Development of vertexing and lifetime triggers and a study of B_s mixing using hadronic decays at DØ

Christopher Barnes

Imperial College London

A thesis submitted for the degree of
Doctor of Philosophy
of the University of London
and the Diploma of Imperial College

March, 2005

Development of vertexing and lifetime triggers and a study of B_s mixing using hadronic decays at DØ

Christopher Barnes
Imperial College London

March, 2005

ABSTRACT

The DØ detector underwent a major upgrade to maximise its ability to fully exploit Run II at the Fermilab Tevatron, the world's highest energy collider. The upgrade included a completely new central tracking system with an outer scintillating fibre tracker and an inner silicon vertex detector all within a 2T super conducting solenoid. This thesis describes the development of high level trigger algorithms including vertexing, impact parameter significance and invariant mass, that utilise tracks from these detectors.

One of the main physics goals of Run II is the observation of B_s oscillations. This measurement, which cannot be performed at the B factories, will significantly constrain the "unitarity triangle" associated with CP violation and so probe the Standard Model of particle physics. Furthermore this is an interesting measurement as the study of mixing in meson systems has a long history for revealing new physics. The second part of this thesis presents a study of the hadronic decay $B_s \to D_s\pi$. This important mode provides the best proper time resolution for B_s mixing and is reconstructed for the first time at DØ. Projections on the sensitivity to B_s oscillations are then presented.

Acknowledgements

I would like to thank...

Gavin Davies and Rick Jesik for being great supervisors and friends, providing help and generally keeping me out of trouble.

Trevor Bacon and John Hassard for proof reading my thesis and providing lots of helpful comments.

Everyone at Fermilab and Imperial who helped me, including Robert Illingworth for getting me started with everything, Jon Hays, Per Jonsson and Terry Wyatt for helping with the Level-3 work and Vivek Jain and Andrei Nomerotski for helping with the B physics.

All my family for sticking by me, especially my mother, who did everything she could to get me here.

All my friends in London, Chorley, Chicago and elsewhere who have been a constant source of amusement and were there when I needed to let off steam.

George for always being there for me and keeping me sane. I owe her a great deal.

Finally, PPARC for paying my fees and supporting me for three years and the Department for Work and Pensions, who supported me for the rest.

Contents

List of Figures

List of Tables

Preface

This thesis describes work performed as a member of the DØ collaboration and on the DØ experiment between December 2001 and December 2004. The focus of work was in the development of Level-3 vertexing tools and filters designed specifically for triggering on low p_T B physics events. In addition, using data collected with these triggers, the $B_s \to D_s^- \pi^+$ decay mode was reconstructed.

I have been an active member of the Level-3 algorithms group for the duration of my time at DØ. I first developed a Level-3 tracking testbed that is still being used by the group. I then took over responsibility for the Level-3 vertexing algorithms. The z vertexing tool was originally written by Ray Beuselinck. In February 2002 I first tested and commissioned the existing basic tool before developing it further. I was solely responsible for the x-y vertex tool from the design stage through to the final implementation and testing. All bug fixes and code development on both tools was undertaken by myself. Additionally I made the certification studies needed for each new release and presented the results to the trigger board to allow the tools to run online. These Level-3 vertexing tools are the only ones of their kind at DØ and form an integral part of the trigger.

I have been a member of the B physics group since around the summer of 2002. I have made many contributions since then including trigger studies and, more notably, the observation of the first hadronic B decays at DØ, in particular $B_s \to D_s^- \pi^+$. My development of triggers designed for B physics is undoubtedly my largest contribution to the B physics effort at DØ. I was the only person working in this

very important area. The invariant mass tool existed in a simple form, developed by Gustaaf Brooijmans. I made significant changes so that two track, two muon and two jet invariant masses could be calculated with specified masses and requiring opposite signs. The track and muon impact parameter filters and the Level-3 tool that they rely on were solely designed and developed by myself. I therefore became responsible for this family of tools and triggers and had to perform bug fixes, maintenance, extensive testing and certification. Again, I convinced the trigger board to allow them to run online. These tools allow the single muon trigger to run unprescaled at all luminosities and are essential to the B physics programme at DØ.

The thesis has the following structure

- Chapter 1 is a brief review of the Standard Model, concentrating particularly in the areas that apply to B physics.
- Chapter 2 is a brief description of the Fermilab accelerator and the DØ detector.
- Chapter 3 describes the development of the z and x-y vertex finding tools. There is a description of the algorithms used, the tool implementation and the extensive testing and performance evaluation.
- Chapter 4 describes the development of the trigger tools designed specifically for low p_T B physics. Outlined is the need for such tools and the philosophy behind them. The implementation of the filters is then described and a detailed account of the extensive testing given.
- Chapter 5 describes the work undertaken to reconstruct the hadronic mode $B_s \rightarrow D_s^- \pi^+$ which includes the reconstruction of $B_d \rightarrow D^{*-} \pi^+$, both for the first time at DØ. Projections on the sensitivity to a ΔM_s discovery are presented.
- Chapter 6 provides a summary and outlook.

Chapter 1

Beauty in the Standard Model

The Standard Model (SM) is our best description of fundamental particles and their interactions. It describes the strong and electroweak interactions using a normalisable, relativistic quantum field theory with $SU(3)_C \times SU(2)_L \times U(1)_Y$ gauge symmetry. It is highly successful and has been found to agree with experiment to a very high degree of accuracy[1]. This Chapter introduces the Standard Model and some of the issues relevant to B physics. Excellent reviews can be found in references [1] and [2].

1.1 Symmetry in the Standard Model

The connection between symmetries and conservation laws is a powerful concept. In classical mechanics, rotational invariance of a closed system gives rise to angular momentum conservation. The requirement that the SM Lagrangian is invariant under certain transformations places tight constraints on the physics it describes. Of these, the principle of gauge invariance and the discrete symmetries charge conjugation, parity and time reversal are fundamental.

[1]The recent discovery of neutrino oscillations [3] is an exception although this is a natural extension to the SM.

1.1.1 Gauge invariance

The principle of gauge invariance is best illustrated starting from the Lagrangian[2] for a free Dirac field, $\Psi = \Psi(x)$:

$$\mathcal{L}_{Dirac} = \overline{\Psi}(i\gamma^{\mu}\partial_{\mu} - m)\Psi. \tag{1.1}$$

The γ^{μ} are the 4×4 gamma-matrices and the adjoint field, $\overline{\Psi}$, is defined as $\Psi^{\dagger}\gamma^{0}$. Equation 1.1 is invariant under $U(1)$ global gauge transformations

$$\begin{aligned} \Psi &\rightarrow \Psi' = e^{i\theta}\Psi \\ \overline{\Psi} &\rightarrow \overline{\Psi}' = e^{-i\theta}\overline{\Psi}, \end{aligned} \tag{1.2}$$

where θ is a real, continuous parameter, independent of space-time coordinates ($\theta \neq \theta(x)$). Hence this is a global gauge transformation. The group $U(1)$ is Abelian which means its members commute. Noether's Theorem relates the invariance of the Lagrangian under these transformations to a conserved current which, in this case, is electric charge.

Now consider local gauge transformations where θ depends on the space-time coordinates, $\theta = \theta(x)$. Under this transformation the Lagrangian is no longer invariant:

$$\mathcal{L}_{Dirac} \rightarrow \mathcal{L}'_{Dirac} = \mathcal{L}_{Dirac} - \overline{\Psi}\gamma^{\mu}\partial_{\mu}\theta(x)\Psi \tag{1.3}$$

since the partial derivative term acting on the exponential is now non-zero. In order to restore invariance, the derivative must be modified so that it transforms covariantly, in the same way as Ψ. This is called the covariant derivative, D_{μ}, and has the transformation property:

$$D_{\mu}\Psi \rightarrow D'_{\mu}\Psi' = e^{i\theta(x)}D_{\mu}\Psi. \tag{1.4}$$

To construct D_{μ} an additional real gauge field $A_{\mu} = A_{\mu}(x)$ is introduced such that:

$$D_{\mu} \equiv \partial_{\mu} + ieA_{\mu}. \tag{1.5}$$

[2]Strictly speaking $\mathcal{L}$ is the Lagrangian Density with the Lagrangian given by $L = \int \mathcal{L} d^3x$.

Under local gauge transformations, A_μ transforms such that the extra term in Equation 1.3 is cancelled:

$$A_\mu \rightarrow A'_\mu = A_\mu - \frac{1}{e}\partial_\mu \theta(x). \tag{1.6}$$

The invariance of the Lagrangian is then restored by replacing ∂_μ with D_μ:

$$\begin{aligned} \mathcal{L}^{GI}_{Dirac} &= \overline{\Psi}(i\gamma^\mu D_\mu - m)\Psi \\ &= \overline{\Psi}(i\gamma^\mu \partial_\mu - m)\Psi - e\overline{\Psi}\gamma^\mu \Psi A_\mu \end{aligned} \tag{1.7}$$

where the GI denotes gauge invariance. By demanding that the Lagrangian is invariant under local gauge transformations, the gauge field, A_μ, has been introduced. In fact this field couples with the Dirac particles (charge e $\rightarrow$ -e) in exactly the same way as the photon field. For completeness, there must be a gauge invariant kinetic energy term for the photon. It must be constructed from the gauge invariant field strength tensor

$$F_{\mu\nu} = \partial_\mu A_\nu - \partial_\nu A_\mu \tag{1.8}$$

and the kinetic energy term is given by

$$\mathcal{L}^{K.E.}_{\gamma} = -\frac{1}{4}F_{\mu\nu}F^{\mu\nu}, \tag{1.9}$$

which reproduces Maxwell's Equations. Hence the Lagrangian for Quantum electrodynamics (QED) is given by

$$\begin{aligned} \mathcal{L}_{QED} &= \mathcal{L}^{GI}_{Dirac} + \mathcal{L}^{K.E.}_{\gamma} \\ &= \overline{\Psi}(i\gamma^\mu D_\mu - m)\Psi - \frac{1}{4}F_{\mu\nu}F^{\mu\nu} \\ &= \overline{\Psi}(i\gamma^\mu \partial_\mu - m)\Psi + e\overline{\Psi}\gamma^\mu \Psi A_\mu - \frac{1}{4}F_{\mu\nu}F^{\mu\nu}. \end{aligned} \tag{1.10}$$

By requiring that the Lagrangian for a free Dirac field is invariant under local gauge transformations, we have arrived at the Lagrangian for QED. Note that there is no term of the form:

$$-\frac{1}{2}m^2_\gamma A_\mu A^\mu, \tag{1.11}$$

which would give the photon a non-zero mass. Clearly such a term would not be gauge invariant and cannot be added to the Lagrangian.

In a completely analogous way, the structure of the strong and the weak forces can be inferred by requiring invariance under SU(3) and SU(2) local gauge transformations. Instead of one gauge field, as for the photon, there are now eight gluon fields for SU(3) and three fields for SU(2). In addition, these groups are no longer Abelian which gives rise to additional terms in the equivalents of Equations 1.6 and 1.8. These additional terms represent the self-interaction of the gauge fields. Note that mass terms for the gauge bosons can still not be added to the Lagrangian in a gauge invariant way. This can only be achieved via electroweak symmetry breaking and the Higgs Mechanism.

1.1.2 Discrete symmetries

As well as local gauge invariance there are additional discrete symmetries that restrict the physics described by the SM. These are charge conjugation (C), parity (P) and time reversal (T).

Charge conjugation and Parity

These two operations have similar properties. They are both unitary and two-fold symmetries. Therefore acting on a particle state twice must give back the original state. Charge conjugation, C, converts a particle into its anti-particle by reversing the sign of all internal quantum numbers such as charge and baryon number. Only particles that are their own antiparticles can be eigenstates of C with eigenvalues of ± 1. Parity, P, changes the sign of the spacial coordinates $(x, y, z) \rightarrow (-x, -y, -z)$ and has eigenvalues of ± 1.

C and P are conserved in the strong and electromagnetic interactions but violated in the weak interaction. In the charged weak sector, C and P are maximally violated and in the limit of vanishing neutrino mass, the weak interaction only couples to

left-handed neutrinos. Therefore

$$\Gamma(\pi^+ \to \mu^+\nu_L) \neq \Gamma(\pi^+ \to \mu^+\nu_R) \quad \text{P violation} \tag{1.12}$$

and

$$\Gamma(\pi^+ \to \mu^+\nu_L) \neq \Gamma(\pi^- \to \mu^-\overline{\nu}_L) \quad \text{C violation} \tag{1.13}$$

where the processes on the right are not observed in nature.

However, the combined operation, CP, was thought to be an exact symmetry. Therefore

$$\Gamma(\pi^+ \to \mu^+\nu_L) = \Gamma(\pi^- \to \mu^-\nu_R) \quad \text{CP conservation} \tag{1.14}$$

but this symmetry is now known to be violated.

CP violation was first discovered in the kaon system in 1964 [4]. Neutral kaons are observed as a mixture of short and long lived eigenstates, K_S with τ =(0.8953 $\pm$ 0.0006)$\times 10^{-10}$s and K_L with τ =(5.18 $\pm$ 0.04)$\times 10^{-8}$s [5]. If weak interactions conserve CP then these states are the CP=+1 and CP=-1 eigenstates respectively. However, the observation of the decay $K_L \to 2\pi$ which is a CP=+1 final state showed the existence of CP violation. This particular type of CP violation is known as CP violation in the mixing. A more detailed discussion of CP violation is presented in Section 1.5.

Time reversal and CPT invariance

Time reversal symmetry, T, performs the translation $t \to -t$. T is an antiunitary operator which can be decomposed into a unitary transformation and complex conjugation. Any local relativistic quantum field theory must be CPT invariant. A consequence is that the mass of a particle and its anti-particle are equal. The best test of this comes from the neutral kaon system and $|(m_{K^0} - m_{\overline{K}^0})/m_{K^0}| \leq 10^{-18}$ at the 95% confidence level [5].

An additional consequence is that any violation in any one symmetry implies violation in the other symmetries for the CPT theorem to hold. For example CP violation implies T violation in the Lagrangian for that process.

1.2 The electroweak interaction

The electroweak sector describes the interactions of the quarks and leptons with the photon, the $W^{\pm}$ and Z gauge bosons [6]. The weak and electromagnetic forces are unified in a theory with $U(1) \times SU(2)$ gauge symmetry.

1.2.1 The electroweak Lagrangian

As has already been demonstrated, the $U(1)$ and $SU(2)$ symmetries give rise to one and three massless gauge bosons respectively. However, in the electroweak theory, these gauge bosons do not directly represent the photon and the $W^{\pm}$ and Z found in nature. Instead the $U(1)$ field charge is that of hypercharge, Y. For this reason the symmetry is denoted by $U(1)_Y$ and the gauge field as B_μ.

The $SU(2)$ weak-isospin generators are given by

$$\mathbf{T}^1 = \frac{1}{2}\begin{pmatrix} 0 & 1 \\ 1 & 0 \end{pmatrix}, \quad \mathbf{T}^2 = \frac{1}{2}\begin{pmatrix} 0 & -i \\ i & 0 \end{pmatrix}, \quad \mathbf{T}^3 = \frac{1}{2}\begin{pmatrix} 1 & 0 \\ 0 & -1 \end{pmatrix}, \tag{1.15}$$

which are simply 1/2 times the Pauli spin matrices. These generators form the following Lie algebra:

$$[\mathbf{T}^a, \mathbf{T}^b] = i\epsilon_{abc}\mathbf{T}^c. \tag{1.16}$$

T^3 is the eigenvalue of the 3rd component of the weak-isospin. The left (right) handed fermions transform as $SU(2)$ weak-isospin doublets (singlets). As will become clear, the weak interaction couples only to left handed fermions and right handed anti-fermions. For this reason the symmetry is denoted by $SU(2)_L$. Table 1.1 displays the values of Y, T and T^3 for any given generation. To obtain the physical gauge fields for the photon and W and Z the following transformations are performed

$$\mathbf{T}^{\pm} = \frac{1}{\sqrt{2}}(\mathbf{T}^1 \mp i\mathbf{T}^2), \quad W_\mu^{\pm} = \frac{1}{\sqrt{2}}(W_\mu^1 \pm iW_\mu^2), \tag{1.17}$$

and

$$\begin{pmatrix} B_\mu \\ W_\mu^3 \end{pmatrix} = \begin{pmatrix} \cos\theta_w & -\sin\theta_w \\ \sin\theta_w & \cos\theta_w \end{pmatrix} \begin{pmatrix} A_\mu \\ Z_\mu \end{pmatrix} \tag{1.18}$$

Particle Type	Fields	T	T^3	Y
Leptons	$l_L = \begin{pmatrix} \nu_L^e \\ e_L^- \end{pmatrix}$	$1/2$ $1/2$	$1/2$ $-1/2$	-1 -1
	e_R	0	0	-2
Quarks	$q_L = \begin{pmatrix} u_L \\ d_L \end{pmatrix}$	$1/2$ $1/2$	$1/2$ $-1/2$	$1/3$ $1/3$
	u_R d_R	0 0	0 0	$4/3$ -2/3

Table 1.1: Charges and fields for a generation of fermions.

where θ_w is the Weinberg angle and A_μ and Z_μ are the photon and Z fields respectively. The theory is constructed using the transformed fields, imposing local gauge invariance and forming the covariant derivative. The interaction terms for the fermion fields take the form

$$\begin{aligned}\mathcal{L}_{int} =& \overline{L}\gamma^\mu g(\mathbf{T}^+ W_\mu^+ + \mathbf{T}^- W_\mu^-)L \\ &+\overline{L}\gamma^\mu(g\mathbf{T}^3\sin\theta_w + g'\frac{\mathbf{Y}}{2}\cos\theta_w)A_\mu L + \overline{R}\gamma^\mu(g'\frac{\mathbf{Y}}{2}\cos\theta_w)A_\mu R \\ &+\overline{L}\gamma^\mu(g\mathbf{T}^3\cos\theta_w - g'\frac{\mathbf{Y}}{2}\sin\theta_w)Z_\mu L - \overline{R}\gamma^\mu(g'\frac{\mathbf{Y}}{2}\sin\theta_w)Z_\mu R\end{aligned} \tag{1.19}$$

where L and R refer to fermion doublets and singlets respectively. Further inspection of Equation 1.19 reveals three separate interactions. The first term couples electrons to neutrinos and up type quarks to down type quarks and is clearly the charged current weak interaction term. It is now clear why this interaction violates parity as it only acts on the left handed particle fields. The second term in Equation 1.19 is simply the QED interaction, provided

$$g\sin\theta_w = g'\cos\theta_w = e, \tag{1.20}$$

and the generator of the electric charge, Q, is given by

$$\mathbf{Q} = \mathbf{T}^3 + \frac{\mathbf{Y}}{2}. \tag{1.21}$$

Using the eigenvalues in Table 1.1 it is clear that neutrinos do not couple to A_μ. In addition, A_μ couples to both the left and right handed quarks and leptons equally;

it conserves parity. The final term in Equation 1.19 is the weak neutral current interaction whose coupling is different for the left and right handed fermions. The weak interactions have a V-A structure which is pure in the case of the charged current and impure in the case of the neutral current.

Despite the success of this theory, the masses of the W and Z bosons still cannot be added in a gauge invariant way. In order to achieve this, a mechanism known as spontaneous symmetry breaking and in particular, the Higgs mechanism, must be applied. As will be demonstrated, by introducing a new scalar field, known as the Higgs field, not only are the masses for the W and Z bosons generated but also those of the fermions. This occurs in a gauge invariant way and leaves the resulting theory renormalisable.

1.2.2 Electroweak symmetry breaking

Spontaneous symmetry breaking and the Higgs mechanism [7] [8] [9] is best demonstrated by considering the $U(1)$ locally gauge invariant Lagrangian previously constructed, Equation 1.10. Consider a self interacting, complex scalar field, ϕ, that transforms under $U(1)$ local gauge transformations:

$$\phi = \frac{1}{\sqrt{2}}(\phi_1 + i\phi_2), \quad \phi \rightarrow \phi' = e^{i\alpha(x)}\phi. \tag{1.22}$$

The gauge invariant Lagrangian for the scalar field is

$$\mathcal{L}_{scalar} = (\partial^\mu + ieA^\mu)\phi^*(\partial_\mu - ieA_\mu)\phi - \frac{1}{4}F^{\mu\nu}F_{\mu\nu} - V(\phi), \tag{1.23}$$

with the potential term, $V(\phi)$, given by

$$V(\phi) = \mu^2\phi^2 + \lambda\phi^4. \tag{1.24}$$

If μ^2 is positive, the minimum of $V(\phi)$ is at zero and the first term in Equation 1.24 simply describes a massive scalar field. The more interesting case is when μ^2 is negative. The potential has a local (unstable) maximum at zero and a set of minima at $\phi_1^2 + \phi_2^2 = v^2$ where v is the vacuum expectation value $\sqrt{-\mu^2/\lambda}$.

A perturbative expansion must be performed around the classical minimum. If it was performed about the local maximum at $\phi_1 = \phi_2 = 0$ it would not converge. Hence we have to choose one minimum to perform the expansion. By translating the field to $\phi_1 = v, \phi_2 = 0$ the symmetry of the ground state is broken. The field, ϕ, is expressed in terms of two new scalar fields, η and ζ, such that

$$\phi(x) = \frac{1}{\sqrt{2}}(v + \eta(x) + i\zeta(x)). \tag{1.25}$$

Upon substitution in the Lagrangian, Equation 1.23, yields terms such as

$$\begin{aligned} \mathcal{L}'_{scalar} &= \frac{1}{2}(\partial_\mu \zeta)^2 + \frac{1}{2}(\partial_\mu \eta)^2 - \frac{1}{4}F^{\mu\nu}F_{\mu\nu} \\ &- v^2\lambda\eta^2 + \frac{1}{2}e^2v^2A_\mu A^\mu \\ &- evA_\mu\partial^\mu\zeta + .. \end{aligned} \tag{1.26}$$

neglecting cross-terms. This Lagrangian now describes the massive scalar field, η, and a massive gauge field, A_μ, provided that

$$m_\eta = \sqrt{2\lambda v^2} = \sqrt{-2\mu^2}, \quad m_{A_\mu} = ev. \tag{1.27}$$

This Lagrangian also contains a massless Goldstone boson, ζ, and the last term in Equation 1.26 is unphysical. Therefore this Lagrangian cannot describe a physical situation and we require an additional step known as the Higgs mechanism. ϕ is expressed in terms of real fields, h and θ:

$$\phi = \frac{1}{\sqrt{2}}(v + h(x))e^{i\theta(x)/v}, \tag{1.28}$$

which, to first order, has the same form as Equation 1.25. By choosing θ so that h is real a particular gauge has been chosen and A_μ becomes

$$A_\mu \rightarrow A_\mu + \frac{1}{ev}\partial_\mu\theta. \tag{1.29}$$

On substitution of Equations 1.28 and 1.29 into the Lagrangian we obtain

$$\begin{aligned}\mathcal{L}''_{scalar} &= \frac{1}{2}(\partial_\mu h)^2 - \frac{1}{4}F^{\mu\nu}F_{\mu\nu} \\ &- v^2\lambda h^2 + \frac{1}{2}e^2v^2A_\mu A^\mu \\ &- \lambda v h^3 - \frac{1}{4}\lambda h^4 \\ &+ \frac{1}{2}e^2A_\mu^2h^2 + ve^2A_\mu^2h. \end{aligned} \tag{1.30}$$

The theory is independent of θ and there is no longer an unphysical Goldstone boson. In Equation 1.30 the third line describes the self interaction of the h field and the fourth line the interaction of the gauge and h fields. This principle of spontaneous symmetry breaking can be applied to the $U(1)_Y \times SU(2)_L$ Lagrangian of electroweak interactions [6].

In electroweak symmetry breaking, the complex scalar field must transform as an $SU(2)$ doublet

$$\mathbf{\Phi} = \begin{pmatrix} \Phi^+ \\ \Phi^\circ \end{pmatrix}, \tag{1.31}$$

and is assigned $T = 1/2$ and $Y = 1$. The physical vacuum is degenerate and we choose it to be in the $T^3 = -1/2$ direction and real:

$$\mathbf{\Phi}_{vac} = \begin{pmatrix} 0 \\ \frac{\nu}{\sqrt{2}} \end{pmatrix}. \tag{1.32}$$

Choosing the unitary gauge and translating the field to the physical vacuum, $\mathbf{\Phi}$ becomes

$$\mathbf{\Phi} = \frac{1}{\sqrt{2}}\begin{pmatrix} 0 \\ \nu + h \end{pmatrix}, \tag{1.33}$$

where $h(x)$ is the Higgs field. Upon substitution of 1.33 into the electroweak Lagrangian for the scalar field, the photon remains massless but the W and Z bosons gain mass terms with

$$M_W = \frac{1}{2}vg, \quad M_Z = \frac{1}{2}v\sqrt{g^2 + g'^2} = \frac{M_W}{\cos\theta_W}. \tag{1.34}$$

There are still no mass terms for the fermions but an attractive feature of this mechanism is that these can be generated, in a gauge invariant way, using the same scalar doublet.

The masses are generated by introducing the $U(1) \times SU(2)$ gauge invariant Yukawa couplings. For the leptons these are of the form

$$\mathcal{L}_{Yukawa} = -G_e \bar{l}_L \Phi e_R + h.c. \tag{1.35}$$

where G_e are the arbitrary Yukawa couplings that must be determined from experiment and $h.c.$ refers to the hermitian conjugate. Upon substitution of Equation 1.33 into the Yukawa terms the symmetry is broken and we obtain

$$\mathcal{L}_{Yukawa} = -m_e(\overline{e}_L e_R + \overline{e}_R e_L) - \frac{m_e}{v}(\overline{e}_L e_R + \overline{e}_R e_L)h, \tag{1.36}$$

with

$$m_e = \frac{G_e v}{\sqrt{2}}. \tag{1.37}$$

The first term is the mass of the lepton and the second term is the interaction of the lepton with the Higgs field.

The quark masses can be generated in a similar way. The most general Yukawa interactions allow inter-generation mixing as there is no symmetry that enforces a simpler structure.[3] Therefore, there are terms of the form

$$-(M_u)_{ij}\overline{u}^i_L u^j_R - (M_d)_{ij}\overline{d}^i_L d^j_R + h.c, \tag{1.38}$$

where i and j run over the three generations. In order to recover the physical mass eigenstates the weak eigenstates must be rotated so that the mass matrices are diagonal. Therefore

$$u^i_R = (V_u)^i_j {u'_R}^j \quad d^i_R = (V_d)^i_j {d'_R}^j, \tag{1.39}$$

where V_u and V_d are both 3×3 unitary matrices.

[3] Any mixing in the lepton sector is unobservable with massless neutrinos.

1.3 The CKM matrix

In the electroweak interaction the fermion masses are generated via their Yukawa coupling to the Higgs field. However, as described in the previous section, the physical mass eigenstates are not equal to the weak eigenstates.

Consider the substitution of the quark mass eigenstates, Equation 1.39, into the interaction terms of the electroweak Lagrangian, Equation 1.19. In the neutral current, terms of the form $V_u{}^\dagger V_u$ and $V_d{}^\dagger V_d$ appear which are simply the identity by unitarity. There are no flavour changing neutral currents at the tree level. However in the weak current, terms such as $V_u{}^\dagger V_d$ allow the possibility of quark mixing. This complex 3×3 unitary matrix is called the Cabibbo-Kobayashi-Maskawa (CKM) matrix and is represented by

$$V_{CKM} = \begin{pmatrix} V_{ud} & V_{us} & V_{ub} \\ V_{cd} & V_{cs} & V_{cb} \\ V_{td} & V_{ts} & V_{tb} \end{pmatrix}, \tag{1.40}$$

where V_{ij} represents the amplitude of the flavour changing process $u_i \to d_j$ where i, j are indices over the up and down type quarks respectively. As already stated, V_{CKM} is unitary. This constraint plus the fact that relative phases are unobservable leaves only 4 of the total 18 parameters independent. Of these parameters, three are real and one is a complex phase that parameterises CP violation in the SM.

The standard parameterisation [5] uses a choice of phases that leaves V_{ud} and V_{cb} real. The three real parameters are represented by the angles θ_{12}, θ_{13} and θ_{23} and the CP violating phase by δ_{13}. The CKM matrix then becomes

$$V_{CKM} = \begin{pmatrix} c_{12}c_{13} & s_{12}c_{13} & s_{13}e^{-i\delta_{13}} \\ -s_{12}c_{23} - c_{12}s_{23}s_{13}e^{i\delta_{13}} & c_{12}c_{23} - s_{12}s_{23}s_{13}e^{i\delta_{13}} & s_{23}c_{13} \\ s_{12}s_{23} - c_{12}c_{23}s_{13}e^{i\delta_{13}} & -c_{12}s_{23} - s_{12}c_{23}s_{13}e^{i\delta_{13}} & c_{23}c_{13} \end{pmatrix}, \tag{1.41}$$

where $c_{ij} = \cos\theta_{ij}$ and $s_{ij} = \sin\theta_{ij}$. All θ_{ij} lie in the range $(0, \pi/2)$ and δ_{13} in

the range $(0, 2\pi)$. The angles represent the mixing between any two generations. Therefore if θ_{13} and θ_{23} are zero, the third generation decouples and the original Cabibbo matrix is recovered with θ_{12} being the Cabibbo angle. CP violation arises for any non-zero value of δ_{13} and there must be at least three generations for an observable complex phase to exist. In fact Kobayashi and Maskawa proposed the existence of the third generation to provide a mechanism to explain CP violation [10].

A common parameterisation is that due to Wolfenstein [11] with the parameters λ, A, ρ and η defined by

$$\lambda \equiv s_{12}, \quad A \equiv s_{23}/\lambda^2, \quad \rho + i\eta \equiv s_{13}e^{i\delta_{13}}/A\lambda^3. \tag{1.42}$$

Experimentally $\lambda \approx 0.22$, $A \approx 0.8$ and $\sqrt{\rho^2+\eta^2} \approx 0.4$ [2]. Expanding in powers of λ, V_{CKM} becomes

$$\begin{aligned} V_{CKM} &= \begin{pmatrix} 1-\frac{\lambda^2}{2} & \lambda & A\lambda^3(\rho - i\eta) \\ -\lambda & 1-\frac{\lambda^2}{2} & A\lambda^2 \\ A\lambda^3(1-\rho-i\eta) & -A\lambda^2 & 1 \end{pmatrix} \\ &+ \begin{pmatrix} -\frac{1}{8}\lambda^4 & 0 & 0 \\ A^2(\frac{1}{2}-\rho-i\eta)\lambda^5 & -\frac{1}{8}(1+4A^2)\lambda^4 & 0 \\ \frac{1}{2}A(\rho+i\eta)\lambda^5 & A(\frac{1}{2}-\rho-i\eta)\lambda^4 & -\frac{1}{2}A^2\lambda^4 \end{pmatrix} + O(\lambda^6) \end{aligned} \tag{1.43}$$

with the variable η representing the CP-violating phase. In this parameterisation the hierarchical structure is evident with the dominance of the diagonal elements and the suppression of transitions between quarks of different generations.

The unitary constraints on the CKM matrix require rows and columns to be orthonormal. Therefore there are 12 expressions inter-relating the CKM elements. The six expressions representing orthogonality can be represented as triangles in the complex plane. The most commonly used relation is

$$V_{ud}V_{ub}^* + V_{cd}V_{cb}^* + V_{td}V_{tb}^* = 0, \tag{1.44}$$

since its sides are all similar in length and its internal angles are large. Figure 1.1a shows the so called "unitarity triangle". It is instructive to rescale in terms

of the Wolfenstein parameters and divide Equation 1.44 by $A\lambda^3 \approx V_{cd}V_{cb}{}^*$. In the rescaled triangle the vertices are $(0,0)$, $(1,0)$ and $(\overline{\rho},\overline{\eta})$ where $\overline{\rho} = (1-\lambda^2/2)\rho$ and $\overline{\eta} = (1-\lambda^2/2)\eta$. Figure 1.1b shows the rescaled unitarity triangle.

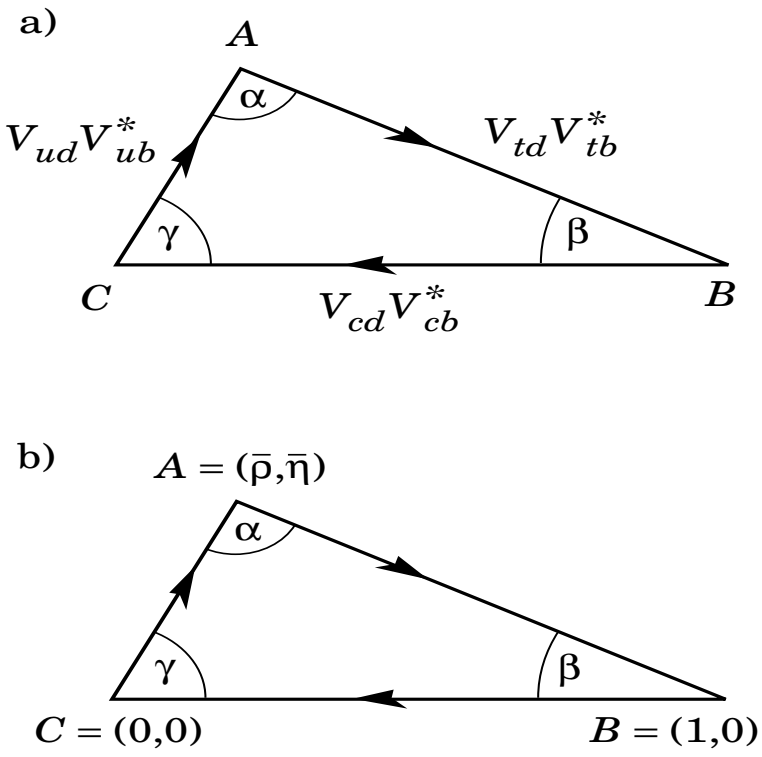

Figure 1.1: The unitarity triangle [5]. (a) Graphical representation of Equation 1.44. (b) Rescaled triangle with vertices at $(0,0)$, $(1,0)$ and $((1-\lambda^2/2)\rho, (1-\lambda^2/2)\eta)$.

The angles α, β and γ are defined by

$$\alpha \equiv arg\left[-\frac{V_{td}V_{tb}^*}{V_{ud}V_{ub}^*}\right], \quad \beta \equiv arg\left[-\frac{V_{cd}V_{cb}^*}{V_{td}V_{tb}^*}\right], \quad \gamma \equiv arg\left[-\frac{V_{ud}V_{ub}^*}{V_{cd}V_{cb}^*}\right]. \tag{1.45}$$

It is important to note that these unitarity triangles represent the amount of CP violation in the SM. If there was no CP violation, they would have zero area. In addition, if the SM is consistent the sum of the angles of each unitarity triangle should sum to 180° and all unitarity triangles should have the same area.

1.4 B meson mixing

In this section the formalism for neutral B mixing is described. The following applies to both B_d and B_s mesons with the meson denoted by B_i where $i = d, s$. In the SM, $B^0 - \overline{B}^0$ mixing occurs via second order flavour changing weak diagrams such as Figure 1.2. This mixing causes oscillations between the two flavour eigenstates B^0 and $\overline{B}^0$ since an initially produced B^0 will evolve into a superposition of B^0 and $\overline{B}^0$. Consider a B_i^0 tagged at time $t = 0$. Its state vector is given by $|B_i^0(t)\rangle$ with

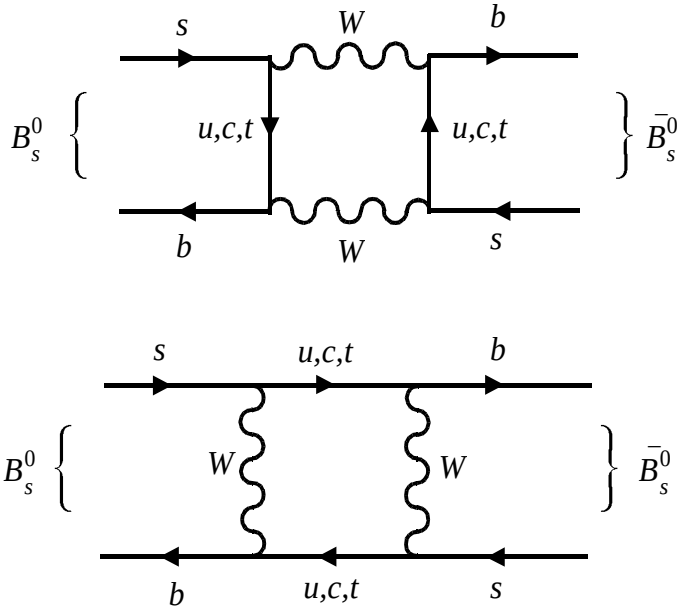

Figure 1.2: Standard model weak diagrams for B_s mixing. The exchange of a top quark dominates.

$|B_i^0(t=0)\rangle \equiv |B_i^0\rangle$. Similarly $|\overline{B}_i^0(t)\rangle$ is the state vector for an initially tagged $\overline{B}_i^0$ meson. The time evolution is given by the approximate[4] Schrödinger equation:

$$i\frac{d}{dt}\begin{pmatrix}|B_i^0(t)\rangle \\ |\overline{B}_i^0(t)\rangle\end{pmatrix} = \left(M - i\tfrac{\Gamma}{2}\right)\begin{pmatrix}|B_i^0(t)\rangle \\ |\overline{B}_i^0(t)\rangle\end{pmatrix}. \tag{1.46}$$

M and Γ are the mass and decay matrices respectively. They are both time independent, Hermitian 2×2 matrices with $M_{11} = M_{22}$ and $\Gamma_{11} = \Gamma_{22}$ given by CPT

[4]There are corrections to the exponential decay at short and long times but these are irrelevant for mixing and CP studies at the Tevatron[2]

invariance. Mixing occurs when these matrices have off diagonal elements and the mass eigenstates are not equal to the flavour eigenstates. The mass eigenstates are defined as the eigenvectors of $M - i\Gamma/2$ which can be expressed as

$$\begin{aligned} |B_{iH}\rangle &= p|B_i^0\rangle + q|\overline{B}_i^0\rangle \\ |B_{iL}\rangle &= p|B_i^0\rangle - q|\overline{B}_i^0\rangle, \end{aligned} \tag{1.47}$$

where the H and L subscripts refer to the heavy and light eigenstates respectively. The time evolution is then given by

$$\begin{aligned} |B_{iH}(t)\rangle &= e^{-(iM_H+\Gamma_H/2)t}|B_{iH}\rangle \\ |B_{iL}(t)\rangle &= e^{-(iM_L+\Gamma_L/2)t}|B_{iL}\rangle, \end{aligned} \tag{1.48}$$

where $M_{H/L} - \frac{i}{2}\Gamma_{H/L}$ are obtained from solving the eigenvalue problem.

The off-diagonal elements of the mass and decay matrices, M_{12} and Γ_{12}, can be calculated from mixing diagrams such as Figure 1.2. To a good approximation, for both the B_d and B_s systems the following simplification applies [2]

$$|\Gamma_{12}| \ll |M_{12}|, \quad \Delta\Gamma \ll \Delta M, \tag{1.49}$$

where $\Delta M = M_H - M_L$ and $\Delta\Gamma = \Gamma_L - \Gamma_H$. This allows an expansion in Γ_{12}/M_{12} and $\Delta\Gamma/\Delta M$. Additional simplifications arise if the final state is flavour specific (such as $B_s \to D_s^- \pi^+$) then B_i^0 can decay into a final state, f, but $\overline{B}_i^0$ cannot. The time dependent decay rates can then be expressed as [2]

$$\begin{aligned} \Gamma(B_i^0(t) \to f) =& N_f |A_f|^2 e^{-\Gamma_i t} \frac{1}{2}\left[\cosh\frac{\Delta\Gamma_i t}{2} + \cos(\Delta M_i t)\right] \\ \Gamma(B_i^0(t) \to \overline{f}) =& N_f |\overline{A}_{\overline{f}}|^2 e^{-\Gamma_i t}(1-a)\frac{1}{2}\left[\cosh\frac{\Delta\Gamma_i t}{2} - \cos(\Delta M_i t)\right], \end{aligned} \tag{1.50}$$

where $\Gamma = 1/2(\Gamma_L + \Gamma_H)$, N_f is a time-independent normalisation, the decay amplitudes are defined as

$$A_f = \langle f|B_i^0\rangle \quad \overline{A}_f = \langle f|\overline{B}_i^0\rangle \tag{1.51}$$

and a is the small parameter given by

$$a = \left|\frac{\Gamma_{12}}{M_{12}}\right| \sin\phi, \quad \phi = \arg\left(-\frac{M_{12}}{\Gamma_{12}}\right). \tag{1.52}$$

This parameter, a, that arises from a relative phase between M_{12} and Γ_{12} describes CP violation in the mixing. This will be described in Section 1.5.

Equation 1.50 demonstrates the fundamentals of mixing. The frequency of the sinusoidal term is given by ΔM and the oscillations are damped due to the exponential term. Experimentally, it is convenient to define the asymmetry, given by

$$\begin{aligned} A_0(t) &= \frac{\Gamma(B_i^0(t) \to f) - \Gamma(B_i^0(t) \to \overline{f})}{\Gamma(B_i^0(t) \to f) + \Gamma(B_i^0(t) \to \overline{f})} \\ &= \frac{N^{non-osc}(t) - N^{osc}(t)}{N^{non-osc}(t) + N^{osc}(t)} \end{aligned} \tag{1.53}$$

where t is the proper time and N^{osc} and $N^{non-osc}$ refer to the number of events tagged as oscillated and non-oscillated respectively. For a flavour specific final state and assuming there is no CP violation in the decay amplitude (Section 1.5) then $|A_f| = |\overline{A}_{\overline{f}}|$. Again, the mode $B_s \to D_s^- \pi^+$ satisfies these conditions. The asymmetry is then given by

$$A_0(t) = \frac{\cos(\Delta M_i t)}{\cosh(\Delta\Gamma t/2)} + \frac{a}{2}\left[1 - \frac{\cos^2(\Delta M_i t)}{\cosh^2(\Delta\Gamma t/2)}\right]. \tag{1.54}$$

Current values

The current values for mixing in the B system are [5]

$$\Delta M_d = 0.502 \pm 0.007 ps^{-1}$$

$$\Delta M_s > 14.4 ps^{-1} \quad 95\% \text{ CL.}$$

In addition $\Delta\Gamma_d \approx 0$ and $\Delta\Gamma_s/\Gamma_s < 0.54$ at 95% CL [5]. Therefore since $\Delta M_s > \Delta M_d$, B_s oscillations are much more rapid than B_d oscillations and a non-zero $\Delta\Gamma_s$ would also cause significant damping. This makes B_s mixing very challenging experimentally.

There are two main strategies to observe B_s mixing. The semileptonic modes, such as $B_s^0 \to D_s^- \mu^+ X$, provide high statistics. However the neutrino in the decay is

not reconstructed which makes the estimate of the B_s momentum consistently lower than the actual momentum. This must be corrected for by a k factor determined from Monte Carlo and causes the proper time resolution to be degraded. These semileptonic decay modes are sensitive to values of ΔM_s of around 18-20 ps^{-1} at most, after which the limited proper time resolution is dominant and no increase in statistics will improve the sensitivity. Higher values of ΔM_s can be probed using hadronic decays such as $B_s^0 \to D_s^- \pi^+$. Because the B_s is fully reconstructed, there is no correction factor needed and the proper time resolution is improved. However these decays are statistics limited due to small branching ratios.

The B mixing parameters can be used to constrain the unitarity triangle. In particular, the ratio of $\Delta M_s/\Delta M_d$ provides a theoretically clean measurement of $|V_{td}|$, the AB side of the unitarity triangle (Figure 1.1). In the ratio many theoretical uncertainties cancel including the assumption that the top-quark loop dominates rather than new physics. Hence

$$\frac{\Delta M_s}{\Delta M_d} = \frac{M_s}{M_d}\xi\frac{|V_{tb}{}^*V_{ts}|}{|V_{tb}{}^*V_{td}|}, \quad \text{where } \xi = \frac{\hat{B}_{B_s} f_{B_s}^2}{\hat{B}_{B_d} f_{B_d}^2}. \tag{1.55}$$

The ratio of hadronic matrix elements, ξ, can be calculated from lattice QCD and is given by $\xi = 1.56 \pm 0.26$ [12]. Using the measured masses, the limit on ΔM_s and assuming for 3 generations $|V_{cb}| \approx |V_{ts}|$, the constraint becomes

$$|V_{td}| < 0.011. \tag{1.56}$$

1.5 CP violation

There are three main types of CP violation: direct and indirect CP violation and CP violation in the interference between decays with and without mixing.

1.5.1 Indirect CP violation

This is also referred to as CP violation in mixing. From Equation 1.47, it follows that

$$\langle B_H | B_L \rangle = |p|^2 - |q|^2. \tag{1.57}$$

Therefore the two states are orthogonal and CP is conserved if and only if $|q/p| = 1$. This is equivalent to a relative phase between M_{12} and Γ_{12} as already stated. The deviation of $|q/p|$ from unity indicates that the mass and CP eigenstates are not equal. As mentioned previously, this was the first type of CP violation to be discovered, in the decay $K_L \to \pi\pi$. Experimentally the following ratios of decay amplitudes are measured

$$\begin{aligned} \eta_{+-} = & \frac{A(K_L \to \pi^+\pi^-)}{A(K_S \to \pi^+\pi^-)} = |\eta_{+-}|e^{i\phi_{+-}} \\ \eta_{00} = & \frac{A(K_L \to \pi^0\pi^0)}{A(K_S \to \pi^0\pi^0)} = |\eta_{00}|e^{i\phi_{00}}, \end{aligned} \tag{1.58}$$

and the current experimental values for these given by [5]

$$\begin{aligned} |\eta_{+-}| = (2.286 \pm 0.014) \times 10^{-3} \quad \phi_{+-} = (43.4 \pm 0.7)^\circ \\ |\eta_{00}| = (2.276 \pm 0.014) \times 10^{-3} \quad \phi_{00} = (43.7 \pm 0.8)^\circ. \end{aligned} \tag{1.59}$$

1.5.2 Direct CP violation

This is also referred to as CP violation in the decay and corresponds to $|\overline{A}_{\overline{f}}| \neq |A_f|$. It is caused by the interference of amplitudes that contain both a weak phase due to the CKM matrix and a phase due to the strong interaction. The strong phase is invariant under a CP transformation whereas the weak phase changes sign.

This type of CP violation was first found in 1999 in $K_{S,L} \to \pi\pi$ decays at the KTEV [13] and NA48 [14] experiments. The CP violating observables, ϵ and ϵ', are defined as

$$\eta_{+-} = \epsilon + \epsilon' \quad \eta_{00} = \epsilon - 2\epsilon', \tag{1.60}$$

with

$$Re(\epsilon'/\epsilon) \approx \frac{1}{6}(1 - |\eta_{00}/\eta_{+-}|). \tag{1.61}$$

A non zero value in $Re(\epsilon'/\epsilon)$ indicates direct CP violation. The current experimentally measured values for ϵ and $Re(\epsilon'/\epsilon)$ are [5]

$$\begin{aligned} |\epsilon| = (2.284 \pm 0.014) \times 10^{-3}, \quad \phi_\epsilon = (43.5 + 0.7)^\circ, \\ Re(\epsilon'/\epsilon) \approx \epsilon'/\epsilon = (1.67 \pm 0.26) \times 10^{-3}. \end{aligned} \tag{1.62}$$

More recently in 2004, direct CP violation in the decay $B^0 \to \pi^+\pi^-$ has been reported by the Belle experiment [15]. Both the Belle [16] and the BaBar experiments [17] have reported direct CP violation in the decay $B^0 \to K^+\pi^-$.

1.5.3 CP violation in the interference between decays with and without mixing

This type of CP violation arises in neutral meson decays where both meson, (M), and anti-meson, $\overline{M}$, can decay to the same final state, f. There is interference between the amplitude for the meson decay, $(M \to f)$ and the amplitude for the meson to mix to the anti-meson and then decay, $(M \to \overline{M} \to f)$.

This type of CP violation was discovered in the B system at the Belle [18] and BaBar [19] experiments in 2001. In these experiments the time dependent decay rates of B^0_d and $\overline{B}^0_d$ mesons to a common CP eigenstate, f_{CP} are measured. The time dependent CP violating asymmetry is defined as

$$A_{CP}(t) = \frac{\Gamma(\overline{B}^0_d \to f_{CP}) - \Gamma(B^0_d \to f_{CP})}{\Gamma(\overline{B}^0_d \to f_{CP}) + \Gamma(B^0_d \to f_{CP})} \tag{1.63}$$

$$= -\eta_f \sin 2\beta \sin \Delta m_d t, \tag{1.64}$$

where η_f is the CP eigenvalue of f_{CP}, Δm_d is the mass difference between the two B_d mass eigenstates and β is the CKM unitarity angle. The world average for $\sin 2\beta$ is given by [5]

$$\sin 2\beta = 0.736 \pm 0.049. \tag{1.65}$$

1.6 Current results

The current values for the magnitudes of the CKM elements at the 90% confidence limit are [5]

$$V_{CKM} = \begin{pmatrix} 0.9739 \text{ to } 0.9751 & 0.221 \text{ to } 0.227 & 0.0029 \text{ to } 0.0045 \\ 0.221 \text{ to } 0.227 & 0.9730 \text{ to } 0.9744 & 0.039 \text{ to } 0.044 \\ 0.0048 \text{ to } 0.014 & 0.037 \text{ to } 0.043 & 0.9990 \text{ to } 0.9992 \end{pmatrix}, \tag{1.66}$$

assuming unitarity and three generations. Using these direct measurements and the indirect constraints due to the parameters ΔM_d, ΔM_s, ϵ and $\sin 2\beta$ tight constraints can be placed on the unitarity triangle. Figure 1.3 shows the current constraints on the apex of the unitarity triangle.

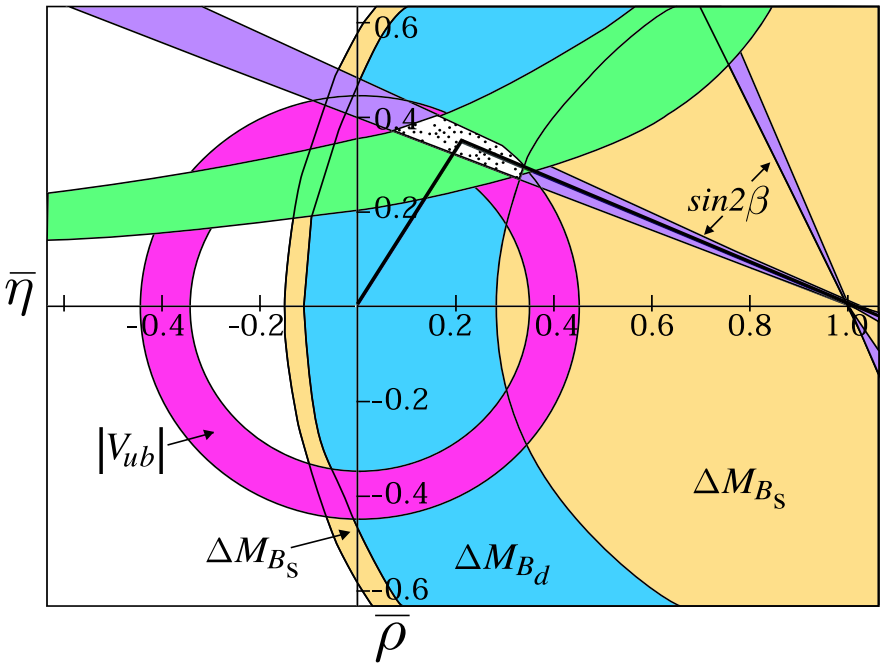

Figure 1.3: Constraints on the position of the apex of the unitarity triangle. These arise from $|V_{ub}|$, ΔM_d, ΔM_s, ϵ and $\sin 2\beta$. The dotted area represents the region of possible apexes and one possible unitarity triangle is shown.

From a combined fit using the direct measurements and indirect constraints [5]

$$\begin{aligned} \overline{\rho} &= 0.20 \pm 0.09 \\ \overline{\eta} &= 0.33 \pm 0.05. \end{aligned} \tag{1.67}$$

From these fits the SM range for ΔM_s is 15.6 - 22.2 ps^{-1}. If the experimental limits on ΔM_s are not included in the fit, the range is 14.2 - 28.1 ps^{-1}[20] . So far, all CP violating processes can be described by one phase in the CKM matrix, $\delta_{13} = 60^\circ \pm 14^\circ$ [5].

1.7 B production at the Tevatron

Figure 1.4 shows the leading order QCD diagrams for b quark production at the Tevatron which are quark-antiquark annihilation and gluon-gluon fusion. At lead-

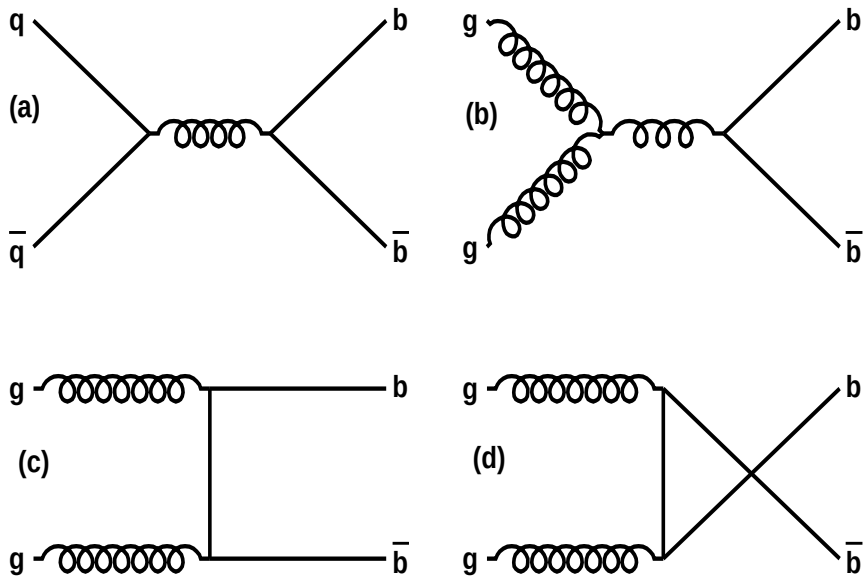

Figure 1.4: Leading order diagrams for b quark production at the Tevatron. The first diagram is quark-antiquark annihilation and the other three are gluon-gluon fusion.

ing order gluon-gluon fusion dominates. These processes are collectively known as flavour creation. In flavour creation the $b\bar{b}$ pair are produced back-to-back in the parton rest frame and the plane transverse to the beam.

Next to leading order (NLO) processes were originally thought to be a small correction but are now thought to contribute significantly [21]. Of these additional processes, flavour excitation and fragmentation are thought to be large. In flavour excitation, a b or $\bar{b}$ is scattered out of the proton initial state by a gluon or light quark. In fragmentation $b\bar{b}$ pairs are not produced in the hard scatter but in the hadronisation of lighter quarks. This includes gluon splitting where a gluon forms a $b\bar{b}$ pair. In both these processes the $b\bar{b}$ pair is no longer necessarily produced back

to back in the parton rest frame and correlations between the b and $\bar{b}$, such as the angular separation, are very different for all three production mechanisms.

Since Run I there has been around a factor of 2-4 discrepancy between the theoretical NLO predictions and the measured spectra by CDF and DØ. New results from CDF and DØ, described in [22], together with improved theoretical calculations accounting for the effects described above have reduced the discrepancy down. There is reasonable agreement at low $p_T < 20$ GeV/c even though effects, including new physics, at the level of 30-40% cannot be completely ruled out due to the large theoretical errors [23] [24]. New analyses from Run II, particularly at higher p_T, should shed light on this important area.

Chapter 2

The Tevatron and the DØ detector

The Tevatron accelerator first started colliding 900 GeV proton and antiproton beams in 1985. Run I was undertaken between 1992 and 1996 and produced many new results including the discovery of the top quark [25]. In Run I, the Tevatron operated at a centre of mass energy of 1.8 TeV. The protons and antiprotons were each grouped into six bunches and the bunch spacing was 3500 ns. The instantaneous luminosity was $\sim$1-2$\times10^{31}$cm^{-2}s^{-1}, with DØ collecting around 120 pb^{-1} of data. Despite the success of Run I, the limited integrated luminosity coupled with the low production cross sections for interesting processes limited the physics capability. Major upgrades were performed on the accelerator complex for Run II including the new Main Injector and antiproton Recycler ring [26]. The number of bunches was increased to 36, the bunch spacing was reduced to 396 ns and the centre of mass energy was increased to 1.96 TeV. This enables a more ambitious physics programme including precise measurements of the top quark and W properties, B-physics including B_s mixing and measurements of CP violation, Higgs searches and searches for physics beyond the Standard Model. Run II began in March of 2001. The Tevatron and the Run II upgrades are described in more detail in Section 2.1.

The DØ detector also underwent significant upgrades for Run II [27]. These included a new tracking system, comprised of an inner silicon vertex detector and scintillating fibre tracker within a 2T superconducting solenoid, the addition of

preshower detectors and an upgraded muon system. Due to the large reduction in the bunch spacing, the readout electronics and trigger were also extensively upgraded. The DØ Run II upgrade is described in Section 2.2.

Run II will consist of two stages: Run IIa and Run IIb. Run IIb will commence after the shutdown in the summer of 2005 when the DØ detector will have undergone another upgrade [28]. This will include the SMT Layer-0, an upgrade of the CFT AFE boards and an upgrade of the trigger to cope with the increased instantaneous luminosity.

2.1 The Fermilab accelerator complex

A diagram illustrating the Fermilab accelerator complex is shown in Figure 2.1.

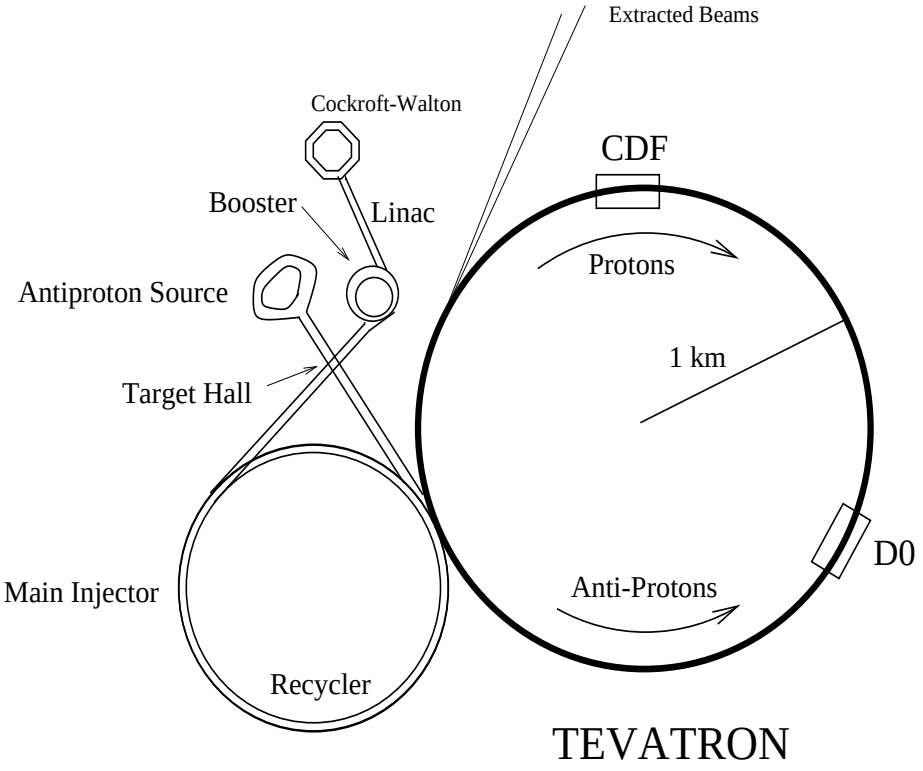

Figure 2.1: The Tevatron accelerator complex.

2.1.1 Proton and antiproton production

The first stage is proton production. Negative hydrogen ions are accelerated to 750 keV by a Cockcroft-Walton accelerator and then to 400 MeV in the Linac. They are focused onto a thin graphite sheet where their electrons are stripped. The protons are then fed into a small synchrotron accelerator called the Booster where they are accelerated to 8 GeV and fed into the Main Injector. The Main Injector is a 3km synchrotron which accelerates the protons to 120 GeV for antiproton production and fixed target experiments or to 150 GeV for injection into the Tevatron.

The antiprotons are produced by firing the 120 GeV proton beam onto a stainless steel target every 1.5 s. The resultant collection of particles is focused using a lithium lens and then passed through a bending magnet that acts as a charge-mass spectrometer. The 8 GeV antiprotons are then passed into the Debuncher and Accumulator Rings that comprise the Antiproton source where they are cooled. Periodically, antiprotons are fed into the Recycler Ring which is a fixed energy storage ring, located in the same tunnel as the Main Injector.

2.1.2 The Tevatron

The Tevatron is the world's highest energy particle accelerator. It is a 6 km circumference synchrotron, accelerating protons and antiprotons to an energy of 980 GeV with the two beams travelling within the same beam pipe. The operating parameters are given in Table 2.1.

As the instantaneous luminosity increases, the number of interactions per bunch crossing will increase. At instantaneous luminosities of $200\times10^{30}\mathrm{cm}^{-2}\mathrm{s}^{-1}$ the number of interactions per bunch crossing will increase to around 7 and the detector performance will drop significantly. This is due to the increased occupancy in the tracking detectors and pile up in the calorimeter. Eventually, the number of interactions per bunch crossing will have to be reduced. Fermilab has decided to implement luminosity levelling which involves dynamically changing the focusing at

	Run I	Run II
Energy $p\bar{p}$ (GeV)	900	980
Proton bunches	6	36
Protons/bunch	2.3×10^{11}	2.7×10^{11}
Antiproton bunches	6	36
Antiprotons/bunch	5.5×10^{10}	3.0×10^{10}
Bunch spacing (ns)	3500	396
Peak luminosity ($cm^{-2}s^{-1}$)	0.16×10^{32}	0.86×10^{32}
Luminosity (pb^{-1}/week)	3.2	17.3
Interactions per crossing	2.5	2.3

Table 2.1: Tevatron operating parameters.

the interaction region. This limits the maximum luminosity but maintains it for much longer, reducing the interactions per bunch crossing while losing only 15% of the total integrated luminosity.

2.1.3 Current status

Figure 2.2 shows the Tevatron peak luminosity. The peak luminosities, although low at the start of Run II, have now exceeded the Run II design specifications. Figure 2.3 shows the integrated luminosity. The design specification for Run II, namely 17.3 pb^{-1}/week, has also been reached.

Up until 2007 the Fermilab complex will be upgraded to increase the luminosity delivered per year [29], [30]. This will include increasing the antiproton production intensity, improving the cooling in the Debuncher and Accumulator, completing the commissioning of the Recycler Ring and upgrades to the Tevatron for operation at higher bunch intensities. Run II will continue until summer 2009 with a predicted integrated luminosity between 4.4 fb^{-1} (baseline) and 8.5 fb^{-1} (design).

2.2 The DØ detector

The DØ detector has a typical cylindrical structure common to many modern high energy physics experiments. Because the beams in the Tevatron are equal in energy, the detector is symmetrical about the interaction region. It consists of three

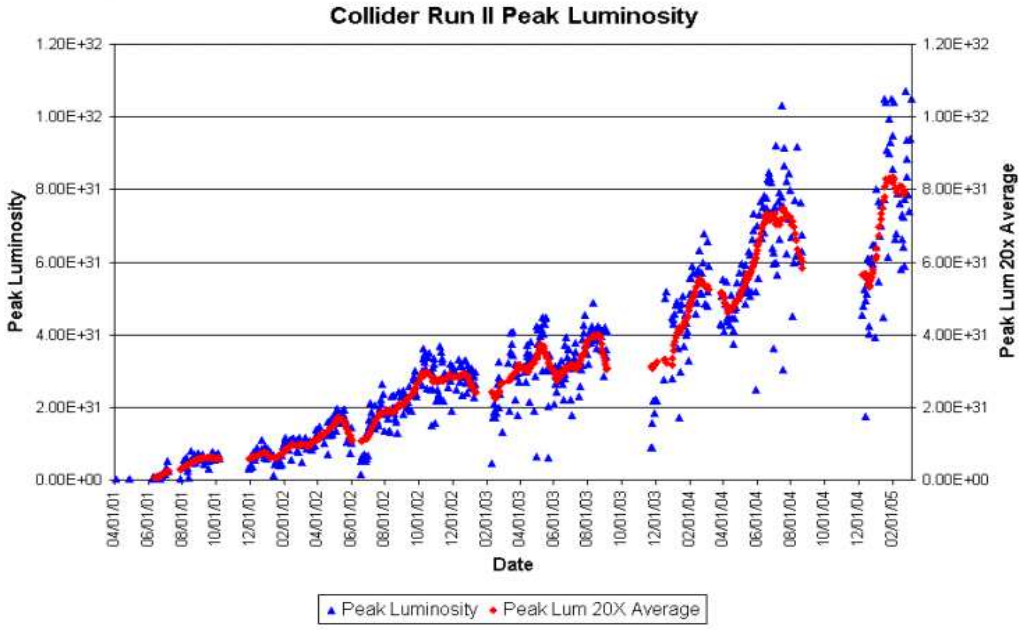

Figure 2.2: Tevatron peak luminosity.

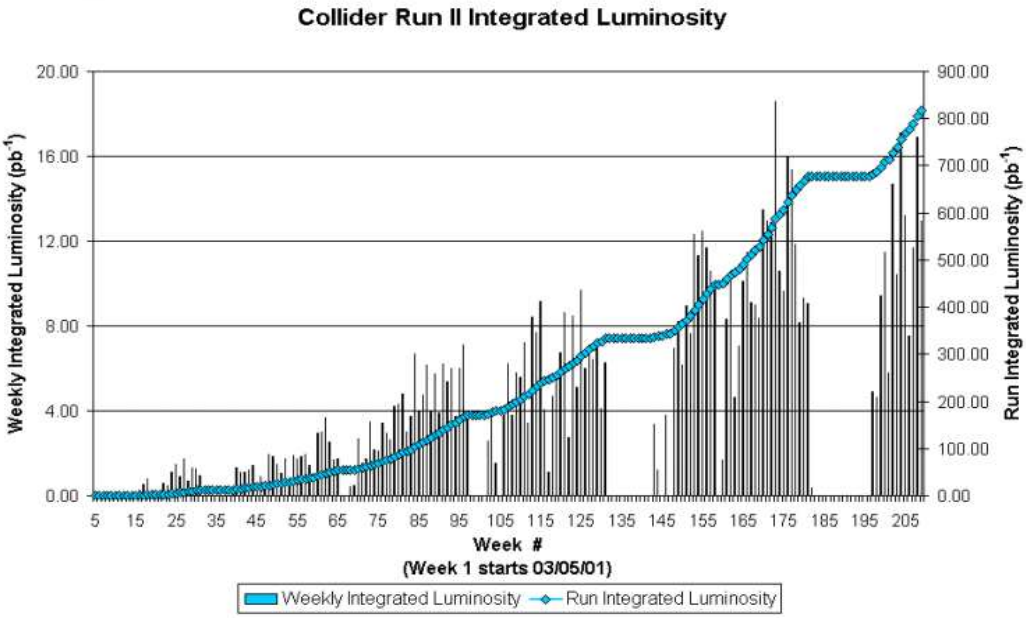

Figure 2.3: Tevatron integrated luminosity.

main subsystems: central tracking detectors for identification of tracks and vertices, a calorimeter to measure the energy of electrons, photons and jets, and a muon spectrometer which identifies and tracks muons. Figure 2.4 shows a side view of the detector. At the very centre is the tracking subsystem and surrounding this is the calorimeter. The outer part of the detector is dominated by the muon system.

A right-handed polar coordinate system is used in all the following with the origin at the centre of the detector at the interaction point. The z-axis points along the direction of the proton beam with the y-axis pointing vertically up. The r coordinate is perpendicular to the beam line and the angles θ and ϕ are the polar ($\theta = 0$ along proton beam direction) and azimuthal angles respectively. The convention at DØ is to replace θ with the pseudo-rapidity, η, defined as

$$\eta = -ln[tan(\theta/2)], \tag{2.1}$$

which is an approximation to the rapidity, a Lorentz invariant quantity. This approximation holds if $mc^2/E \approx 0$ for a given particle.

2.2.1 Central tracking

The tracking system consists of the Silicon Microstrip Tracker (SMT) surrounded by the Central Fibre Tracker (CFT). These are enclosed within a 2 Tesla superconducting solenoid. On the outer face of the solenoid is the central preshower scintillator and the forward preshowers are placed on the inner face of the forward calorimeters. Figure 2.5 displays the DØ tracking subsystem.

Silicon Microstrip Tracker

The Silicon Microstrip Tracker (SMT) design is dictated by the accelerator environment. The length scale must accommodate the large interaction region ($\sigma_z \approx$ 25 cm) and the silicon must be radiation tolerant. The SMT is split into 3 subdetector types: the central barrels, the F-Disks and the H-Disks. The central barrels

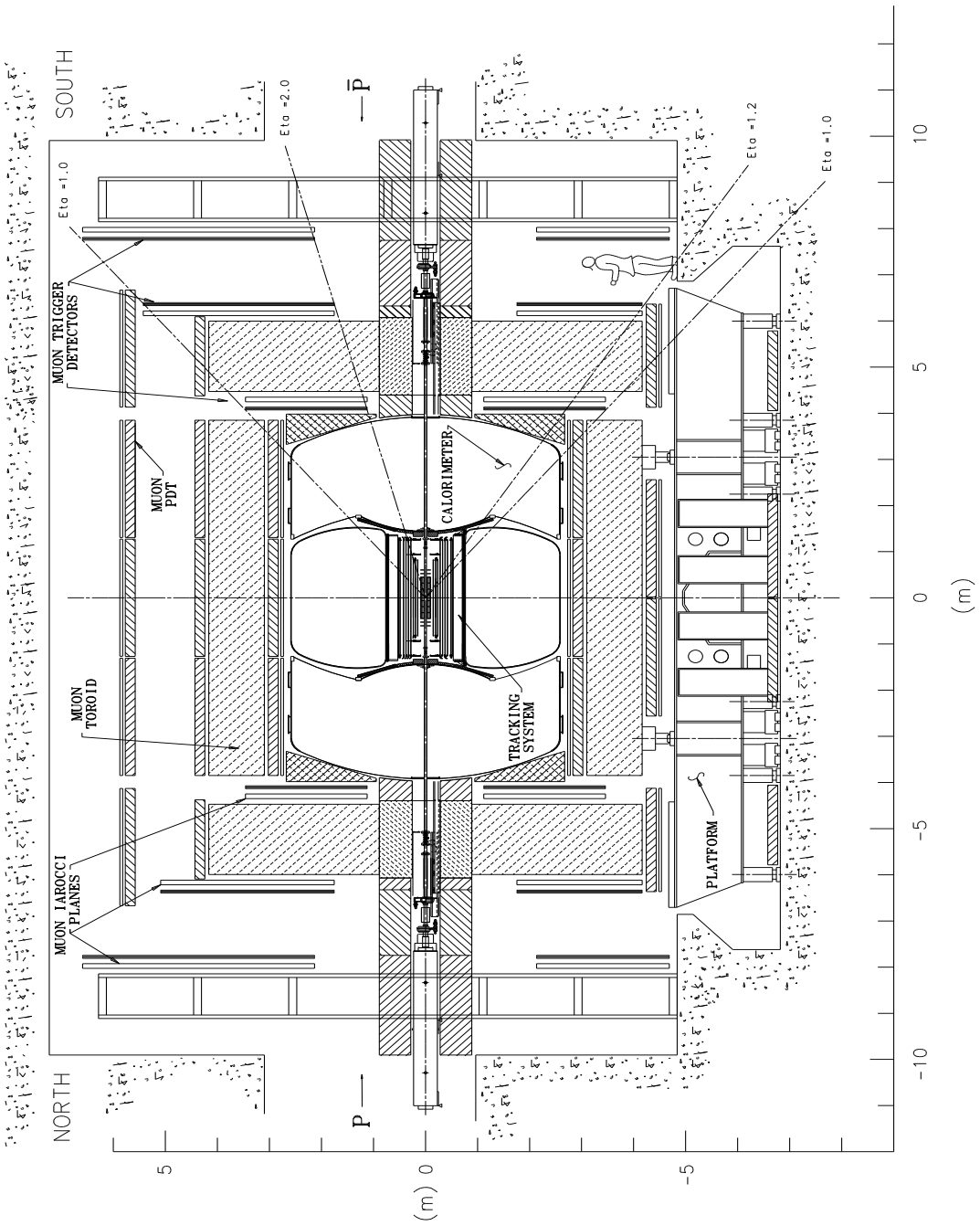

Figure 2.4: DØ Run II detector (side view).

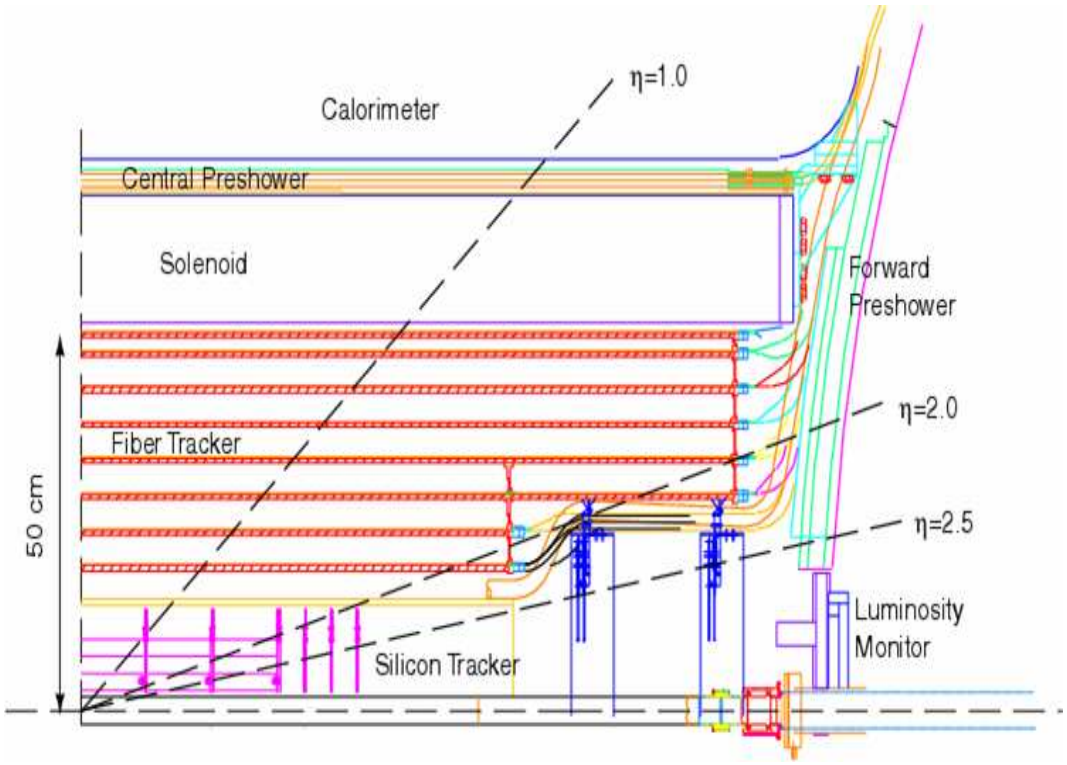

Figure 2.5: The DØ tracking subsystem.

primarily measure the $r-\phi$ coordinate and the disks measure both the $r-\phi$ and $r-z$ coordinates. There are 3 barrels either side of the interaction point. They have a length of 12.0 cm, an inner radius of 2.7 cm and an outer radius of 10.5 cm. Each barrel is composed of 4 layers of rectangular shaped silicon modules known as ladders. Each ladder is double sided and are all encased in a beryllium support structure. There are 12 F-Disks, each disk containing 12 double sided trapezoidal silicon modules know as wedges. There is an F-Disk attached to the end of each barrel plus there are 2 triplets of F-Disks located a small distance from the end of the outermost barrel. The H-Disks are located about 1 metre from the interaction point and are composed of twelve wedges with each wedge composed of two single sided, half wedges. These provide tracking at high $|\eta|$. Figure 2.6 shows a three dimensional view of the SMT. Each ladder or wedge contains readout modules, most with 50 μm pitch, known as strips. In total there are 912 strips with 792,576 channels.

The SMT has a signal to noise ranging from 12:1 to 18:1.

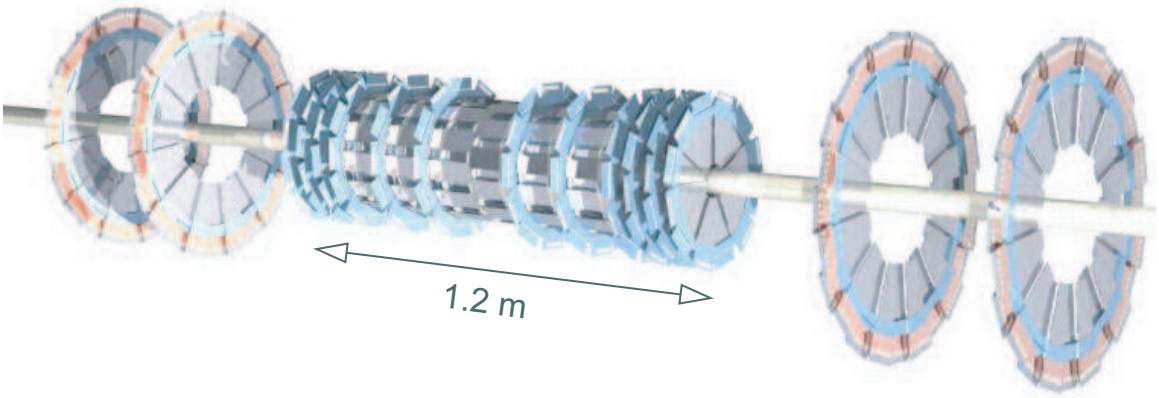

Figure 2.6: The DØ Silicon Microstrip Tracker.

Central Fibre Tracker

The Central Fibre Tracker (CFT) provides track reconstruction and momentum measurement in the region $|\eta| < 1.6$. In addition, the axial layers provide a fast Level-1 trigger. It is composed of scintillating fibres mounted on eight concentric cylinders.

The fibres are composed of a polystyrene core with a thin ($\sim$ 25 μm) acrylic inner layer and a thin ($\sim$ 25 μm) outer layer of fluoroacrylate. The total diameter is 835 μm. This multi-clad fibre is mechanically superior to single-clad fibre. The polystyrene core is doped with 1% p-terphenyl to increase the light yield and small amounts (1500 ppm) of 3-hydroxyflavone which causes a wavelength shift from 340 nm to 530 nm which is transmitted more efficiently in the polystyrene.

The scintillating fibres are grouped into ribbons of 256 fibres with 2 layers of 128 fibres each. The two layers are offset by one half of the fibre spacing in order to minimise gaps. This is known as a doublet layer. These doublet layers are placed on eight concentric support cylinders ranging from r = 20.04 cm to r = 52.15 cm. Each cylinder has an axial layer (with ribbons pointing along the beam axis) and

a stereo layer (with ribbons at $\pm$ 2^o to the beam axis). The stereo layers alternate between these two angles.

The fibres are connected to 7-11 m long waveguides which are chemically and structurally similar to the scintillating fibres but with no dopants. The waveguides are connected to visible light photon counters (VLPC) which are housed in a cryostat underneath the detector. The VLPCs are doped silicon avalanche photo-detectors which operate at 9 K. They are capable of detecting single photons and provide fast response, excellent quantum efficiency ($\geq$75%) and high gain (17,000 to 65,000 electrons per converted photon). The total CFT system contains 76,800 fibres with 200 km of scintillating fibre and 800 km of clear fibre and has a hit efficiency of around 98%.

Solenoid

The dimensions of the solenoid are largely determined from the space available and it is 2.73 m long and 1.42 m in diameter. Other factors that determined its properties were momentum resolution, ability to operate at both polarities, field uniformity and maximum tracking volume. A central field of 2 Tesla was decided upon and this gives a stored energy of 5.6 MJ. The uniform magnetic field is achieved by using two layers of superconductor with the current density in the windings larger at the end of the coil. Inside the tracking volume the field is homogeneous to within 0.5% [27]. The solenoid coil and its cryostat are in total 1.1 radiation lengths (X_0) thick.

Preshowers

The preshower detectors (PS) aid electron identification and provide background rejection both offline and in online triggering. The detectors aid in matching tracks to calorimeter showers and also in correcting the EM energy measurement of the central and end calorimeters for energy loss due to material such as the solenoid. There are two preshower detectors: the central preshower (CPS) and the forward

preshower (FPS). The CPS detector covers the region $|\eta| < 1.3$ and fits in the 5.1 cm gap between the solenoid and the central calorimeter. The two FPS detectors cover the region $1.5 < |\eta| < 2.5$ and are attached to the inner faces of the end calorimeters.

Both detectors are composed of interlocking triangular strips of scintillator. The scintillator is composed of polystyrene doped with 1% p-terphenyl and 150 ppm diphenyl stilbene. At the centre of each strip is a wavelength-shifting fibre. This carries the light out to clear fibres which are in turn connected to VLPCs under the detector in the same way as the CFT.

The CPS consists of three layers: one axial layer with two stereo layers located at $\pm$ 23^o. Between the solenoid and the CPS is a lead plate approximately 1 radiation length thick. Together with the solenoid this provides around $2X_0$ at normal incidence for showering.

The FPS detectors consist of two double layers of scintillator strips separated by a $2X_0$ stainless steel and lead absorber. The double layers are composed of two layers with a crossing angle of 22.5^o with respect to each other. The first layer (upstream of the absorber) is known as the minimum ionising particle (MIP) layer as all charged particles register a minimum ionising hit. This hit can be used to locate the track in η, ϕ and z. The second layer is known as the shower layer. An electron is likely to shower in the absorber and leave a cluster of energy in the shower layer. A heavier charged particle is unlikely to shower and will leave a MIP hit in both layers. A photon or π^0 will leave only a cluster of energy in the shower layer. In the range $1.5 < |\eta| < 1.65$ there is only the shower layer present. This is because in this region the solenoid provides up to $3X_0$ of material for particles to shower in.

Current performance

The combined tracking detectors can locate the primary vertex with a resolution of about 35 μm and can tag b-quark jets with an impact parameter resolution of

less than 15 μm in $r\phi$ for particles with $p_T > 10$ GeV/c. The combined design p_T resolution is $\Delta p_T/p_T = 0.0015 p_T$ where p_T is in GeV/c.[27]

Currently there around 14% of the SMT readout modules disabled and around 2% of the CFT and CPS dead [31]. In the case of the SMT readout most problems are caused by defects on the boards whereas with the CFT and CPS the problem lies in water damage to the VLPC's [31]. In addition, the solenoid is currently operating at around 95.8% of its design current to allow safe operation of the magnet. There has been an increased heat load that is still being investigated.

2.2.2 Calorimeter

The DØ calorimeter is shown in Figure 2.7. It measures the energy of electrons, photons and jets out to $|\eta| \approx 4$. It has essentially been untouched from Run I [32] although the readout electronics have been upgraded to cope with the shorter bunch crossing time. It is a liquid argon sampling calorimeter using depleted uranium, copper and stainless steel absorbers. The depleted uranium acts as a compensator which makes the calorimeter respond almost equally to electromagnetic and hadronic showers. The ratio of the electromagnetic and hadronic response ranges from 1.11 at 10 GeV to 1.04 at 150 GeV. Since it uses liquid argon as the ionising medium, it must be kept at a temperature of around 80K.

Central Calorimeter

The central calorimeter provides coverage of the region $|\eta| \approx 1$ and is divided into three sections which correspond to concentric shells around the beampipe. These are the electromagnetic (EM), fine hadronic (FH) and coarse hadronic (CH) sections with the EM the innermost and the CH the outermost sections respectively. Each section is subdivided into layers which are futher divided into cells approximately 0.1×0.1 in $\Delta\eta \times \Delta\phi$ where $\Delta\phi$ is in radians. The EM section has 4 layers and a total depth of $20.5 X_0$ with the third layer divided into 0.05×0.05 cells corresponding to

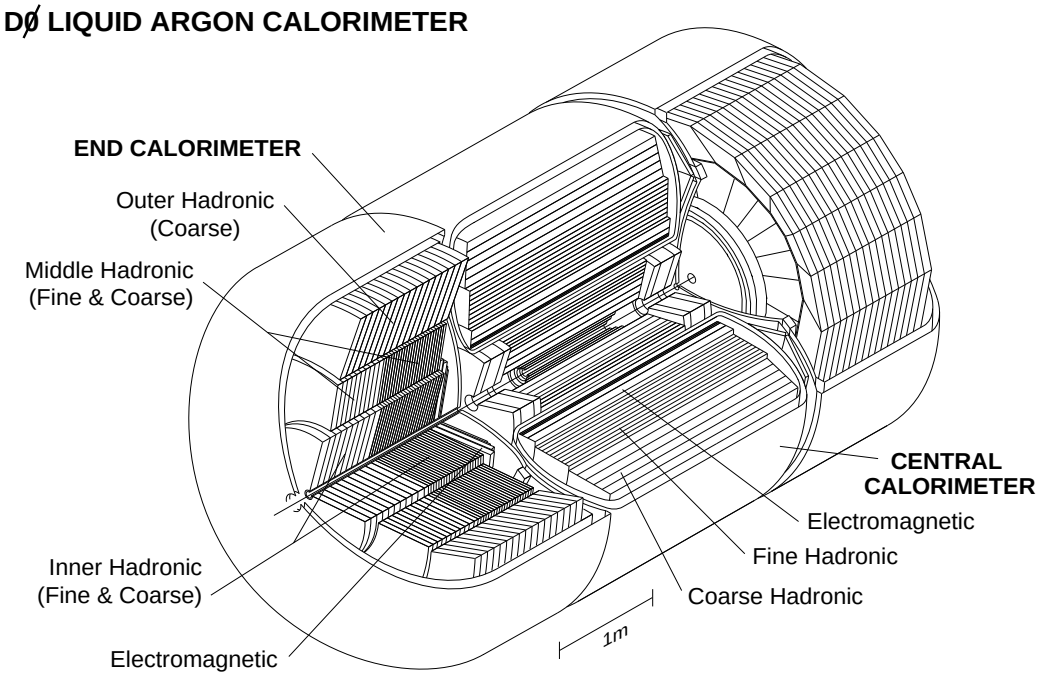

Figure 2.7: The DØ Calorimeter.

the maximum deposition of the EM shower. The FH section is where the majority of the energy from hadronic showers is deposited and has three layers. The CH section has one layer and is present to catch any leakage from the FH section. The total depth of the EM and hadronic calorimeters is approximately 7.2 nuclear absorption lengths.

End Calorimeter

The end calorimeters extend coverage out to $|\eta| \approx 4$ and are divided into four sections: electromagnetic (EM), inner hadronic (IH), middle hadronic (MH) and outer hadronic (OH). The IH and MH sections are split into fine and coarse regions and the the OH section is coarse. The cell segmentation is the same as in the central calorimeter except the finer segmentation in EM layer 3 is only present up to $|\eta| < 2.6$. In addition, beyond $|\eta| > 3.2$, the segmentation increases in both $\Delta\eta$ and $\Delta\phi$.

The total depth is approximately 10.3 nuclear absorption lengths at the smallest angle.

Inter-Cryostat detector

The Inter-Cryostat detector (ICD) is composed of an array of 384 scintillating tiles mounted on the face of both end cryostats. It covers the range $1.1 < |\eta| < 1.4$ which is where there is an overlap between the central and end calorimeters. Here there is a large amount of uninstrumented material including the cryostat walls and support structure. The ICD provides a way of correcting for the energy loss in this region. The scintillator tile size is 0.3×0.3 in $\Delta\eta \times \Delta\phi$ and each tile is subdivided into twelve readout tiles. Optical fibres carry the scintillation light to phototubes outside the magnetic field.

Current performance

The calorimeter performance was measured in test beam studies [32] and the response found to be

$$\begin{aligned} (\sigma_E/E)^2 &= 0.003^2 + 0.157^2/E \quad (EM) \\ (\sigma_E/E)^2 &= 0.032^2 + 0.41^2/E \quad (\pi^{\pm}) \end{aligned} \tag{2.2}$$

where E is in GeV. Currently only 50 out of the 50,000 total calorimeter channels are dead and unrecoverable [31].

2.2.3 Muon system

The muon system was upgraded for Run II and now has full coverage and triggering out to $|\eta| = 2$. It is divided into the wide angle muon system (WAMUS) which covers the region $|\eta| < 1.0$ and the forward angle muon system (FAMUS) which covers the region $1.0 < |\eta| < 2.0$. A toroid magnet with a field of 1.9 T bends the muon trajectory in the r-z plane and either proportional or mini drift tubes are used for identification of muons. In addition, scintillator counters aid in triggering and in reducing backgrounds such as cosmic rays.

Wide angle muon system - WAMUS

The WAMUS system consists of three layers of proportional drift tubes (PDTs), one of which is inside (A-layer) and two of which are outside (B and C layers) the central toroid (see Figure 2.4). The PDTs are typically 2.79×5.59 m^2 and made of rectangular extruded aluminium tubes. Each drift chamber is typically subdivided into 24 cells with each cell ≈ 10.1 cm across with a gold clad, tungsten anode wire down the centre. The gas used is a mixture of argon (84%), methane (8%) and CF_4 (8%) which provides a drift velocity of 10cm/μs and a maximum drift time of 500ns. The hit uncertainty due to diffusion is around 0.4 mm. The A-layer and BC-layers contain 4 and 3 decks of cells respectively. There are two layers of scintillator counters, one located between the calorimeter and PDT A-layer and one outside of the C-layer. An exception to this is on the underside of the detector where some counters are positioned on the outside of the B-layer due to the positioning of support structures. The time resolution is 1.6 ns and there are 986 counters in total.

Forward angle muon system - FAMUS

The FAMUS system consists of three layers of mini drift tubes (MDTs) similarly arranged to the PDT layers, with the A-layer inside the toroid (four decks of cells) and the B and C layers outside the toroid (three decks of cells). They are aligned along the magnetic field lines. Each MDT tube is made from an aluminium extrusion comb with a stainless steel foil cover and is subdivided into eight, 1×1 cm^2, cells each with a gold-tungsten anode wire in the centre. The MDTs use a 90%-10% CF_4-CH_4 gas mixture which is radiation hard and fast, giving a maximum drift time of 60ns. The hit uncertainty is around 0.7mm.

Since the maximum drift time is shorter than the bunch crossing time, scintillators are not needed to match drift tube hits to events. However, the scintillators can reduce backgrounds such as cosmic rays and aid in triggering. There are three

layers of scintillator counters corresponding to the A, B and C layers of MDTs. The segmentation is typically 0.12×4.5 in $\Delta\eta \times \Delta\phi$ where $\Delta\phi$ is in radians.

Current performance

The WAMUS system has a momentum resolution of

$$\sigma(1/p) = 0.36(p - 3.1)/p^2 \oplus 0.03, \tag{2.3}$$

where p is in GeV/c. The FAMUS system has a momentum resolution of around 20% for muons under 40 GeV/c. The overall momentum resolution is defined by the central tracking system for muons with momenta up to 100 GeV/c. After this the muon systems improve resolution.

2.2.4 Trigger

The DØ trigger system has been upgraded for Run II and has three main levels. Level-1 is hardware-based using Field Programmable Gate Array (FPGA) microchips, Level-2 uses FPGAs and microprocessors and Level-3 is fully software based, running on a farm of PCs. There is also a Level-0 which consists of the luminosity monitors mounted symmetrically around the beam pipe, on the inside of the end calorimeters. Its purpose is to trigger on inelastic $p\bar{p}$ collisions.

	Accept Rate	Latency
Collisions	7.6 MHz	
Level-1	10 kHz	4.2 μs
Level-2	1k Hz	$\sim$100 μs
Level-3	50 Hz	$\sim$100 ms

Table 2.2: Trigger rates for Run II.

Table 2.2 shows the design specifications for the trigger in Run II at design luminosity. Note that due to the collaboration's decision to allow a maximum of 5% readout front end busy, the maximum rate out of Level-1 is around 1.6 kHz. This restriction is due to the silicon readout electronics. The times for Level-2 and

Level-3 trigger decisions are variable depending on the event. Currently, with an average luminosity of around $40\text{x}10^{30}\text{cm}^{-2}\text{s}^{-1}$ the rates for Level-1/Level-2/Level-3 are 300-1600/200-850/30-60 Hz. As the luminosity increases the Level-1 rate will rise and the rejection at Level-2 and Level-3 will have to increase. The limiting factors in final output rate of Level-3 are the cost of tape and the speed of the official DØ reconstruction code (RECO).

Level-1 trigger

The upgraded Level-1 trigger utilises a reduced form of the readout for the calorimeter (L1CAL), CFT/PS (known as Central Track Trigger, L1CTT) and muon subsystems (L1MU). In the CAL, cell energies are summed to form *trigger towers*. A trigger decision is made based on the energy of a tower exceeding a preset value. In addition, a trigger decision can be made on global quantities such as total transverse energy (E_T) or missing E_T. The CTT trigger is based upon $r-\phi$ hit patterns in 4.5^o sectors of the CFT. A decision is based on the hit pattern being consistent with a track of one of four software programmable p_T thresholds. There must also be energy deposition in the CPS consistent with the trigger track. The FPS requires a spacial match between hits in the MIP and shower layers. The L1MU trigger utilises information from the muon scintillator counters, muon wire chambers and tracks from L1CTT. Scintillator and drift tube hits in the A,B and C layers are matched with CFT sectors containing tracks.

The output of the separate detectors is logically combined into a maximum of 128 different triggers, the output of which is called a trigger bit. If all the logical requirements of a particular trigger are satisfied for an event, then that particular trigger bit is said to be set. Each subdetector buffers the readout awaiting a Level-1 accept (if any one bit is set). If this occurs, then the data are digitised (if not already done so) and passed into the Level-2 trigger.

Level-2 trigger

The Level-2 trigger [33] is required to handle a 1.6kHz input and provide a factor of 10 rejection. It achieves this task by refining the information that the Level-1 trigger provides and also correlating trigger information from the different subdetectors. For each Level-1 trigger bit there is a corresponding Level-2 trigger bit.

The Level-2 trigger consists of preprocessors for each subdetector, namely L2CAL, L2CTT and L2MU, and a global processor (L2Global) which makes the trigger decision. The preprocessors handle data specific to the individual subdetectors, but in general, prepare lists of physics objects (such as muons, electrons or jets) to be sent to L2Global. L2Global then makes trigger decisions based on the objects found by the preprocessors. This may involve the correlation of objects in different subdetectors (such as calorimeter/track matching), the calculation of kinematic variables from multiple objects or requiring object quality cuts. The actions of L2Global will depend on which Level-1 trigger bits have fired with an individual set of algorithms for each Level-1 trigger bit. Thus each Level-1 trigger bit is either confirmed or rejected with the output forming the 128-bit Level-2 trigger bit mask. If any of the Level-2 trigger bits are set then the event passes and the whole detector is read out and passed to the Level-3 trigger.

In addition to the preprocessors mentioned above, there is a Level-2 silicon track trigger (L2STT) preprocessor currently being commissioned. This takes tracks from the L1CTT and adds hits from the axial strips of the silicon ladders which define points in $r-\phi$. This additional information will improve the p_T resolution of L2CTT tracks and also allow triggering on tracks displaced from the primary vertex. The impact parameter resolution is approximately 20 μm for high p_T ($>$ 50 GeV/c) simulated single muons.

Level-3 trigger

The Level-3 trigger is a high level, software based, fully programmable trigger. It refines the physics objects created at Level-2, creates new, more sophisticated objects, finds relations between objects and makes the final decision to keep the event. There is full access to the detector readout and a limited reconstruction of each event is performed. It has approximately 50-100 ms in order to do this.

The software runs on a farm of standard PC computers running the Linux operating system. Each individual PC is known as a Level-3 node and runs an independent instance of the Level-3 software. Each instance sequentially processes complete events and if accepted, the event is passed on to the datalogger where it is sent to tape.

Figure 2.8 shows the hierarchy of objects in the Level 3 framework. For each Level-2 trigger bit there is at least one associated *filter script*. There is no limit, except for available processing power, on the number of filter scripts associated to a Level-2 bit. Each filter script defines a number of *filters* that determine the Level-3 conditions for this trigger bit. Filters come in two main types. The most common type are physics object filters that apply selection cuts on physics objects created by a *physics tool*. In Figure 2.8, filters 1, 2 and 3 are of this type. The second type of filter is a relational filter. This type of filter compares the output of other filters. In Figure 2.8, filter 4 is of this type.

Physics tools provide a list of `L3PhysicsResults` objects for the filters to cut on. Examples include electrons, muons, jets, tracks and taus. The physics tools in turn generally call at least one *data tool* that performs most of the computation. Examples of data tools include tracking, vertexing or clustering tools. Data tools can call other tools and they cache their results to ensure that the tool runs once per event despite multiple calls. Only tools known as *unpack tools* have access to the raw data. These generally process the data in a form acceptable to the data tools.

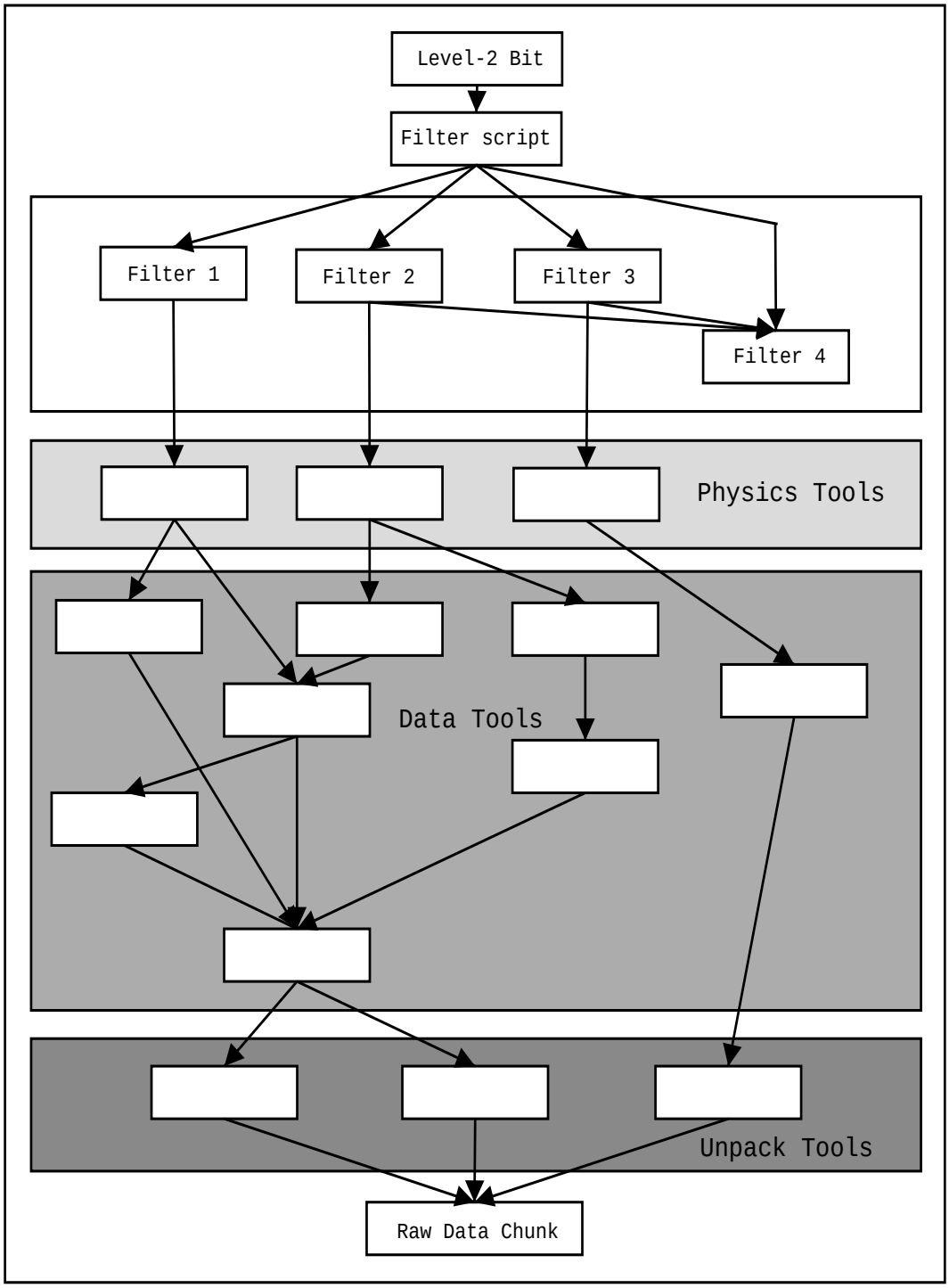

Figure 2.8: Flow diagram illustrating the hierachy of objects in the Level-3 trigger framework. Filters and tools are called in top to bottom order. The Raw Data Chunk (RDC) is described in Section 2.2.5.

The software interface for the filters and tools is called `ScriptRunner`. It takes as input a *triggerlist* which defines the filter scripts and contains filter and tool *refsets*. A refset is a set of programmable parameters that may be algorithmic in the case of a data tool or kinematic in the case of a filter. Refsets allow quality definitions to be defined such as loose, medium or tight muons.

At the beginning of a run, `ScriptRunner` parses the triggerlist, initialises all required tools and builds an execution tree. Assuming no errors occur, `ScriptRunner` is then ready to accept data.

When ScriptRunner receives an event it runs an execution tree for each Level-2 bit that is set. Each filter script is executed in turn with each filter and associated tools executed in script order. If a filter fails or all of the filters in the filter script pass, the next filter script associated with that Level-2 bit is executed. If none exists, `ScriptRunner` progresses to the next set Level-2 bit. If all the filters in any one filter script pass, then that event, together with information on which filter scripts passed and failed is sent to the datalogger and written out.

An example of this process is the impact parameter framework, developed by myself, and described in more detail in the following two Chapters. At the top of the chain is the filter `L3FIP` which is a filter to place cuts on the impact parameter of tracks. This filter calls the physics tool `L3TIPTracker` which in turn calls the tracking data tool `L3TGlobalTracker` and vertexing data tools `L3TXYVertex` and `L3TCFTVertex`. If these tools have already been called in this event they just return their cached results otherwise they execute their algorithms. This chain inevitably leads to one or more unpack tools, in this case the clustering tools `l3fsmtunptool` and `l3fcftunpack`.

When all the tools in the chain have output their results, `L3TIPTracker` uses the primary vertex position and calculates the impact parameter significance for the list of tracks. The results are stored in a list of `L3IPTrackPhysicsResults` which is returned to the filter, `L3FIP`. If any of the objects pass the cuts specified in the

filter refset then the filter returns true. If all the other filters in that particular filter script (such as a muon filter) return true then that event is written out.

2.2.5 Software

Most of the reconstruction and programmable trigger (Level-2 and Level-3) software is written in C++. Both the Level-3 and offline reconstruction frameworks utilise an object oriented structure. The DØ event data model (EDM) provides a structure for the offline storage, processing and analysis of data. All the data for an event are stored in the `Event` object as a collection of "chunks". For example the raw data are stored in the `RawDataChunk` and the Level-3 information is stored in the `L3Chunk`. Each component of the reconstruction software accesses the chunk or chunks that it requires, runs all algorithms and places a new chunk into the `Event`. An example would be vertexing which would read in the relevant tracking chunks and add the `VertexChunk`.

Chapter 3

Level-3 Vertexing

3.1 Introduction

The location of the primary vertex is an important input parameter for many Level-3 filters. The z coordinate can be used by the jet and missing E_T filters to calculate a more accurate E_T and sharpen their turn-on curves. Many triggers also use the z position to filter events that are situated within the tracking fiducial region. The full 3-D primary vertex is used primarily for track impact parameter and b-tagging calculations which allow the filtering of events based on lifetime. Almost all physics areas at DØ utilise the Level-3 vertexing tools.

The time budget per event at Level-3 is around 50ms. The majority of this time is spent on clustering and tracking, therefore any vertexing algorithms must be fast. A suitable balance between speed and performance is the aim for any tool at Level-3. To aid in timekeeping, the vertex finding is split into z coordinate finding and x-y coordinate finding. With this split, filters requiring only the z coordinate do not have to call the more accurate x-y coordinate finding.

3.2 Clustering and tracking

Both vertexing algorithms are track based and require a set of tracks as input. The packages `l3fsmtunptool` and `l3fcftunpack` access the raw data chunks for

the SMT and CFT and perform clustering from strips and fibres respectively [34] [35]. The tracking package `l3ftrack_global` uses these clusters to find global tracks (SMT + CFT tracks) [36].

3.3 Vertexing algorithms

3.3.1 Vertexing in z - Histogramming method

The z finding algorithm utilises a p_T weighted histogramming approach. All tracks possessing > 8 stereo CFT hits are binned in the z range (-100cm,100cm) according to their Z_0 track parameter which is the z position of the track helix at the distance of closest approach to the origin in the x-y plane (Appendix A). The bin width is 1cm. The number of tracks in each bin, n, is then multiplied by the $\sum p_T$ of tracks within that bin. The resulting bin value is then $n \sum p_T$. The maximum adjacent 2 bins are selected and the z position calculated as the mean Z_0 of the tracks present in those bins. Choosing the highest adjacent 2 bins is required since the Z_0 of tracks from the hard scatter can be distributed over 1-2 cm. Using the p_T weight to select the correct bins makes it robust against minimum bias vertices present. To help prevent fake, high p_T tracks from biasing the vertex, a maximum p_T weight of 10 GeV/c is imposed. The tool returns only one primary vertex. If no tracks pass the selection criteria, no vertex is returned rather than the origin.

Figure 3.1 illustrates the difference between a straight histogramming method and the p_T weighted histogramming method for a $B_s \to D_s\pi$ Monte Carlo (MC) event. The MC has additional minimum bias events added with the probability following a Poisson distribution with mean 0.8. In this event the hard scatter vertex lies at $z \sim +30$ cm and a minimum bias vertex lies at $z \sim -10$ cm. The histogramming method with no p_T weight finds the minimum bias vertex. The p_T weighted histogramming method finds the hard scatter vertex. The vertex returned in the former case has a very large residual. In all of the following, the "residual" is defined as the distance between the found vertex and the MC true hard scatter vertex.

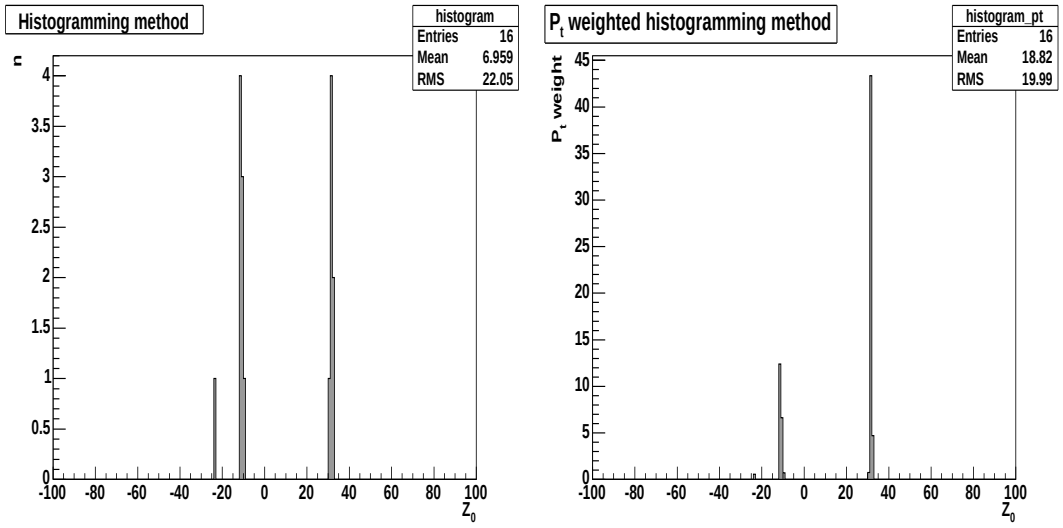

Figure 3.1: Comparison of histogramming and p_T weighted histogramming approach on a $B_s \to D_s\pi$ event. The MC has additional minimum bias events added with the probability following a Poisson distribution with mean 0.8. The x axis displays the track Z_0 in 1cm bins in the range -100cm to 100cm. The y axis is the number of tracks, n, for the histogramming method (left) or $n\sum p_T$ for the p_T weighted histogramming method (right). Without the p_T weight, the histogramming method finds the minimum bias vertex ($z \sim -10$ cm) rather than the hard scatter vertex ($z \sim +30$ cm).

3.3.2 Vertexing in x-y - Impact parameter minimisation

To calculate the vertex position in the x-y plane an impact parameter minimisation algorithm is used [37],[38]. The tracks are approximated by straight lines, linearised at the closest point to the mean beamspot position (see Section 3.5). Figure 3.2 shows the conventions used in the following derivation of vertex position. By definition

$$(\underline{r} + t\underline{\hat{d}} - \underline{V}) \cdot \underline{\hat{d}} = 0, \tag{3.1}$$

which gives

$$t = \underline{V} \cdot \underline{\hat{d}}. \tag{3.2}$$

The vertex is calculated by minimising the following χ^2 function

$$\chi^2 = \sum_{a}^{Ntracks} \frac{(d_0^a)^2}{(\sigma_{d_0}^a)^2} + \sum_{i=x,y} \frac{(b_i - V_i)^2}{(\sigma_i^b)^2}, \tag{3.3}$$

where the track subscript a corresponds to an individual track and the subscript i refers to x-y coordinates. The first term is the track contribution and can be

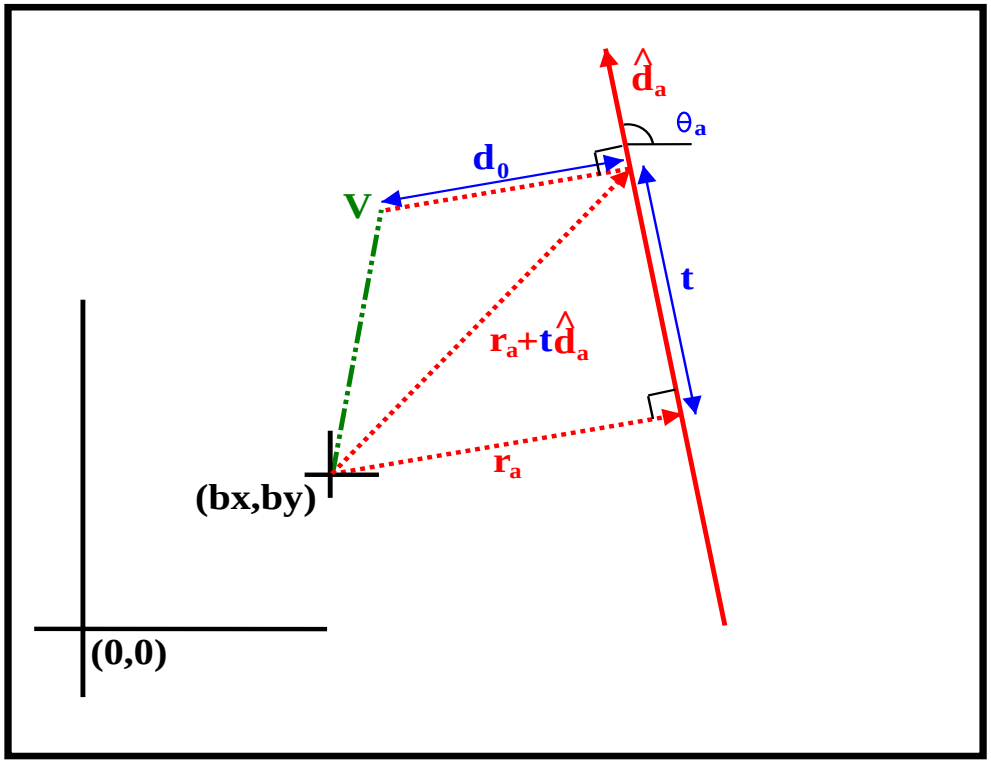

Figure 3.2: Definition of geometrical variables in the impact parameter minimisation derivation. V is the vertex position, bx and by are the mean beamspot position (Section 3.5). The variables d_0, t and θ (0,2π) are scalar quantities. $\hat{\underline{d}}$ is the linearised track unit vector.

expressed as

$$\sum_{a}^{Ntracks} \frac{\left|\underline{r}_a + \hat{\underline{d}}_a[\underline{V} \cdot \hat{\underline{d}}_a] - \underline{V}\right|^2}{(\sigma^a_{d_0})^2}. \tag{3.4}$$

The second term is the beamspot constraint with b_i the beam position and σ^b_i the corresponding width. By transforming into the system where the beamspot is the origin (as in Figure 3.2) b_i is zero and the expression simplifies:

$$\chi^2 = A - 2\sum_i V_i B_i + \sum_{ij} V_i C_{ij} V_j, \tag{3.5}$$

where

$$A = \sum_{a}^{Ntracks} \frac{r_a^2}{(\sigma^a_{d_0})^2} \qquad B_i = \sum_{a}^{Ntracks} \frac{r_{ia}}{(\sigma^a_{d_0})^2} \qquad C_{ij} = \frac{\delta_{ij}}{(\sigma^b_i)^2} + \sum_{a}^{Ntracks} \frac{\delta_{ij} - d_{ia}d_{ja}}{(\sigma^a_{d_0})^2}. \tag{3.6}$$

Differentiating with respect to V and equating to zero yields the following relation for the vertex position, which is true in any coordinate system

$$V_i = (C_{ij})^{-1} B_j. \tag{3.7}$$

Using the substitution,

$$d_a = (\cos\theta_a, \sin\theta_a), \tag{3.8}$$

we can express C as

$$C_{ij} = \frac{\delta_{ij}}{(\sigma_i^b)^2} + M_{ij}, \tag{3.9}$$

where

$$M_{ij} = \begin{pmatrix} M_{11} & M_{12} \\ M_{21} & M_{22} \end{pmatrix} = \begin{pmatrix} \sum_a \frac{sin^2\theta_a}{(\sigma^a_{d_0})^2} & -\frac{1}{2}\sum_a \frac{sin2\theta_a}{(\sigma^a_{d_0})^2} \\ -\frac{1}{2}\sum_a \frac{sin2\theta_a}{(\sigma^a_{d_0})^2} & \sum_a \frac{cos^2\theta_a}{(\sigma^a_{d_0})^2} \end{pmatrix}. \tag{3.10}$$

To obtain the expression for the vertex error, a transformation of the origin to the vertex position is performed. In this system

$$r_x = d_0 \cos\theta, \qquad r_y = d_0 \sin\theta. \tag{3.11}$$

Assuming the vertex error is independent of θ, ie

$${\sigma_V}^2 = \left(\frac{\partial V}{\partial d_0}\right)^2 {\sigma_{d_0}}^2, \tag{3.12}$$

the error is given by

$$\begin{pmatrix} \sigma^2_{Vx} \\ \sigma^2_{Vy} \end{pmatrix} = \frac{1}{(\det C)^2} \begin{pmatrix} C^2_{22}M_{22} + C^2_{12}M_{11} + 2C_{12}C_{22}M_{12} \\ C^2_{11}M_{11} + C^2_{12}M_{22} + 2C_{12}C_{11}M_{12} \end{pmatrix}. \tag{3.13}$$

3.4 Error parameterisation

The dominant error contributions to the track d_0 (also known as distance of closest approach, DCA) are due to the number of SMT hits and multiple scattering (MS). The former contribution, σ_{NSMT}, can be parameterised from MC events and is the error quoted by the tracking tool [36]. Multiple scattering in the plane transverse to the beam is expected to be inversely proportional to $p_T = p\sin\theta$, where θ is the

polar angle relative to the beam or z axis and p is the momentum. Additionally, MS is proportional to the square root of the distance travelled through the material [39]. This distance is inversely proportional to $\sin\theta$ assuming the material is distributed along cylinders aligned with the beam. Therefore MS is inversely proportional to p_{scat}, where

$$p_{scat} = p\sin^{3/2}(\theta) \tag{3.14}$$

The total d_0 error, including the beam width in x and y, σ_{beamx} and σ_{beamy}, is given by

$$\sigma_{d_0}^2 = (\sigma_{NSMT})^2 F(p_{scat})^2 + \sigma_{beamx}^2 + \sigma_{beamy}^2, \tag{3.15}$$

where $F(p_{scat})$ is the correction to the error due to MS and is to be determined. Figure 3.3 shows the width of the d_0 significance (d_0/σ_{d_0}) distribution as a function of p_{scat} in data, before the p_{scat} correction. The data are binned as a function of p_{scat} and the resultant distributions fitted with a Gaussian. The effect of MS is to

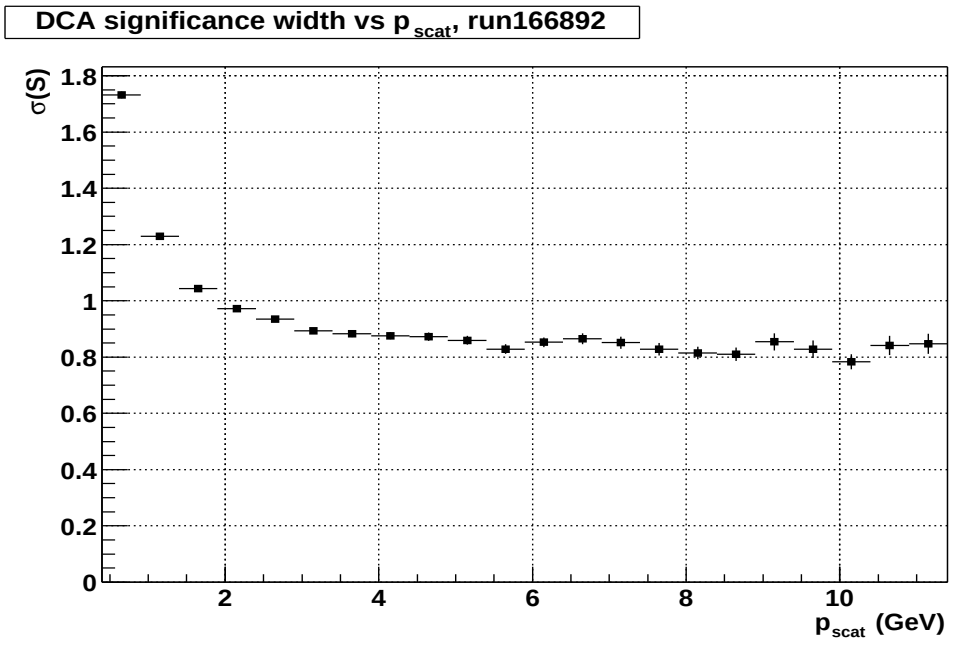

Figure 3.3: DCA significance as a function of p_{scat} for data.

cause large deviations from σ_{NSMT} at small p_{scat}. Additionally, at large p_{scat} values,

the significance is offset from one. Considering this and that the amount of multiple scattering is inversely proportional to p_{scat}, the correction $F(p_{scat})$ takes the form

$$F(p_{scat}) = \sqrt{c_0^2 + c_1^2/p_{scat}^2}. \tag{3.16}$$

Substituting into Equation 3.15 yields

$$\sigma_{d_0}^2 = \sigma_{NSMT}^2 c_0^2 + \sigma_{NSMT}^2 c_1^2/p_{scat}^2 + \sigma_{beamx}^2 + \sigma_{beamy}^2. \tag{3.17}$$

In MC, the last two terms of Equation 3.17 vanish and the exact vertex position, hence d_0, is known. Figure 3.4 shows the d_0 significance vs p_{scat} in QCD MC. By fitting this plot, the constants c_0 and c_1 can be extracted. Applying this correction factor to data, the d_0 significance becomes approximately 1 for all p_{scat}, as shown in figure 3.5.

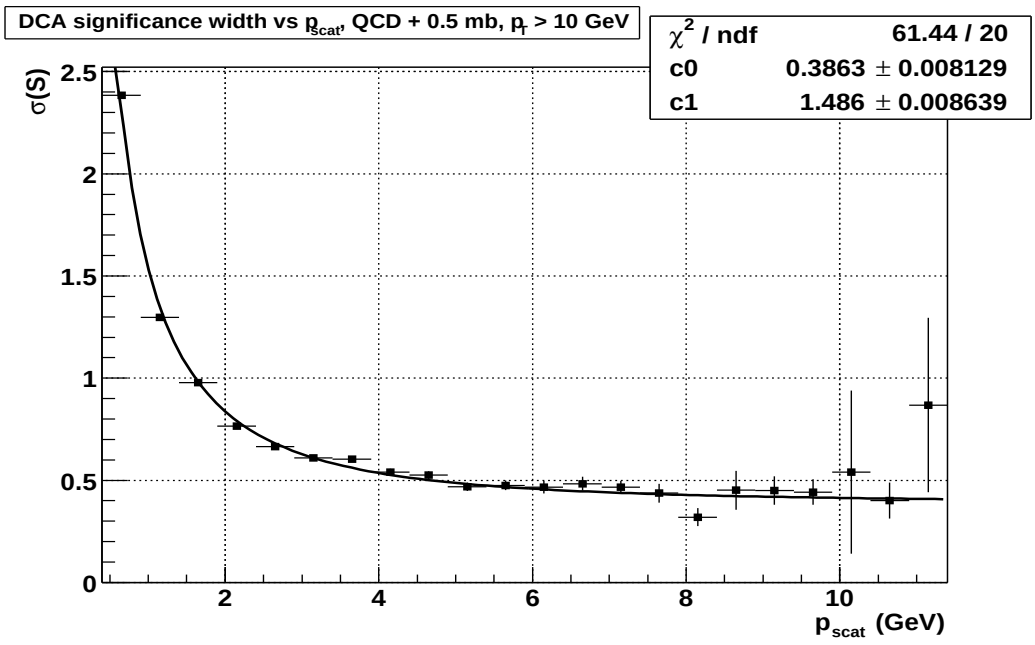

Figure 3.4: DCA significance as a function of p_{scat} for QCD MC.

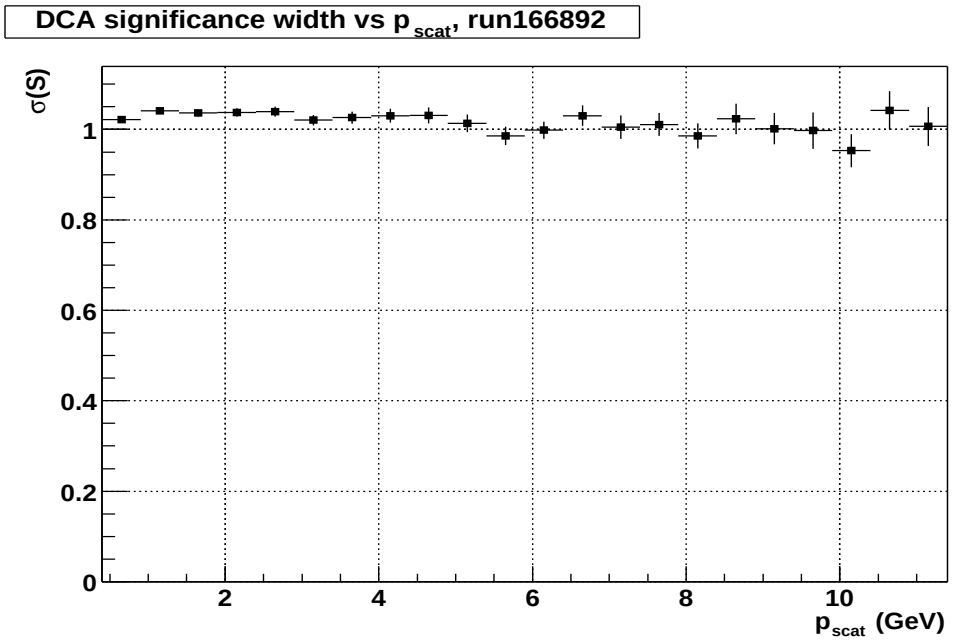

Figure 3.5: Corrected DCA significance as a function of p_{scat} in data.

3.5 Beam parameters

The beam position in data is not only displaced from the origin but has a tilt in z (see Figures 3.28 and 3.29, Section 3.8). This is assumed to be linear and can be expressed as

$$x = X_0 + A_x z \qquad y = Y_0 + A_y z. \tag{3.18}$$

The impact parameter, d_0, of any track, a, with respect to the origin will have an extra contribution due to the displaced beamspot. This is given by

$$d(\phi_a, z_a) = (X_0 + A_x z_a)\sin\phi_a - (Y_0 + A_y z_a)\cos\phi_a, \tag{3.19}$$

where ϕ_a is the azimuthal angle of track a (Appendix A). Figure 3.6 shows the d_0 as a function of ϕ in data. To evaluate the beam parameters, a large collection of tracks from different events is collected and the following χ^2 function minimised

$$\chi^2 = \sum_{a}^{Ntracks} \frac{(d_a - d(\phi_a, z_a))^2}{\sigma_a^2 + \sigma_{beamx}^2 + \sigma_{beamy}^2}. \tag{3.20}$$

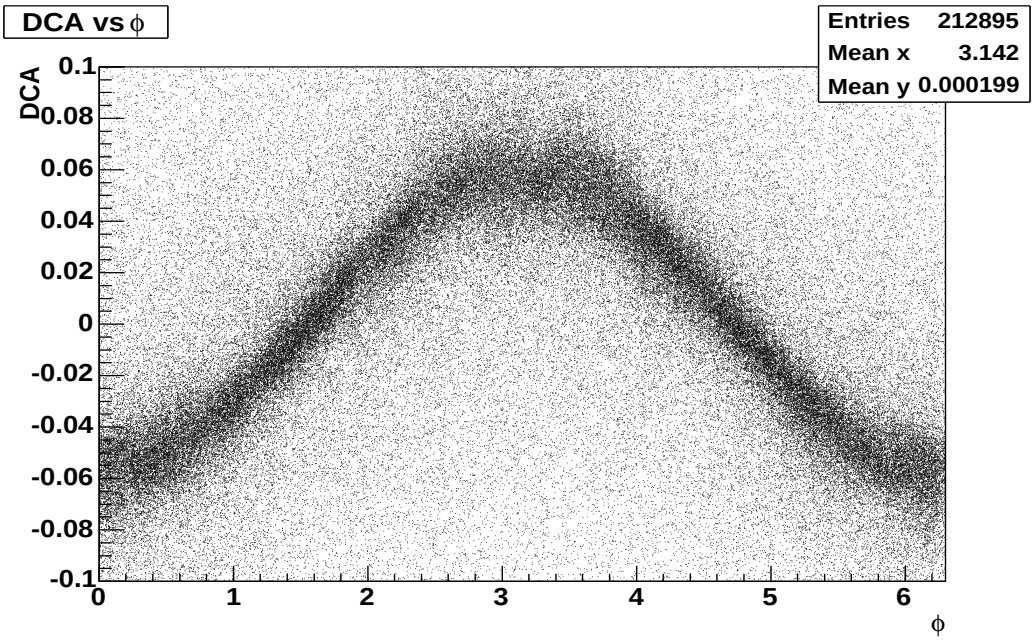

Figure 3.6: Track DCA (cm) versus ϕ in data.

The package that performs this calculation is called `vertex_examine` [40]. Examine packages run online in parallel with `ScriptRunner`. They receive a subset of events in real time, provided by the Data Distributor. `vertex_examine` runs Level-3 tracking on the raw data and performs an iterative minimisation. On the first iteration, all tracks are used. Tracks satisfying $d_0 > 0.1$cm with respect to the resultant beamspot are excluded and the parameters re-calculated. This process is repeated until no more tracks are removed or there are less than 10% of the tracks left. The package calculates the beam position every 5 to 10 minutes and has a precision of around 2.5 μm in x and y and 10 μ rad in the tilt.

The 4 parameters X_0, Y_0, A_x and A_y are passed to the Level-3 tools via the triggerlist at the start of the run. The x-y vertex finder uses these values, together with the z coordinate of the vertex to calculate the position of the beamspot on an event by event basis. The beam width in x and y is taken to be 30μm [41].

3.6 Combined vertexing method

Once the x-y vertex finder acquires the z position it then uses an iterative process to find the set of tracks that form the best vertex. Figure 3.7 illustrates this technique. Before impact parameter minimisation, tracks are selected using the following criteria

- Total number of stereo hits ≥ 7
- Number of axial SMT hits ≥ 2
- $|Z_0 - PV_z| < 1\text{cm}$
- $|d_0/\sigma_{d_0}| < 3$

The first cut reduces the number of fake tracks. The cut on the number of SMT hits ensures a good resolution in the x-y plane. To reduce track contamination from minimum bias vertices, a cut is placed on the distance between the track Z_0 and the returned primary vertex z coordinate. To reduce contamination from secondary vertices, the track must be consistent with the mean beam position within errors. There is also a variable p_T cut on the tracks that can be specified at run time in the triggerlist. This cut will be investigated in Section 3.7.3.

If two or more tracks pass the selection criteria, the vertex and χ^2 are calculated with all tracks. Each track is sequentially removed and the vertex recalculated. The track that causes the maximum change in χ^2 per degree of freedom, $\Delta\chi^2_{max}$ is removed from the set of tracks provided $\Delta\chi^2_{max}$ is larger than the value Δ_{max}. This process is repeated until a set of tracks is found such that $\Delta\chi^2_{max} < \Delta_{max}$, in which case the vertex position is returned, or there is only 1 track remaining, in which case the beamspot is returned. The optimal Δ_{max} cut will be determined in Section 3.7.3.

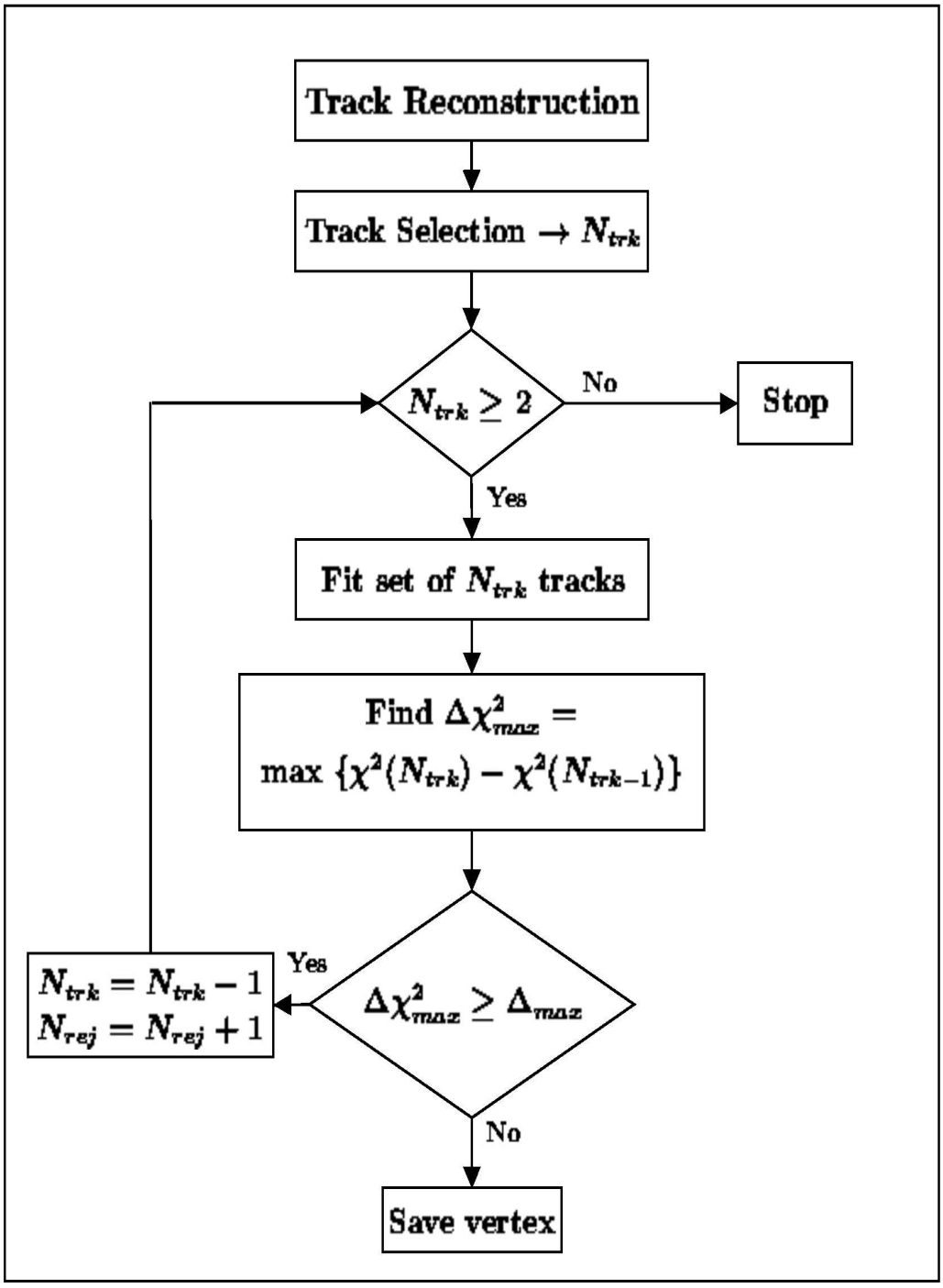

Figure 3.7: Procedure for finding primary vertices.

3.7 Monte Carlo performance

In this section the performance of both the z and x-y vertex algorithms are evaluated on MC samples.

3.7.1 Samples

The MC samples used to measure the performance of the z vertex tool were chosen to represent all types of events that the tool may be used on.

- $B_s \rightarrow D_s\pi$ + 0.8 min bias, generated with p14[1], 5000 events
- $t\bar{t} \rightarrow$ jets + 0.8 min bias, generated with p14, 5000 events
- Associated Higgs production, $Z^*H \rightarrow b\bar{b}b\bar{b}$ + 0.8 min bias, generated with p14, 5000 events ($M_{Higgs} = 100$ GeV/c^2). This sample will just be referred to as $H \rightarrow b\bar{b}b\bar{b}$.
- $Z^0 \rightarrow \mu\mu$ + 0.5 min bias, generated with p13[2], 5000 events
- $W \rightarrow \mu\nu$ + 0.5 min bias, generated with p13, 2500 events

For the performance of the x-y vertex finder, only the $B_s \rightarrow D_s\pi$ and the $H \rightarrow b\bar{b}b\bar{b}$ MC samples were used for studies. This is because, at present, only these types of events will require b-tagging at the trigger level.

3.7.2 z performance

Figures 3.8 to 3.12 show the residual between the returned z vertex and the true MC vertex and the number of tracks associated to the vertex for five different types of MC event with a track p_T cut of 1 GeV/c. The residual distributions are fitted with a double Gaussian distribution centred at zero. Table 3.1 summarizes the results.

[1]Version 14 of the official DØ production release software.
[2]Version 13 of the official DØ production release software.

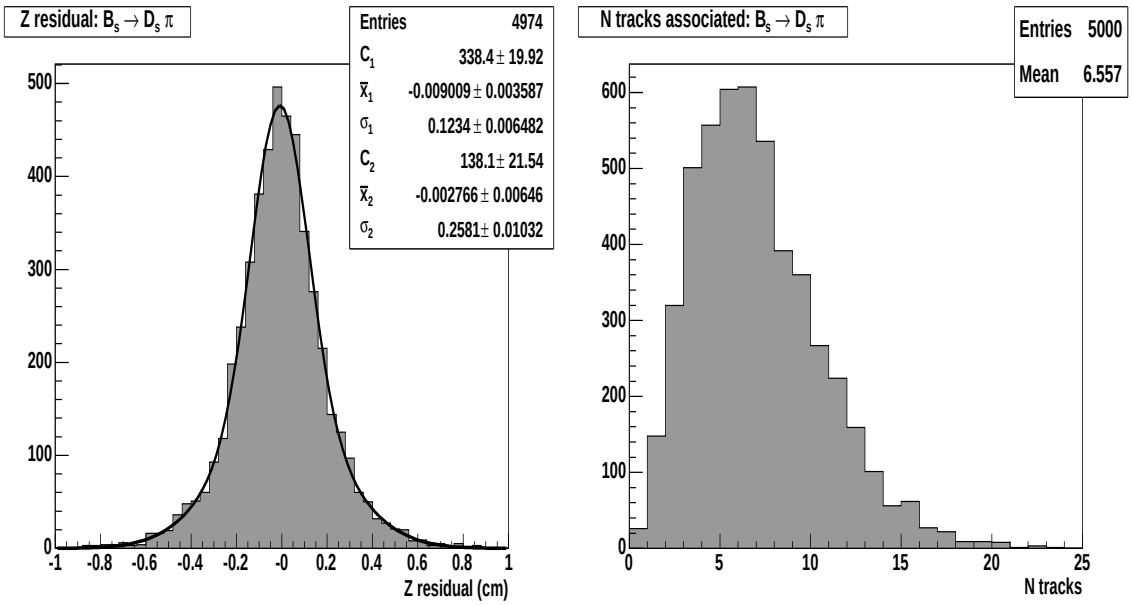

Figure 3.8: $B_s \to D_s\pi$ z residual and number of associated tracks, $p_T > 1$ GeV/c.

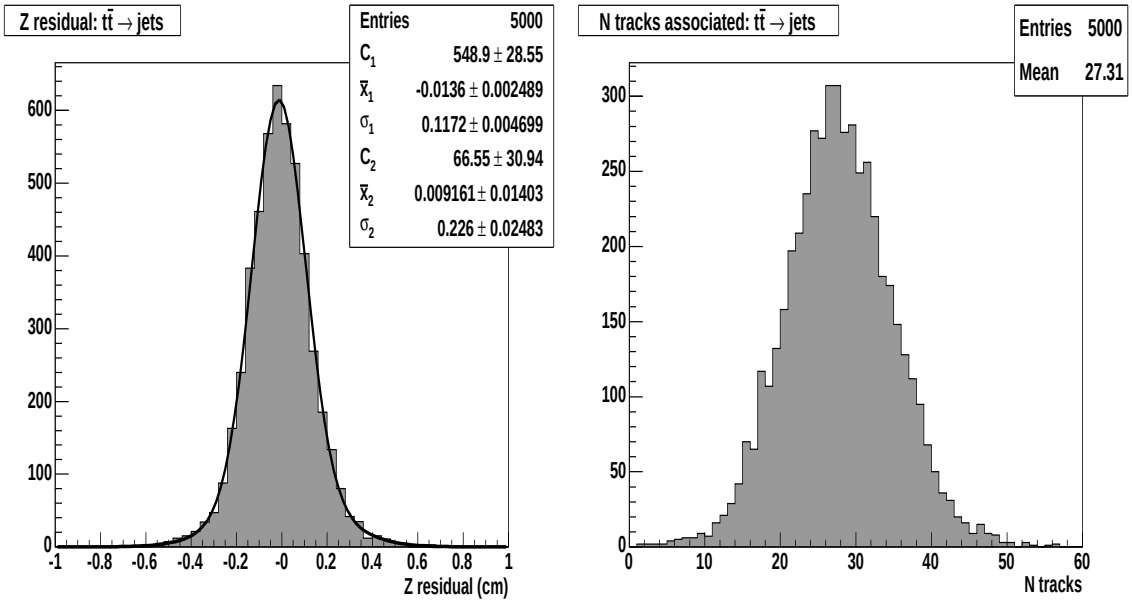

Figure 3.9: $t\bar{t}$ z residual and number of associated tracks, $p_T > 1$ GeV/c.

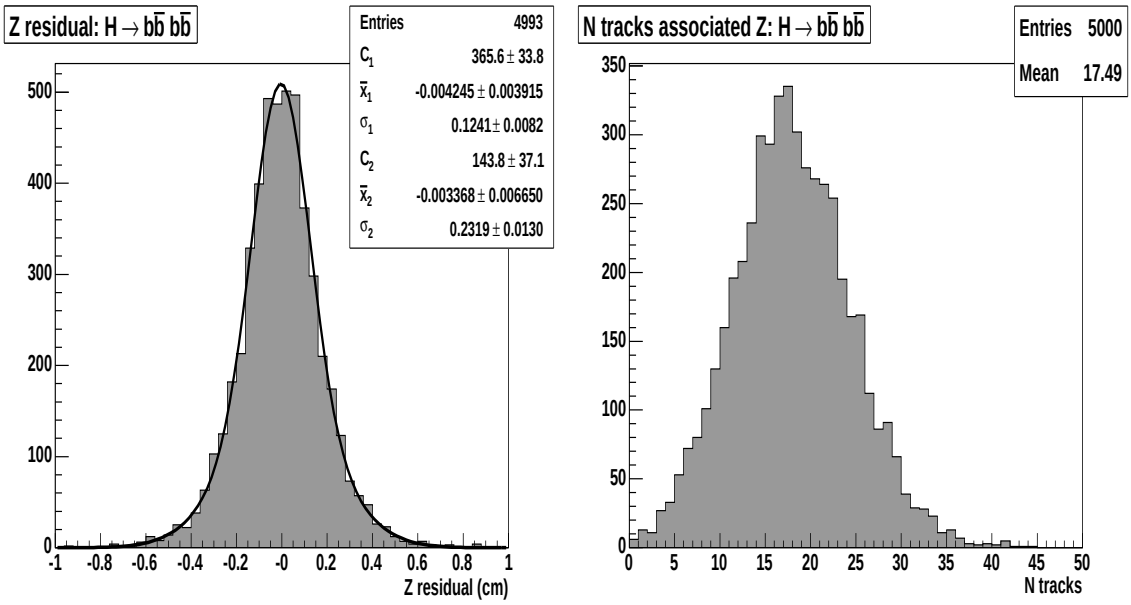

Figure 3.10: $H \to b\bar{b}b\bar{b}$ z residual and number of associated tracks, $p_T > 1$ GeV/c.

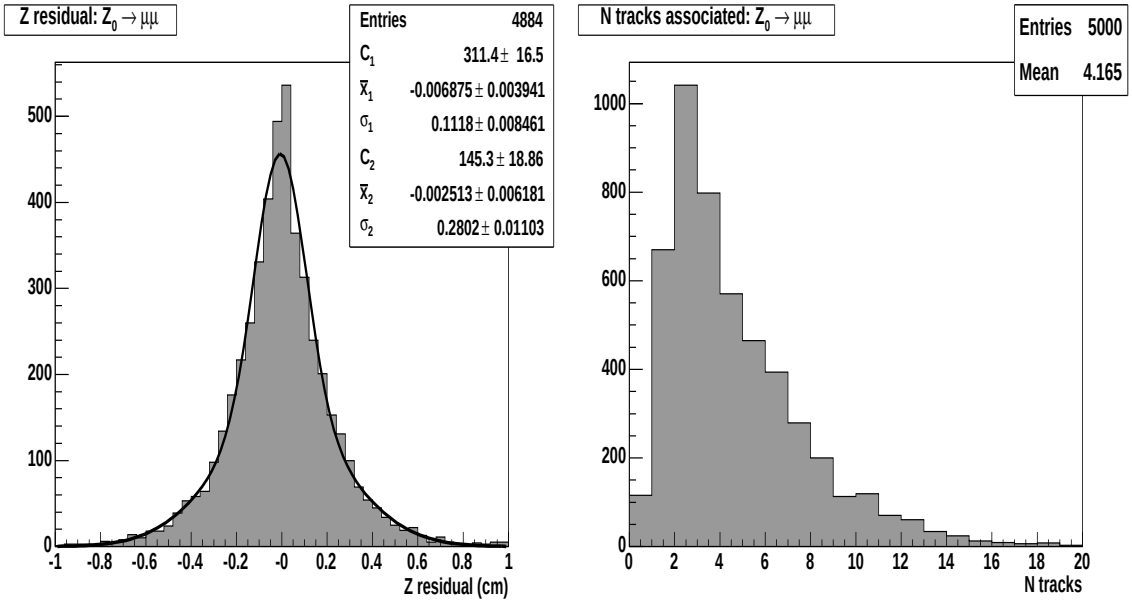

Figure 3.11: $Z \to \mu\mu$ z residual and number of associated tracks, $p_T > 1$ GeV/c.

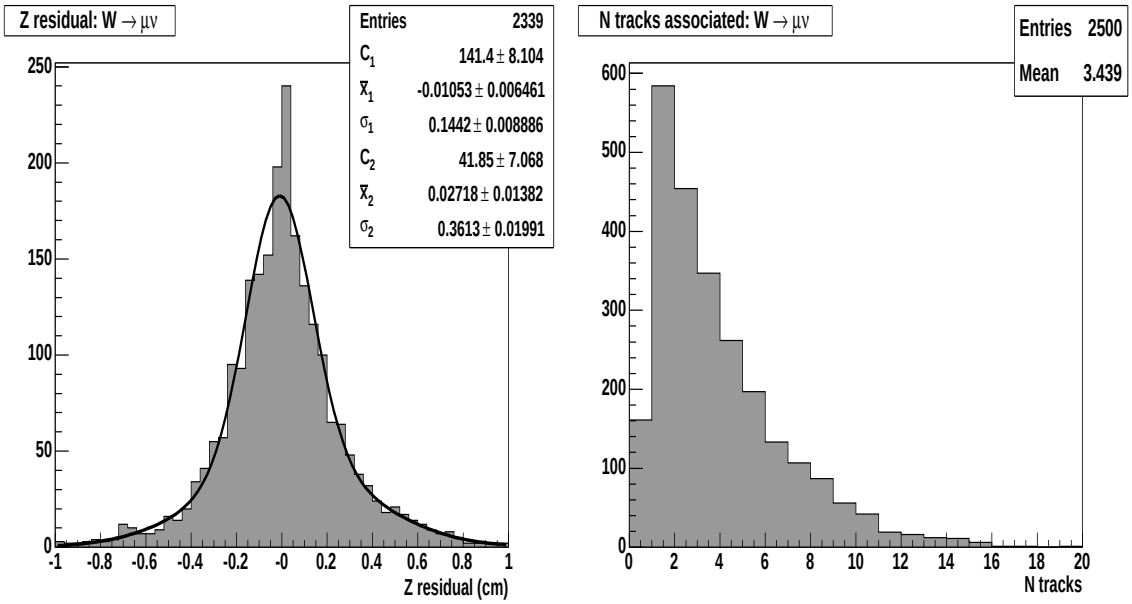

Figure 3.12: $W \to \mu\nu$ z residual and number of associated tracks, $p_T > 1$ GeV/c.

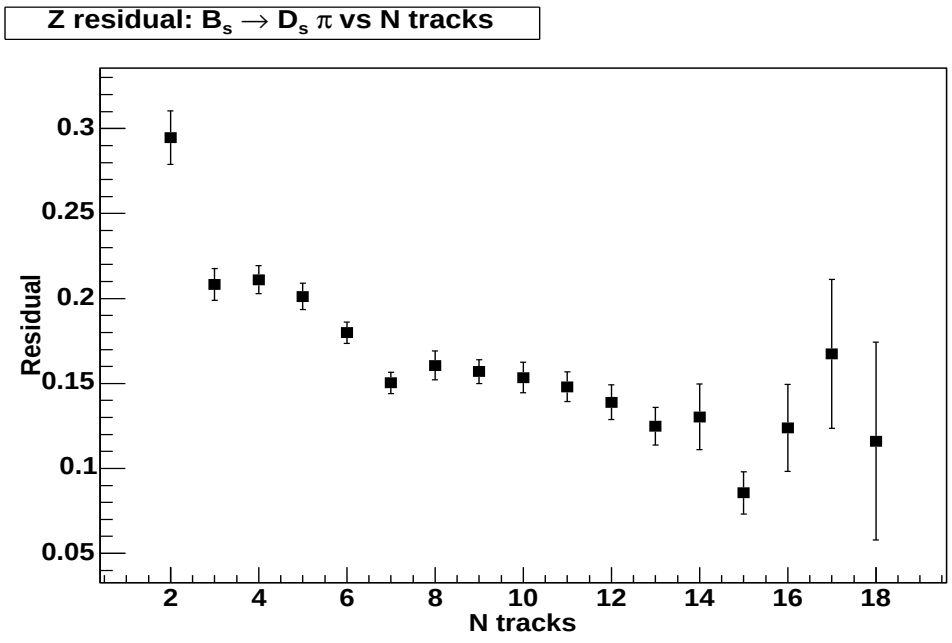

Figure 3.13: z residual (cm) as a function of number of associated tracks to the vertex for the $B_s \to D_s\pi$ MC sample with $p_T > 1$ GeV.

Sample	$\bar{\sigma} = \frac{C_1\sigma_1 + C_2\sigma_2}{C_1 + C_2}$ (cm)	N tracks
$B_s \to D_s\pi$	0.16	6.6
$t\bar{t} \to$ jets	0.12	27.3
$H \to bbbb$	0.15	17.5
$Z^0 \to \mu\mu$	0.17	4.2
$W \to \mu\nu$	0.19	3.4

Table 3.1: Gaussian fit values of the z vertex residuals and the number of associated tracks for the five MC samples.

Different topologies display different resolutions due to the track multiplicity of the events. The effect of track multiplicity can be seen as the residual increases across the different types of event as the multiplicity decreases. This is further illustrated by Figure 3.13 which shows the residual as a function of number of tracks for the $B_s \to D_s\pi$ MC sample. The residual clearly improves with the number of tracks associated.

The performance of the z finding algorithm as a function of track p_T cut is measured in terms of efficiency and purity. A vertex is "correctly found" if the residual is less than 1 cm.

$$\text{efficiency} = \frac{\text{number of correctly found vertices}}{\text{total number of events}} \tag{3.21}$$

$$\text{purity} = \frac{\text{number of correctly found vertices}}{\text{total number of returned vertices}} \tag{3.22}$$

An additional cut was placed on the MC; the primary vertex must have associated with it at least one track with $p_T > 0.5$ GeV and in the CFT fiducial region ($\eta < 1.6$). In the $Z^0 \to \mu\mu$ and $W \to \mu\nu$ MC, this track must also be a muon.

Figures 3.14 and 3.15 show the efficiency and purity as a function of track p_T cut for the five different types of MC event. Both efficiency and purity are high ($>$ 97%) for all topologies at low p_T cuts. Two important effects occur as the p_T cut is increased. As tracks are excluded from the vertex calculation, the track multiplicity decreases, the resolution worsens and the algorithm may give an incorrect vertex.

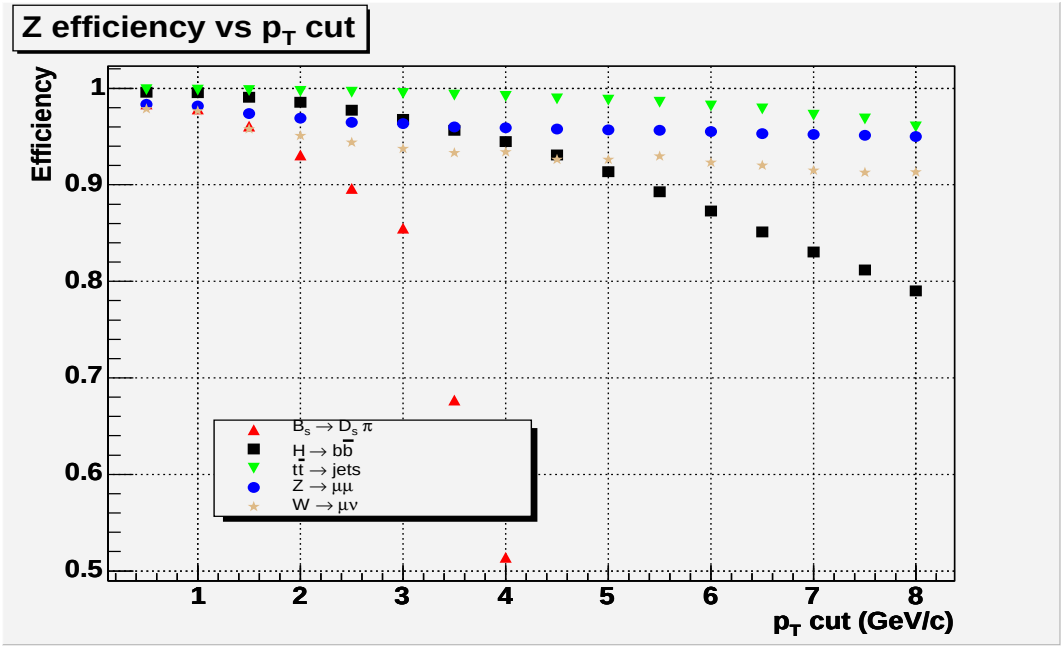

Figure 3.14: z finding efficiency as a function of track p_T cut.

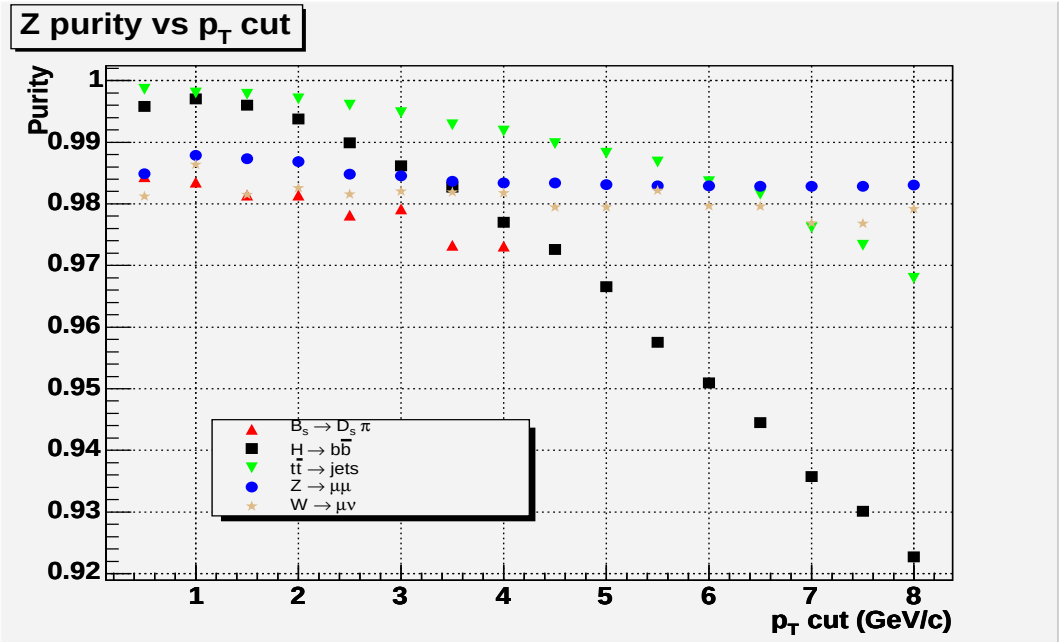

Figure 3.15: z finding purity as a function of track p_T cut.

In addition, if all the tracks in the event are excluded by a particular p_T cut, the algorithm returns no vertex.

The $H \to b\bar{b}b\bar{b}$ and $t\bar{t} \to jets$ events are susceptible mainly to the first effect as they have high track multiplicities (17.5, 27.3) and high p_T spectra. Table 3.2 shows the average p_T, $\langle p_T \rangle$, of the tracks in the samples and minimum bias events. This causes the efficiency and purity to steadily fall with p_T cut with the effect stronger in the $H \to b\bar{b}b\bar{b}$ events due to the lower track multiplicity and p_T spectrum.

Sample	$\langle p_T \rangle$ (GeV/c)
$B_s \to D_s\pi$	1.4
$t\bar{t} \to$ jets	3.7
$H \to bbbb$	2.7
$Z^0 \to \mu\mu$	4.1
$W \to \mu\nu$	2.8
min bias	0.4

Table 3.2: $< p_T >$ of tracks in the five MC samples and minimum bias events.

The $B_s \to D_s\pi$ events have a low track multiplicity (6.6) and a soft p_T spectrum. This makes them susceptible to both effects. The efficiency drops steadily with p_T cut and then falls sharply after around 3 GeV due to there being no tracks available for vertexing. This is the dominant effect since the purity falls only slightly with p_T cut.

The $W \to \mu\nu$ and $Z^0 \to \mu\mu$ events have high p_T leptons which are not excluded at these low p_T cuts. The efficiency and purity remain approximately constant at all p_T cuts. The purities are not 100% due to the "found" window size and misreconstructed tracks.

Most topologies show a decrease in purity between p_T cuts of 1.0 and 0.5 GeV/c. This is due to tracks from minimum bias vertices causing an incorrect vertex to be returned. This effect is small after a p_T cut of > 1.0 GeV. The fact that purity is generally high shows that the algorithm preferentially returns no vertex to returning an incorrect vertex. This is important for tools that will use the vertex, as an incorrect vertex could cause a bias.

3.7.3 x-y performance

There are three main parameters that directly affect the 3-D vertex performance. These are the z vertex p_T cut, the x-y vertex p_T cut and the x-y vertex $\Delta\chi^2$ cut. The first of these parameters has already been investigated in Section 3.7.2 and was kept constant at 1.0 GeV/c in all of the following.

Figure 3.16 shows the x residual as a function of p_T cut while keeping the Δ_{max} constant at 0.2 and 3.17 shows the x residual as a function of Δ_{max} while keeping the p_T cut constant at 0.5 GeV/c.

The optimal performance for both MC samples is found to be when the p_T cut is 0.4 GeV (which is the lowest p_T of the tracker). This is due to the increased number of tracks at lower p_T. The optimal Δ_{max} is 0.1. A larger cut does not reject the incorrect tracks which cause poorer resolution. Conversely, a tighter window rejects too many tracks. These parameters are the values used throughout the rest of the study and are the values currently used online.[3]

Figures 3.18 to 3.19 show the x residual and number of tracks associated to the vertex for the $B_s \to D_s\pi$ and $H \to b\bar{b}b\bar{b}$ MC samples. The residual for both samples is around 30 μm and there are on average 6.9 and 13.4 associated tracks with the $B_s \to D_s\pi$ and $H \to b\bar{b}b\bar{b}$ samples respectively. The B_s sample has $\sim$13.6% events where the beamspot position is returned compared to $\sim$7.7% for the $H \to b\bar{b}b\bar{b}$ case. This is due to the higher track multiplicity in the latter case.

Figures 3.20 and 3.21 show the residual as a function of the number of associated tracks. Both samples show a resolution that is better than the beamspot (30 μm) for all numbers of associated tracks. The vertex in the $B_s \to D_s\pi$ sample shows a better resolution than the $H \to b\bar{b}b\bar{b}$ sample for a given number of tracks. This is because the $H \to b\bar{b}b\bar{b}$ events contain four b quarks and a higher proportion of secondary vertices. When tracks from these vertices are included in the primary vertex calculation the resolution is worsened.

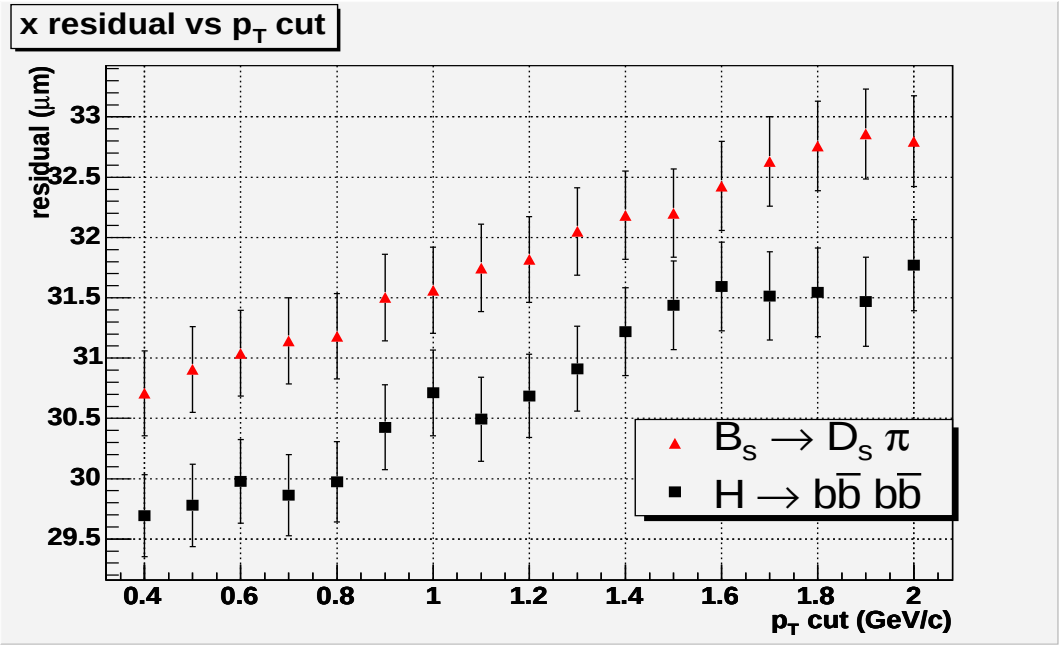

Figure 3.16: x residual as a function of track p_T cut (Δ_{max} cut constant).

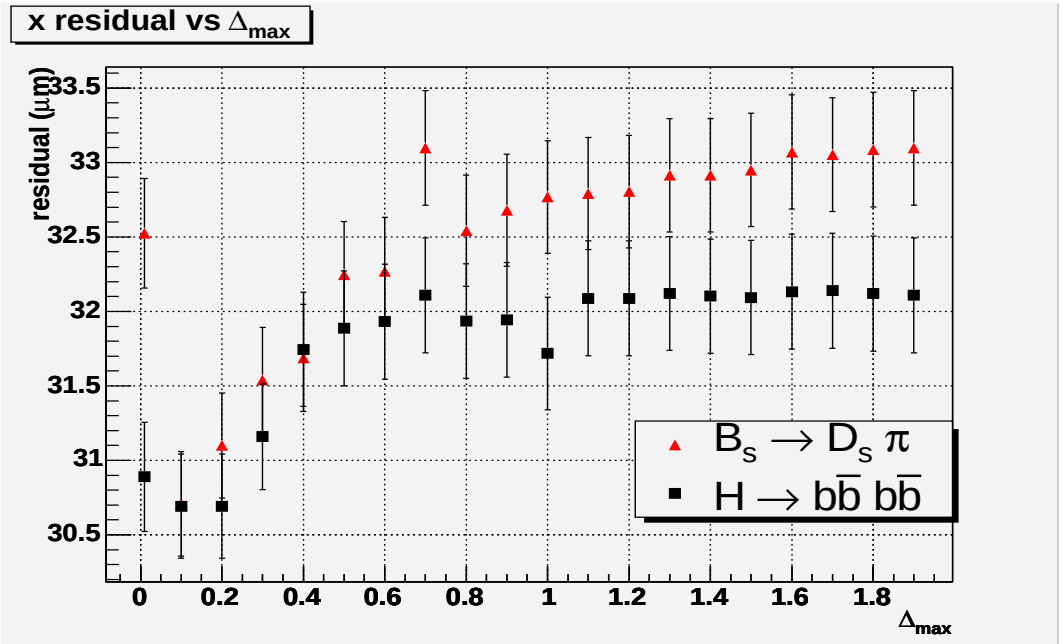

Figure 3.17: x residual as a function of track Δ_{max} cut (p_T cut constant).

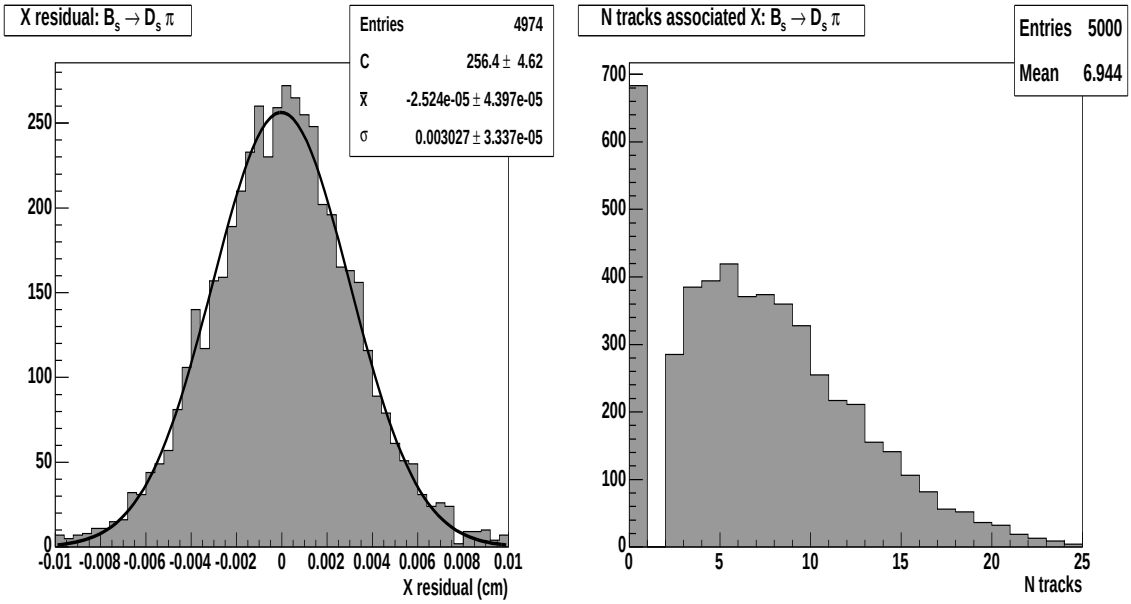

Figure 3.18: $B_s \to D_s \pi$ x residual and number of associated tracks.

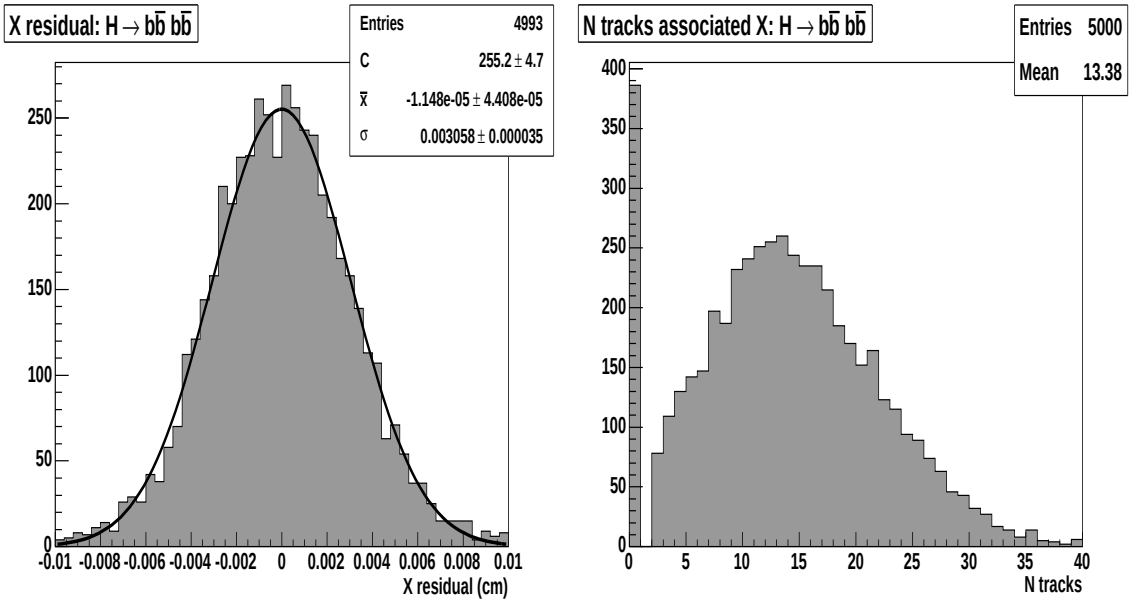

Figure 3.19: $H \to b\bar{b}b\bar{b}$ x residual and number of associated tracks.

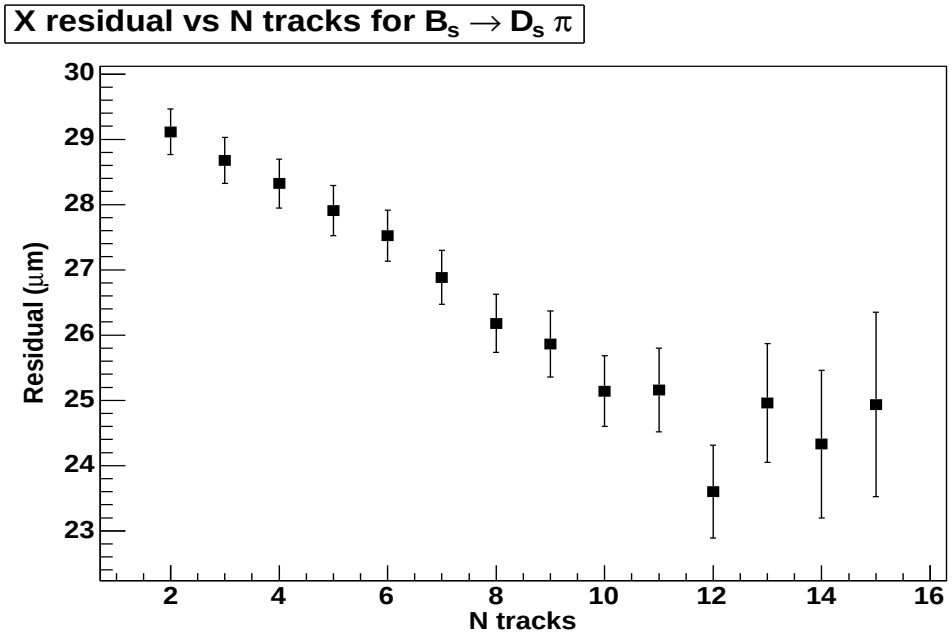

Figure 3.20: $B_s \to D_s\pi$ x residual as a function of number of associated tracks.

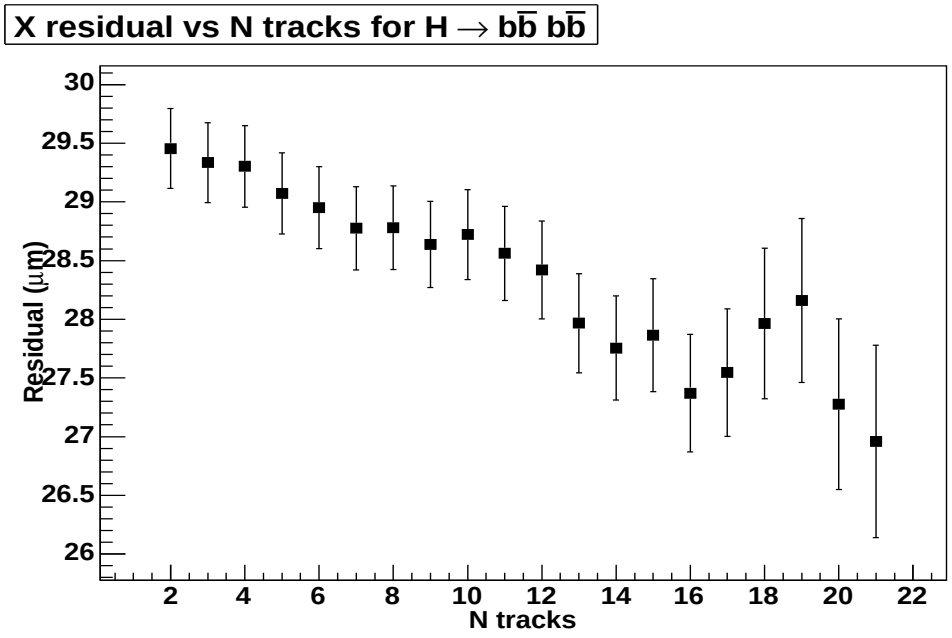

Figure 3.21: $H \to b\bar{b}b\bar{b}$ x residual as a function of number of associated tracks.

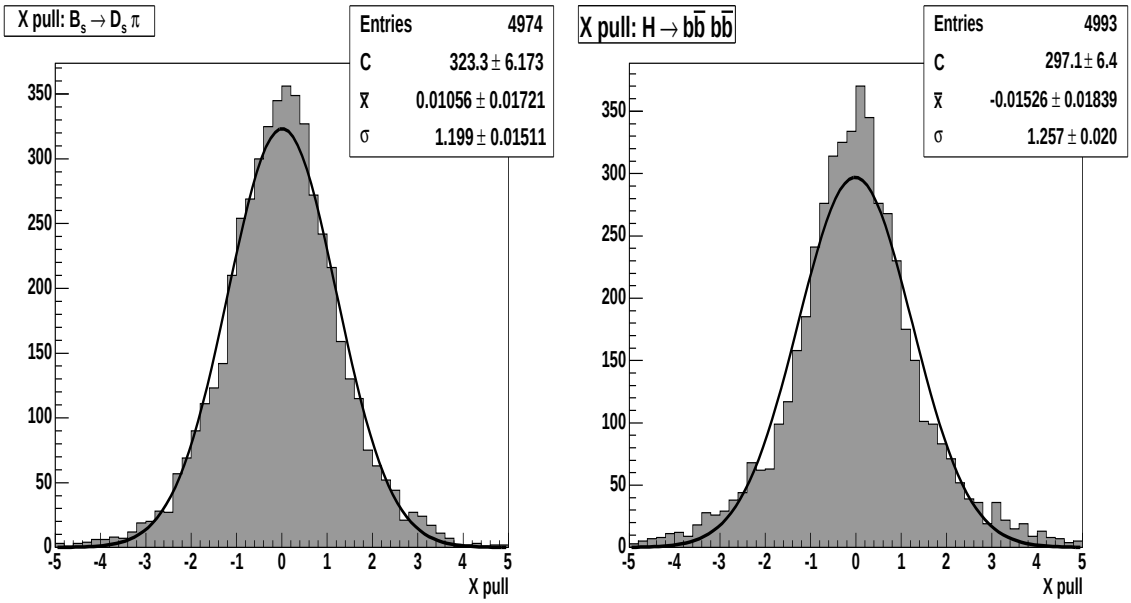

Figure 3.22: Pull distributions for the $B_s \to D_s\pi$ and $H \to b\bar{b}b\bar{b}$ MC samples.

Figure 3.22 shows the vertex pull for all tracks for both samples. Pull is defined as the ratio of the residual to the error. If the error is calculated correctly the pull should be distributed normally with mean zero and standard deviation 1. The distributions are fitted with Gaussians, centred at zero and with widths of 1.20 and 1.23 for the $B_s \to D_s\pi$ and $H \to b\bar{b}b\bar{b}$ samples respectively.

Figures 3.23 and 3.24 show the vertex pull as a function of the number of associated tracks. Both plots are fitted with a first order polynomial and have slopes consistent with zero which suggests that the pull is independent of the number of associated tracks.

The pull values from the Gaussian fits to all tracks (Figure 3.22) give widths larger than unity. The constants in the linear fits to Figures 3.23 and 3.24 are closer to unity (1.10 and 1.08 repectively) but still suggest that the error is underestimated. Since the pull is independent of track multiplicity this will just increase the impact parameter significance of all tracks by a constant amount. Triggers using impact parameter significance will just have less rejection for a given cut value.

[3]In fact a p_T cut of 0.5 GeV/c is now used online for timing reasons.

Figures 3.25 and 3.26 show the width of the vertex distribution (σ_x) as a function of the number of associated tracks. The MC vertex has a Gaussian distribution with $\sigma = 30\mu$m. This demonstrates the effect of the beamspot entering the vertex calculation. For low multiplicity vertices, the beamspot dominates and the vertex position is weighted towards the beamspot position. As the number of tracks associated increases, the beamspot weight becomes less dominant, until the actual beam width is reached as in the $H \to b\bar{b}b\bar{b}$ case.

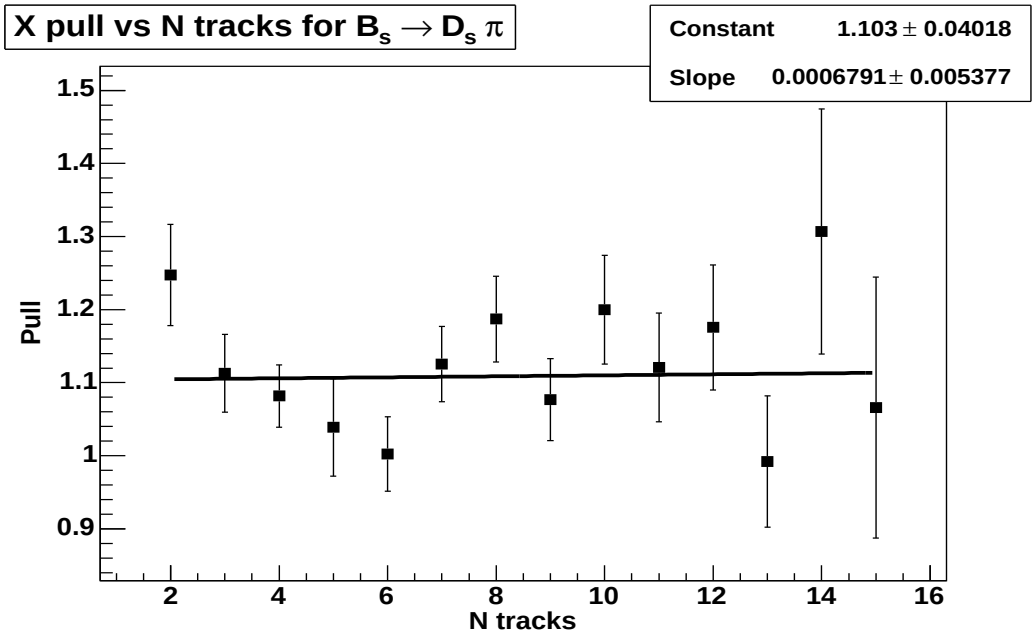

Figure 3.23: $B_s \to D_s\pi$ pull as a function of number of associated tracks.

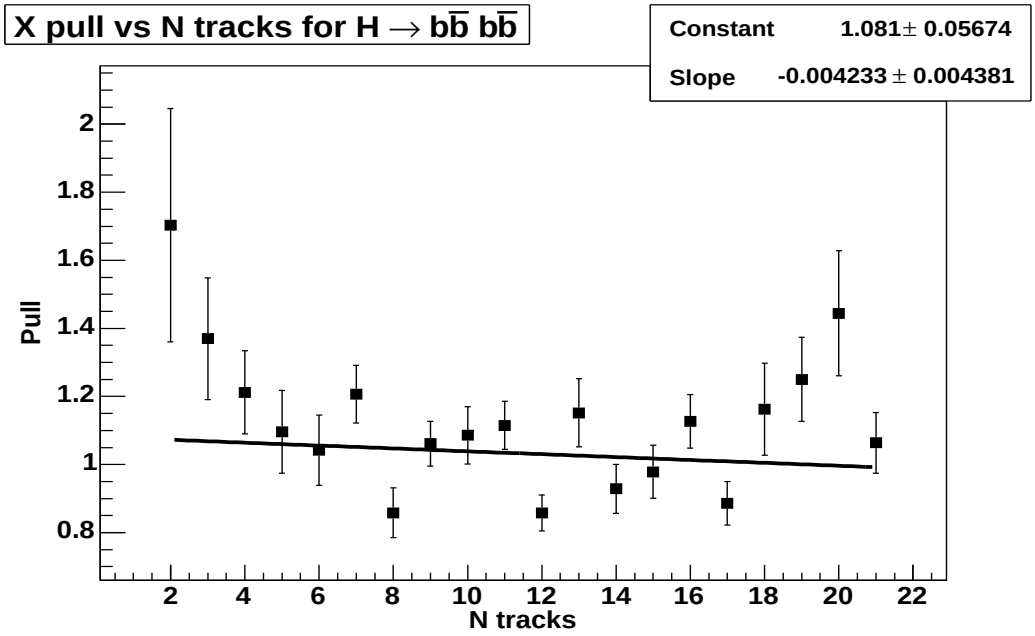

Figure 3.24: $H \to b\bar{b}b\bar{b}$ pull as a function of number of associated tracks.

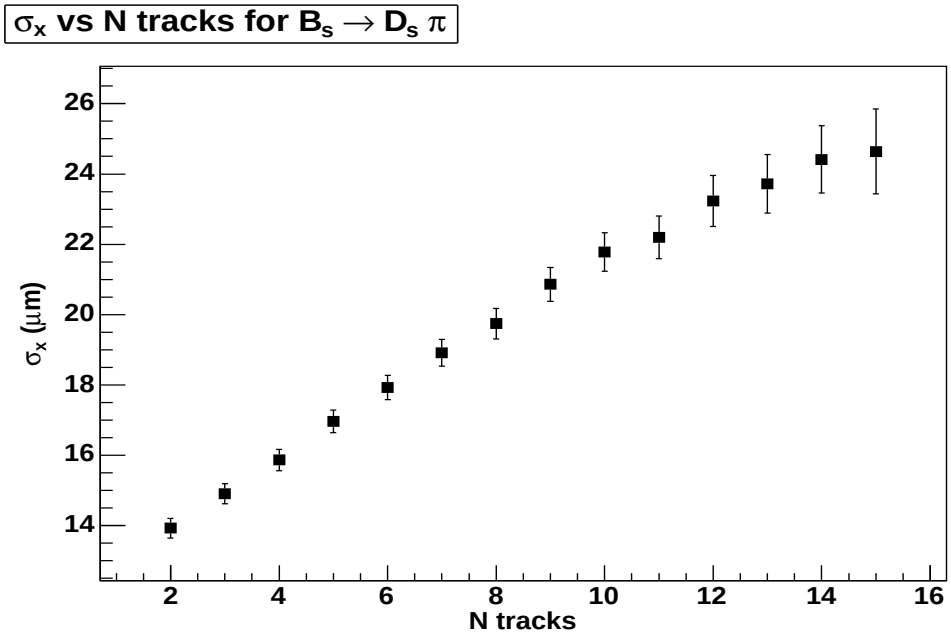

Figure 3.25: $B_s \to D_s\pi$ σ_x as a function of number of associated tracks.

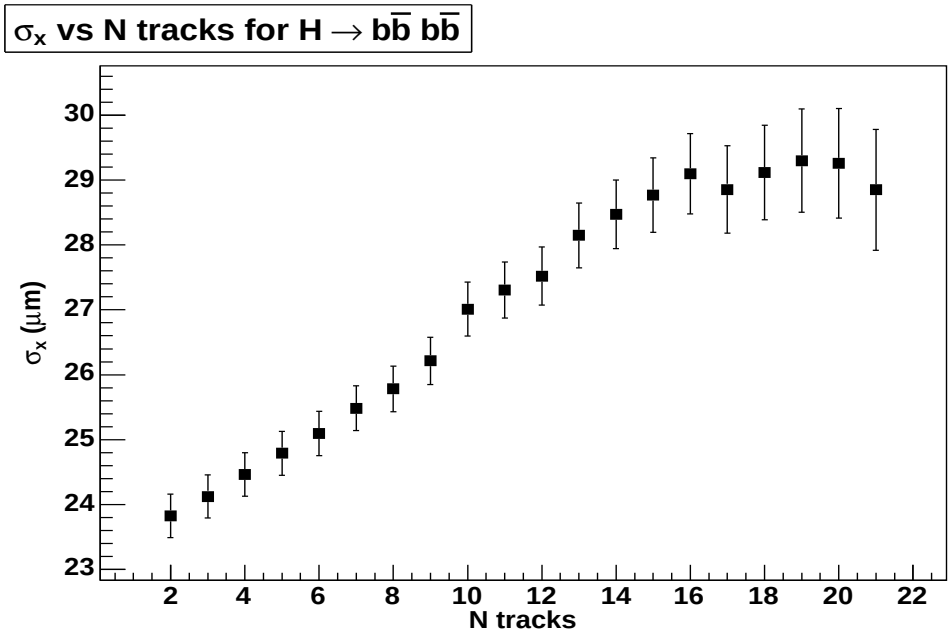

Figure 3.26: $H \to b\bar{b}b\bar{b}$ σ_x as a function of number of associated tracks.

3.8 Data

Figures 3.27 to 3.29 show the vertex distributions for a typical run, 188676. There were no event or trigger selections. Figure 3.27 shows the z distribution and the number of tracks associated to the z and x-y vertex.

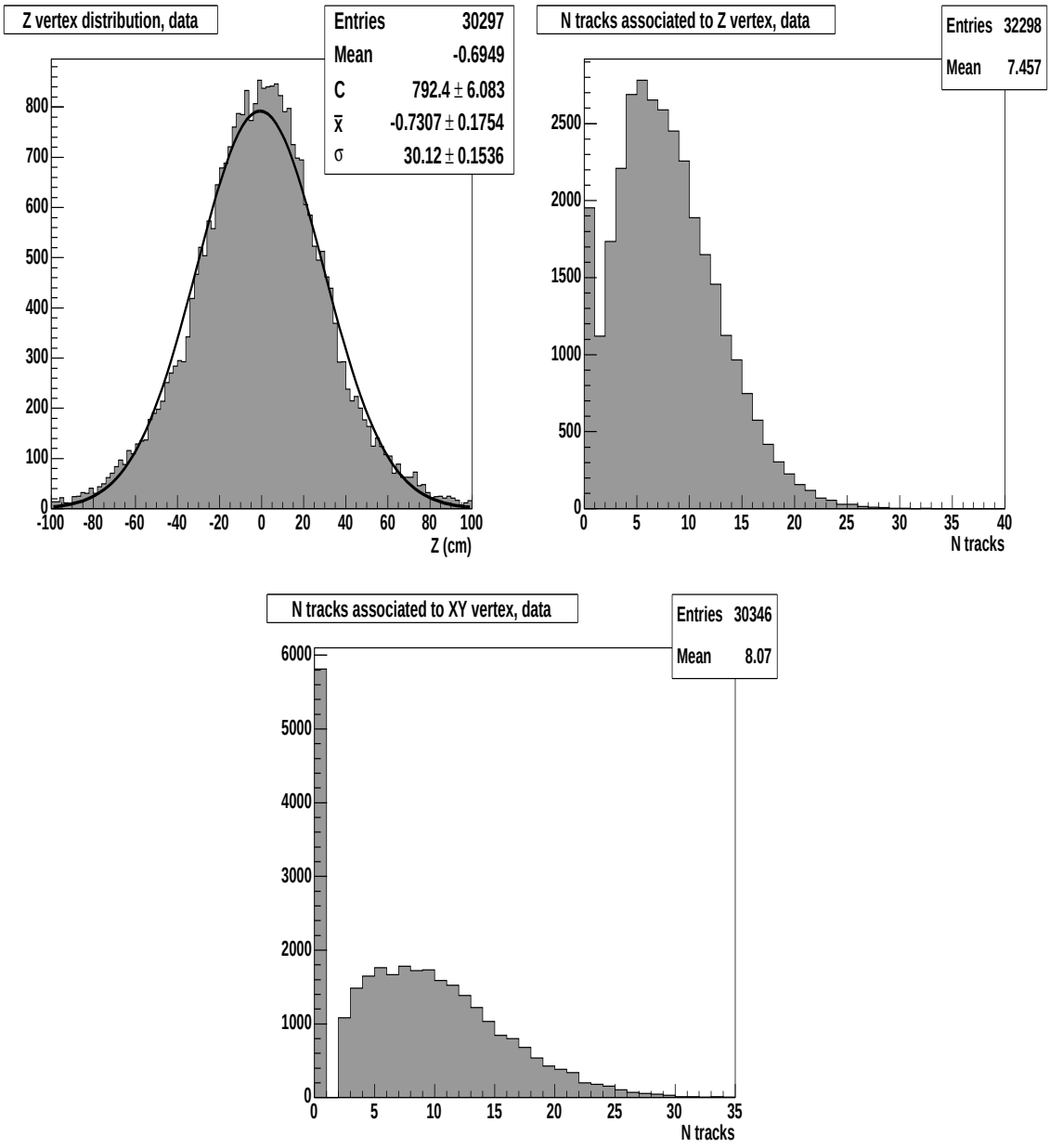

Figure 3.27: z distribution and number of tracks associated to the z and x-y vertex, run 188676

The mean number of tracks associated to the z vertex is 7.5 and the efficiency for

returning a z vertex is around 94%. The vertex distribution is Gaussian with a width of 30cm, as expected. The mean number of tracks associated to the x-y vertex is 8.1 and the efficiency for finding a (non beam spot) x-y vertex, given a z vertex is $\sim$ 81%.

Figures 3.28 and 3.29 show the x and y vertex position as a function of z position (xz and yz tilt). The plots show how the vertex position is distributed around the beam line up to $|z| < 40$cm. Beyond this distance, tracks no longer pass through the full CFT fiducial region and the mean beamspot position is returned.

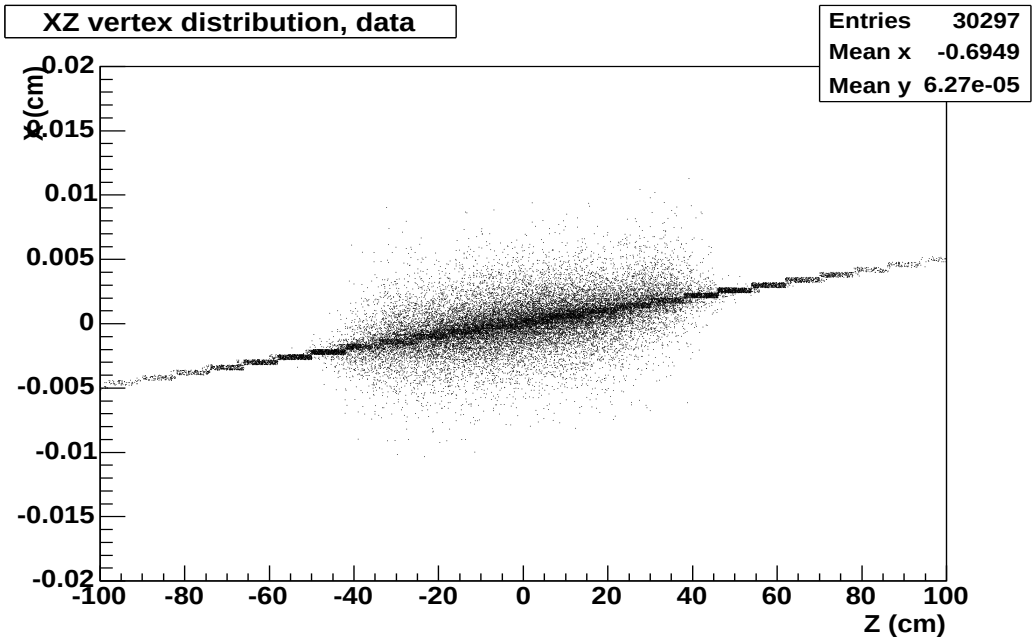

Figure 3.28: x vertex position as a function of z.

Figure 3.30 shows the track d_0 resolution as a function of p_{scat}. The asymptotic resolution is 15.3μm. This depends on detector intrinsic resolutions, detector alignment and the primary vertexing resolution. This value is competitive with the offline `d0reco`[4] vertex (see Section 3.9).

[4] `d0reco` is the offline DØ event reconstruction software

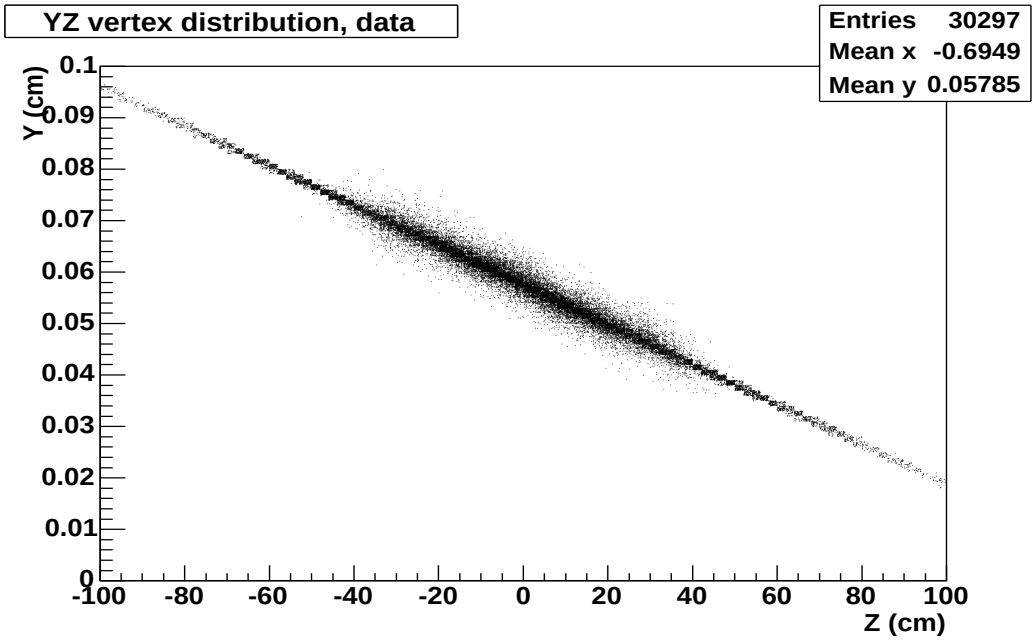

Figure 3.29: y vertex position as a function of z.

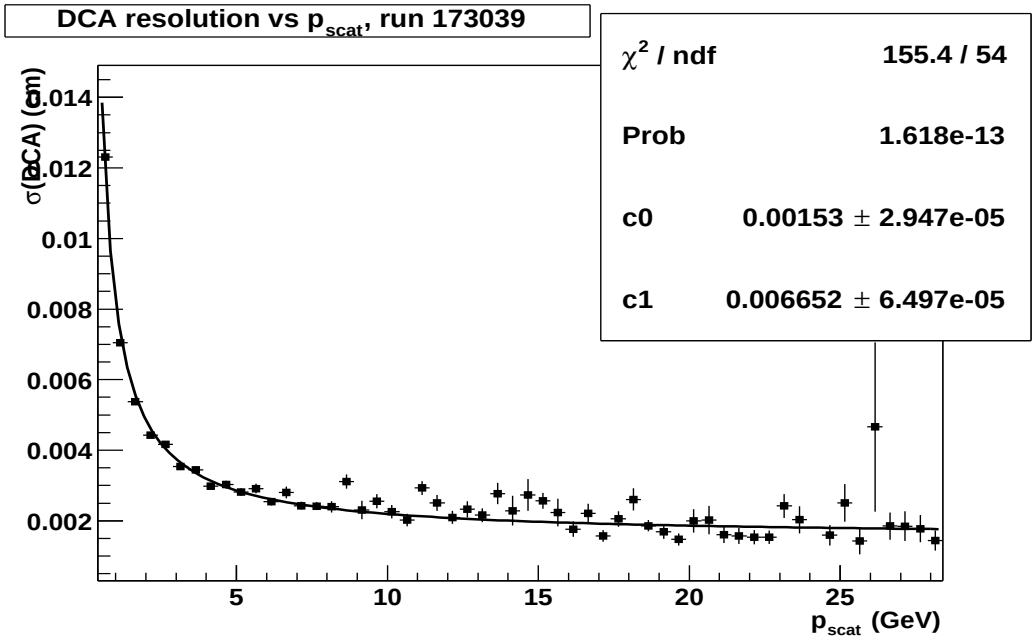

Figure 3.30: Track impact parameter resolution as a function of p_{scat}.

3.9 d0reco comparisons

d0reco is the main offline reconstruction software at DØ. The vertexing uses a 2-pass algorithm described in reference [42]. This section compares the performance of the offline and online vertexing tools. Figure 3.31 shows the residual between the d0reco primary vertex and the Level-3 primary vertex for the $B_s \to D_s\pi$ MC sample. The width of the residuals is $\sim 44\mu$m in x and y and 1.9 mm in z.

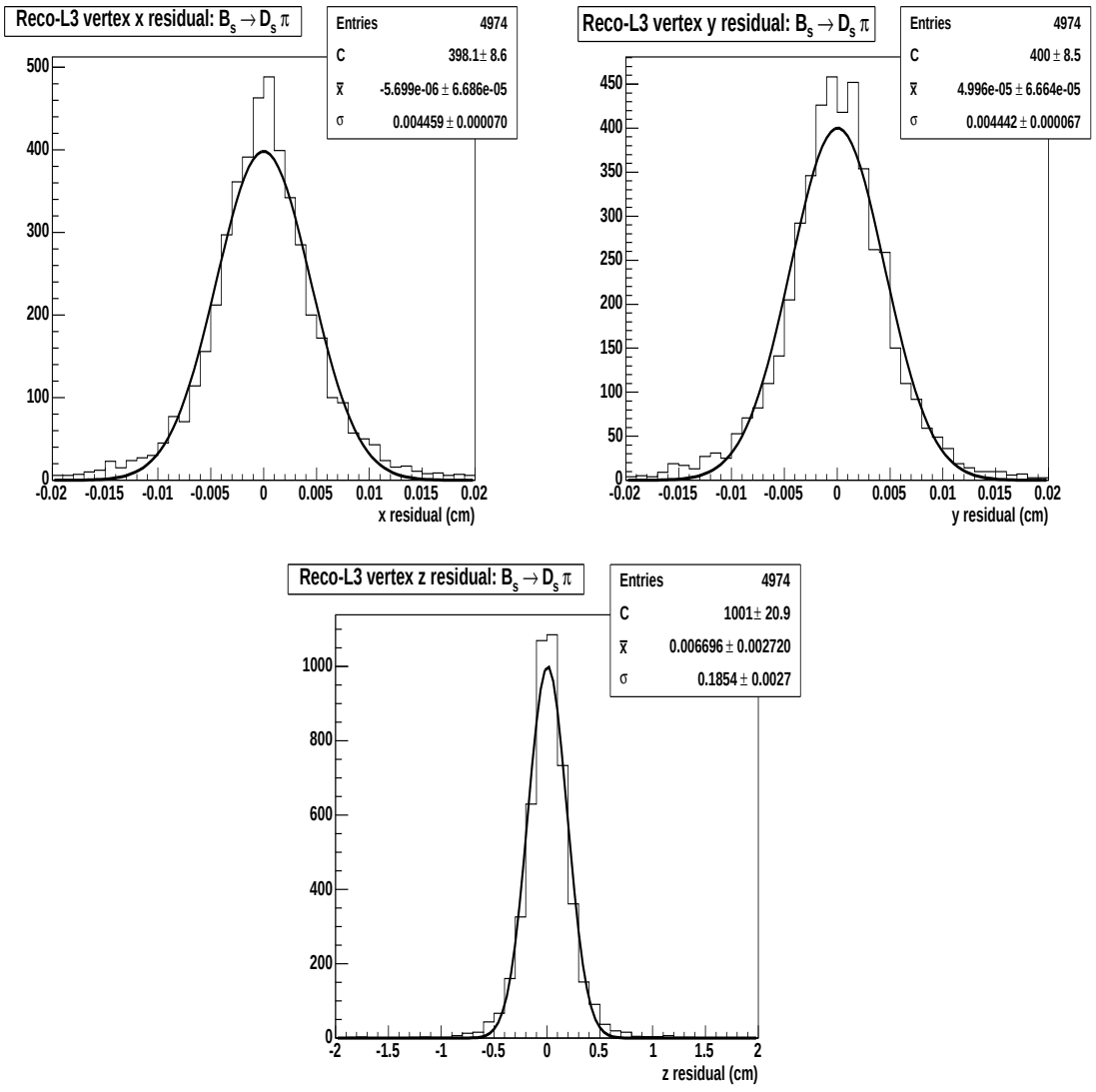

Figure 3.31: Residual between Level-3 and d0reco vertices, $B_s \to D_s\pi$ MC.

Figure 3.32 shows the distributions of the parameter A, defined as

$$A_i = |L3PV_i - MCPV_i| - |\texttt{d0reco}PV_i - MCPV_i| \tag{3.23}$$

where $L3PV$, $MCPV$ and $\texttt{d0reco}PV$ are the Level-3, Monte Carlo truth and d0reco primary vertices respectively. The subscript i refers to the x,y and z co-ordinates.

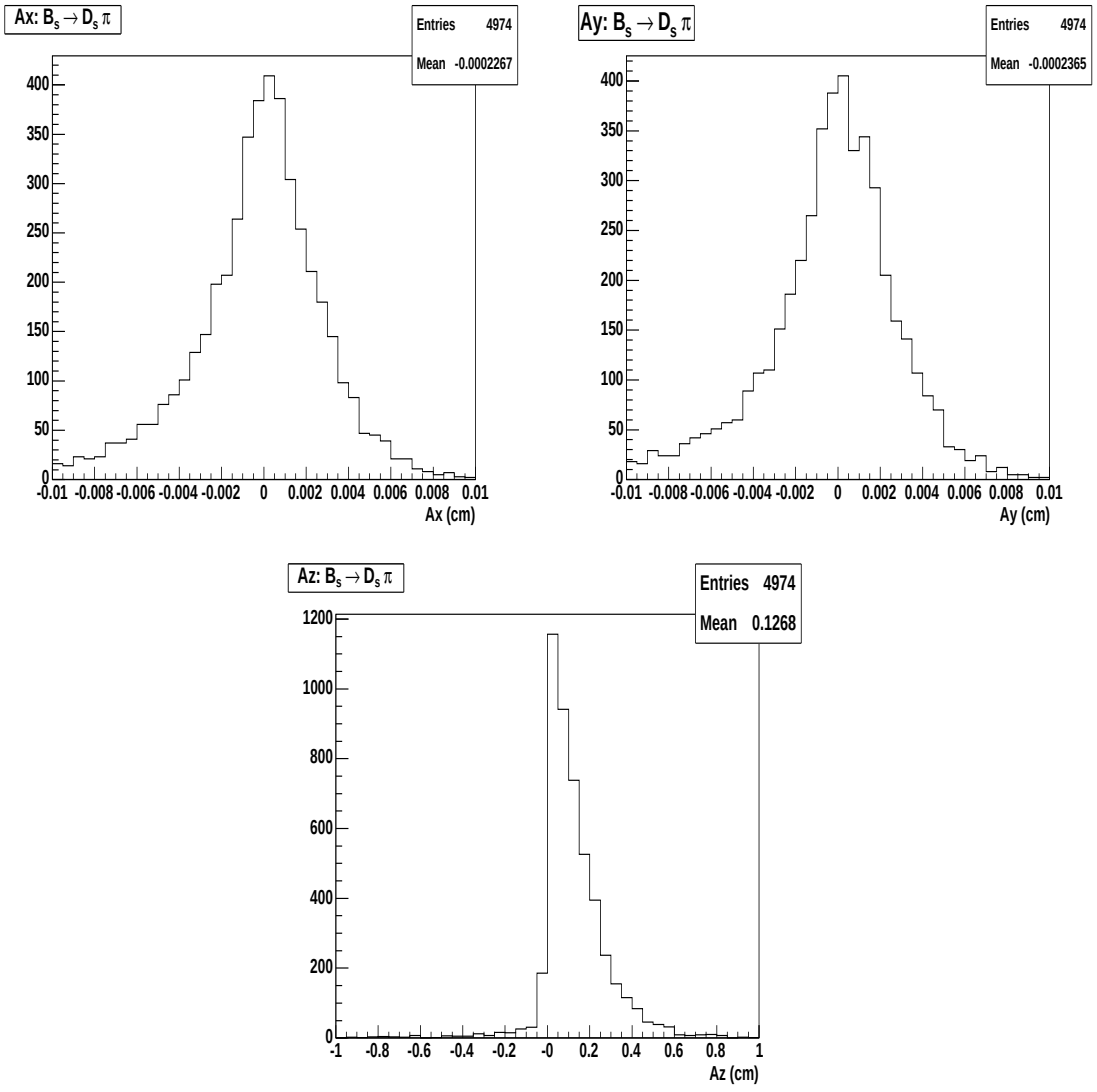

Figure 3.32: A_i distributions for Level-3 and d0reco vertices, $B_s \to D_s\pi$ MC.

Any performance difference in the vertexing algorithms is represented by a non zero mean. Positive mean represents better d0reco performance and vice versa. The A_x

and A_y distributions show a mean close to zero and negative, which suggests the Level-3 vertex is outperforming the the d0reco vertex. A significant achievement in the limited time available at Level-3. The A_z distribution has a positive mean. In this case the d0reco vertex does better than the Level-3 vertex. This is expected, due to the more sophisticated 3-D vertexing algorithm. The Level-3 primary vertex z coordinate does not require greater accuracy as the tools that use it, such as the Level-3 jets, require accuracy on the order of centimetres for trigger purposes. In addition, these tools may already be time consuming and require a very fast z primary vertex (see Section 3.10).

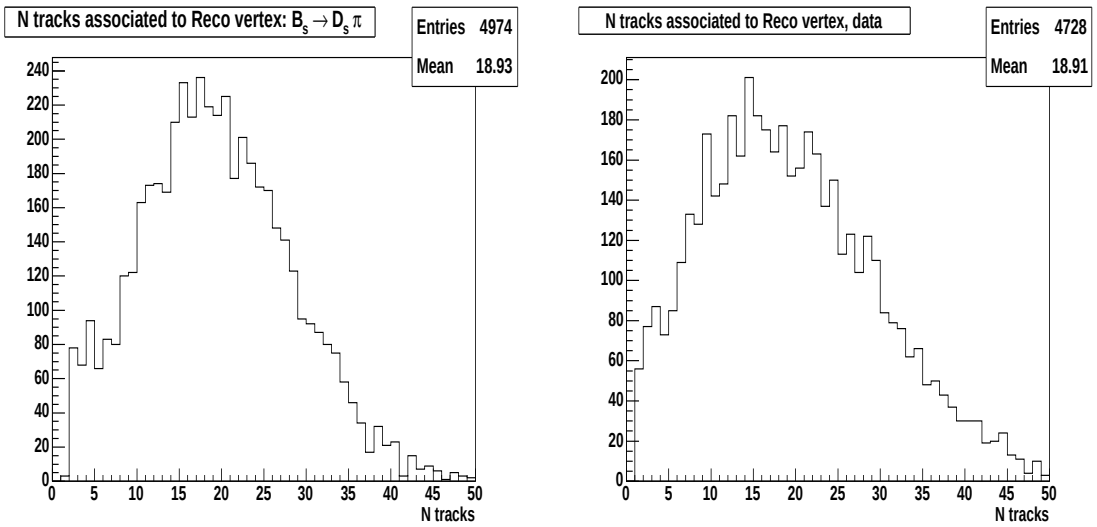

Figure 3.33: Number of tracks associated to the d0reco vertex for the $B_s \to D_s\pi$ MC and data run 188676.

Figure 3.33 shows the number of tracks associated to the d0reco vertex for the $B_s \to D_s\pi$ MC sample and data. There are ~19 associated tracks on average for both samples. The corresponding numbers for the Level-3 x-y primary vertex are 7 and 8 respectively. The fact the equal resolutions are achieved is particularly impressive.

Figure 3.34 shows the residual between the Level-3 vertex and the d0reco vertex for data. The width of the x and y distributions is similar to the corresponding MC plots. However, the width of the z distribution is $\sim$ 3mm which is larger than the

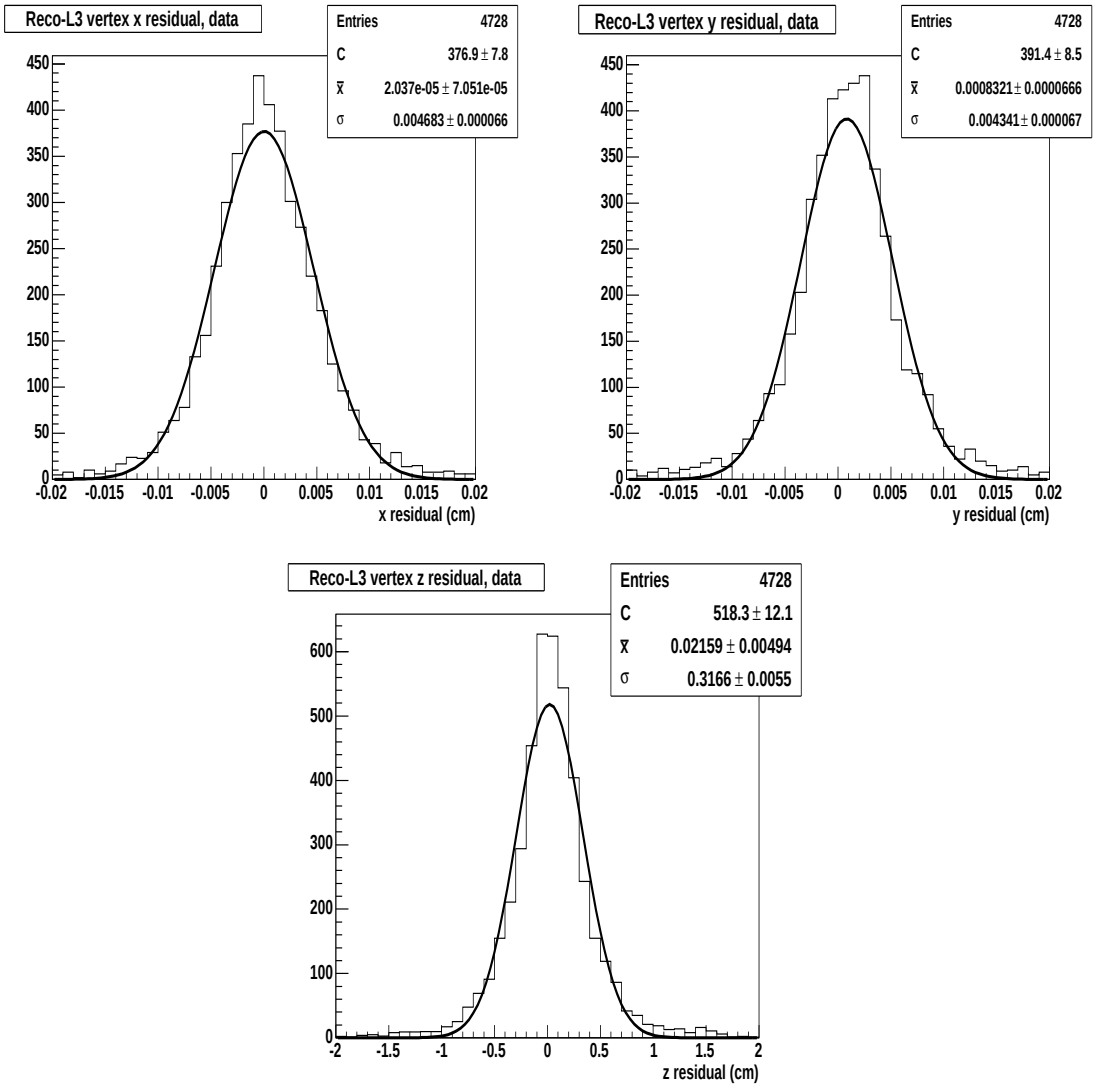

Figure 3.34: Residual between Level-3 and `d0reco` vertices, data run 188676.

corresponding MC plot. This is due to the weaker performance of the histogramming technique, due to the larger number of fake tracks in data.

3.10 Timing

As stated earlier, timing is a crucial factor in the design of tools for the Level-3 trigger. Figures 3.35 and 3.36 show the time per event for the SMT and CFT unpacking, global tracking, z vertex finder and x-y vertex finder on data events, run 179760. This chain of tools is required to calculate a 3-D primary vertex.

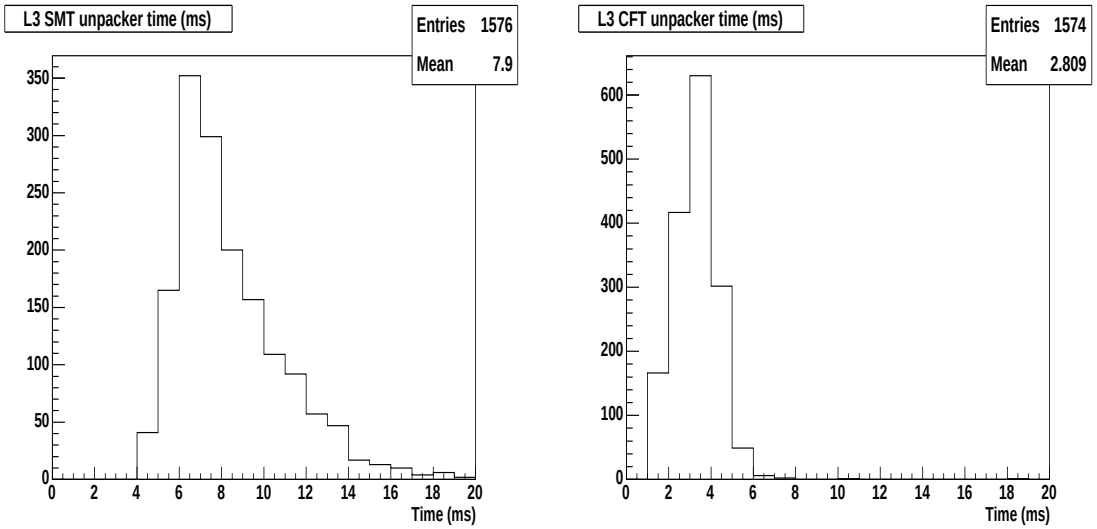

Figure 3.35: Time for Level-3 SMT and CFT unpacking.

Table 3.3 summarises the time per event for each Level-3 tool. Included in the table is the time taken by `d0reco` assuming tracking takes 62% and vertexing takes 5% of the total time per event [43]. All the times are normalised with respect to the speed of the processor the study was performed on. The numbers in the table correspond to a 1GHz processor.

The total vertexing time is around 300μs which is around 3 orders of magnitude faster than the unpacking and tracking. This easily satisfies the online timing constraints.

3.11 Implementation

The packages containing the code for these algorithms are `l3fcft_vertex` and `l3fxy_vertex` for the z and x-y finders respectively. The Level-3 tool names are `L3TCFTVertex` and `L3TXYVertex`. The package `l3fcft_vertex` was originally written by Ray Beuselinck. In its original form a simple average of track Z_0's was performed with a histogramming method used if no tracks passed the selection criteria. I modified the algorithm to use histogramming and then the p_T weighted histogramming by default. This package was developed starting in February of 2002 and was included in the global_CMT-8.00 physics triggerlist which first ran online

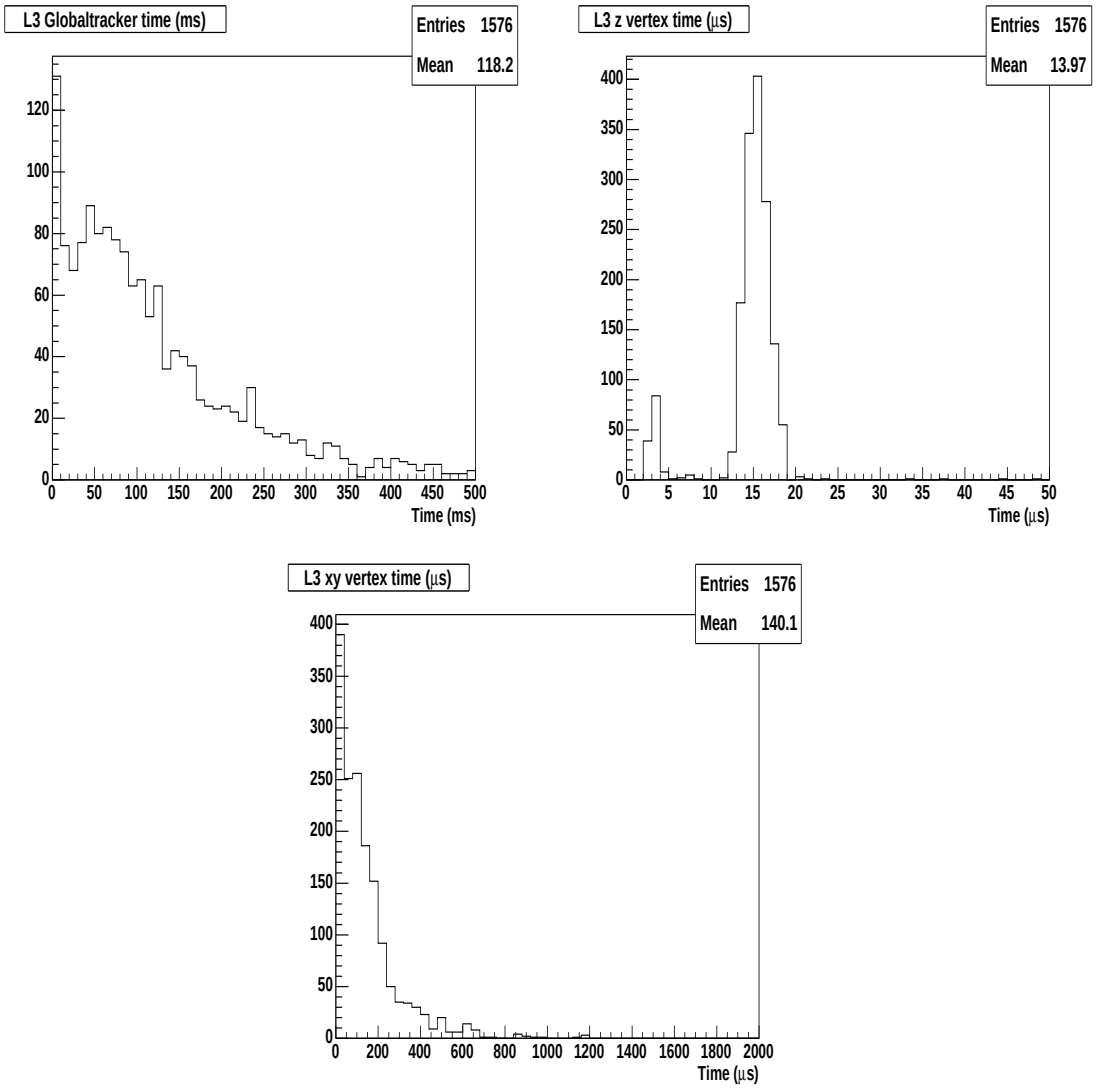

Figure 3.36: Time for Level-3 tracking ($p_T = 0.4$ GeV/c), z vertex ($p_T = 1.0$ GeV/c) and x-y vertex ($p_T = 0.4$ GeV/c).

	Level-3	`d0reco`
SMT unpacking	15.8 ms	12.8 s
CFT unpacking	5.6 ms	
Tracking	236.4 ms	
z vertex	27.9 μs	1.03 s
xy vertex	280.2 μs	

Table 3.3: Timing for the Level-3 tools required for a 3-D primary vertex. Included are the equivalent `d0reco` times. All times are normalised to 1GHz seconds

in June of that year. It has been a part of every triggerlist since then and is used in all jet and missing E_T triggers. More recently it is being used to trigger on events occuring in the tracking fiducial region by requiring $|PV_Z| < 35$cm.

I started developing the package `l3fxy_vertex` in September of 2002. It was first included in a physics triggerlist in version global_CMT-12.00 in April of 2003. The impact parameter tool, `L3TIPTracker`, (which I also solely developed and is described in Chapter 4) and the B-Jet tagger, `L3TBTagIP` use the 3-D vertex as a foundation.

I have had sole responsibility for all the Level-3 vertexing algorithms at DØ since the spring of 2002. This has involved extensive testing, maintenence and code improvements. In addition, every new software release that has been used on the Level-3 farms has required performance evaluation, timing checks and re-certification. The Level-3 vertex tools described in this chapter are currently the only tools of their kind used by the DØ collaboration.

Chapter 4

Level-3 Triggers for B Physics

4.1 Introduction

The rich B physics programme at DØ utilises the excellent muon coverage to trigger on events containing muons. The Level-1 bandwidth does not allow triggering on tracks by design, therefore all types of B physics events are collected with single and di-muon triggers. Many important decay modes are collected with these triggers. The di-muon trigger, for example, collects J/ψ events used for CP studies of $B_s \to J/\psi\phi$. The single muon trigger is extremely important for B_s mixing, collecting both semileptonic and hadronic modes. In semileptonic modes such as $B_s \to D_s\mu\nu$, the initial B flavour can be tagged using same-side, soft lepton or opposite side jet charge tagging [2]. Hadronic modes, such as $B_s \to D_s\pi$ collected with the single muon trigger, already have the initial B flavour tagged by assuming that the triggered muon is from the opposite-side b decay. Effective use of the single muon trigger will be key to DØ's prospects for measuring B_s mixing.

4.2 B physics at hadron colliders

The $b\bar{b}$ production cross section at a hadron collider is large. Table 4.1 compares current and past experiments. The production cross section at the Tevatron is around five orders of magnitude greater than at the B factories.

Experiment	Process	$\sqrt{s}$	σ
Tevatron	$p\bar{p} \to b\bar{b}$	1.96TeV	150μb
LEP, SLC	$e^+e^- \to b\bar{b}$	Z^0	7nb
PEP-II, KEK	$e^+e^- \to B\bar{B}$	$\Upsilon(4s)$	1nb

Table 4.1: Comparison of B production cross sections at different experimental facilities.

In addition, all B hadron species are produced including B_s, B_c and Λ_b which is not true of the B factories. However, at a hadron collider, the inelastic cross section is 3 orders of magnitude larger than the $b\bar{b}$ cross section, with a p_T spectrum which is approximately the same. Figure 4.1 (left) compares the p_T spectrum of B_d decay products and minimum bias events in MC. In addition, events have high track multiplicities, an example of which is shown in Figure 4.1 (right). These factors make effective triggering and offline analyses extremely challenging.

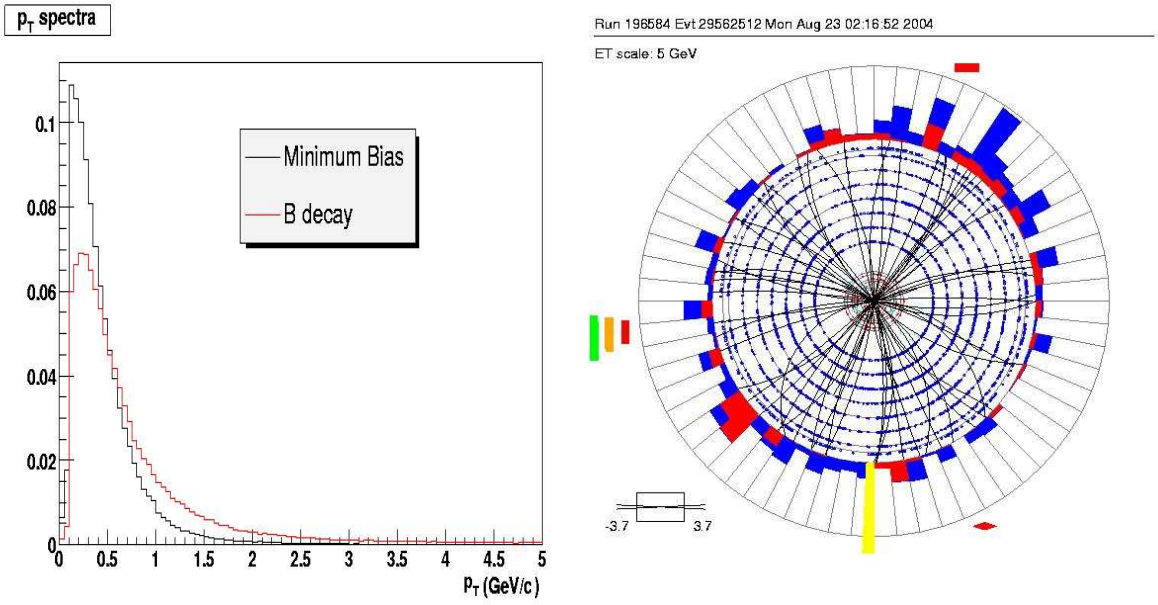

Figure 4.1: A comparison of B_d decay and minimum bias p_T spectra in MC (left). An x-y event display of a typical bunch crossing for run 196584 (right). The instantaneous luminosity for this run was ~30x10^{30}cm^{-2}s^{-1}. The inner concentric circles represent, to scale, the SMT and CFT detectors and the reconstructed tracks within them. The outer concentric ring is a histogram of deposited energies within the $|\eta| < 3.7$ range with red, blue and yellow representing the electromagnetic, hadronic and missing energies respectively. Outside of this ring are coloured bars and diamonds which represent hits in the muon system.

Level-1 LOOSE	A & BC[a] muon in wide[b] region tight scintillator and loose wire requirements 3 GeV CTT track **OR**
TIGHT	muon in wide region loose scintillator and loose wire requirements 5 GeV CTT track matched to A-BC scintillator pair
Level-2 LOOSE	muon with 2 wire hits in A and BC layers associated scintillator hits **OR**
TIGHT	muon with 2 wire hits in A and BC layers associated scintillator hits scintillator timing window < 10 ns
Level-3	muon with 2 wire hits or 1 scintillator hit in A layers 2 wire hits and 1 scintillator hit in BC layers Central track match with p_T cut

Table 4.2: Level-1, Level-2 and Level-3 single muon trigger requirements.

[a]BC requirement is a hit in either layer B or layer C
[b]wide refers to the CFT fiducial region

4.3 Single muon trigger

A detailed description of the DØ muon trigger can be found in references [44], [45], [46]. The Level-1, Level-2 and minimum Level-3 requirements for all current single muon triggers are summarised in Table 4.2.

The acceptable rate for this trigger is 2-3 Hz averaged over all luminosities. The ideal strategy would be to trigger on A-stub muons which are muons passing through only the A scintillator layer, which is inside the iron toroid. Unfortunately the rate at Level-1 is too high for single muons so the additional requirement of a hit in either the B or C layer has to be enforced. Since these layers lie outside the iron toroid the muons have an effective minimum p_T of 3 GeV/c. Therefore, the optimum p_T cut of the central matched muon at Level-3 is 3.0 GeV. However, the unprescaled rate at a luminosity of $30\text{x}10^{30}\text{cm}^{-2}\text{s}^{-1}$ is $\sim$30Hz. Since the maximum total rate for all triggers is 50 Hz, this trigger is effectively turned off at this luminosity. If the

central match p_T cut is increased to 5.0 GeV the corresponding unprescaled rate at 30x10^{30}cm^{-2}s^{-1} is $\sim$11Hz which receives a prescale of "6".

When a trigger is prescaled its decision is only run on a fraction of events. For example, if a trigger has a prescale of 5, it is only applied to 1 in every 5 events. In terms of event yield or integrated luminosity, a trigger that is 20% efficient for signal is *always* preferred to a prescale of 5, since a prescale is applied randomly.

These triggers are allowed bandwidths of up to 10Hz at luminosities less than 20x10^{30}cm^{-2}s^{-1}. However the Tevatron peak instantaneous luminosity is approaching 100x10^{30}cm^{-2}s^{-1} and increasingly, stores are dumped at luminosities around 20x10^{30}cm^{-2}s^{-1}. In order for the single muon triggers to run greater rejection at Level-3 is needed. This is essential for the B physics programme in general and B_s mixing in particular.

Two main properties that distinguish the B physics signal from the continuum are the B lifetime and the invariant mass of the decay products. Because of the B lifetime the tracks from the decay products will be displaced from the primary vertex. Assuming the background is from QCD processes the background tracks should all be compatible with the primary vertex. Level-3 impact parameter significance and invariant mass tools were developed by myself to take advantage of these properties.

4.4 Impact parameter significance at Level-3

To fully exploit the displaced tracks from the B decay products, an impact parameter significance (IPS) tool was developed. This tool was developed by myself, after the vertexing tools described in Chapter 3, had been certified. If a track is associated to the primary vertex and the error description is correct, then the IPS will have a Gaussian distribution with a mean of zero and a standard deviation of 1. Therefore any track that has an $|IPS| > 3$ is excluded from being associated with the primary vertex with $> 99\%$ confidence.

The IPS tool requires that the tracking and full 3-D vertexing has run. As input it takes the 3-D primary vertex and a list of tracks from the global tracker. All tracks must pass the following selection criteria before they are considered suitable for IPS cuts

- $\chi^2 < 5$ for one degree of freedom in both axial and stereo
- $|Z_0 - PV_z| < 2\text{cm}$
- $\sigma_{d_0} < 750\mu\text{m}$
- $d_0 < 5\text{mm}$

The total number of hits and number of SMT hits can be cut on at the filter level. The χ^2, σ_{d_0} and d_0 cuts are general track selection criteria. The Z_0 cut ensures that the track comes from the hard scatter primary vertex and not a minimum bias vertex.

The tracks that pass the selection criteria enter an algorithm that performs a coordinate transformation into the system where the origin is the found primary vertex position (vertex coordinate system). All the track parameters are recalculated. In this system the new d_0 track parameter (denoted by $d_0^{'}$) is the impact parameter by definition (Appendix A). The error in the vertex coordinate system, $\sigma_{d_0}^{'}$, is given by

$$\sigma_{d_0}^{2\,'} = \sigma_{d_0}^2 - \sigma_{V_x}^2 - \sigma_{V_y}^2, \tag{4.1}$$

if the track is included in the set of tracks that form the primary vertex, or

$$\sigma_{d_0}^{2\,'} = \sigma_{d_0}^2 + \sigma_{V_x}^2 + \sigma_{V_y}^2. \tag{4.2}$$

otherwise. The negative sign arises from the fact that a track used in the calculation of the primary vertex has an error correlated with the vertex error. The significance is then given by $d_0^{'}/\sigma_{d_0}^{'}$.

The Level-3 tool that performs this task is named `L3TIPTracker`. It is a physics tool and creates `L3IPTrackPhysicsResults` for each track passing the selection criteria. These objects contain the original track parameters, the recalculated track parameters and the impact parameter and its error. `L3TIPTracker` recalculates all the needed track parameters and creates the list of physics objects in less than 1 ms and poses no timing concerns.

The `L3IPTrackPhysicsResults` objects form a basis for a framework of IPS filters. The first filters using these objects, developed by myself for B physics, are track and muon IPS filters. However, filters to calculate the IPS of electrons, taus, jets or any object with a track associated are easily developed within this framework.

4.5 Track impact parameter significance

As already stated, events containing B mesons will, in general, contain multiple tracks that are displaced from the primary vertex. By requiring multiple tracks with IPS above a threshold, background events can be rejected at the trigger level. The filter `L3FIP` accesses the list of `L3IPTrackPhysicsResults` produced by `L3TIPTracker`. The filter requires at least N tracks satisfying the following cuts

- Minimum p_T
- Minimum IPS
- Maximum IPS
- Total number of axial hits
- Total number of stereo hits
- Number of axial SMT hits
- Number of stereo SMT hits

Figure 4.2 compares the Level-3 IPS of all tracks in $B_s \to D_s\pi$ MC and real data events. As expected, the tracks in the B events have higher IPS than the background events

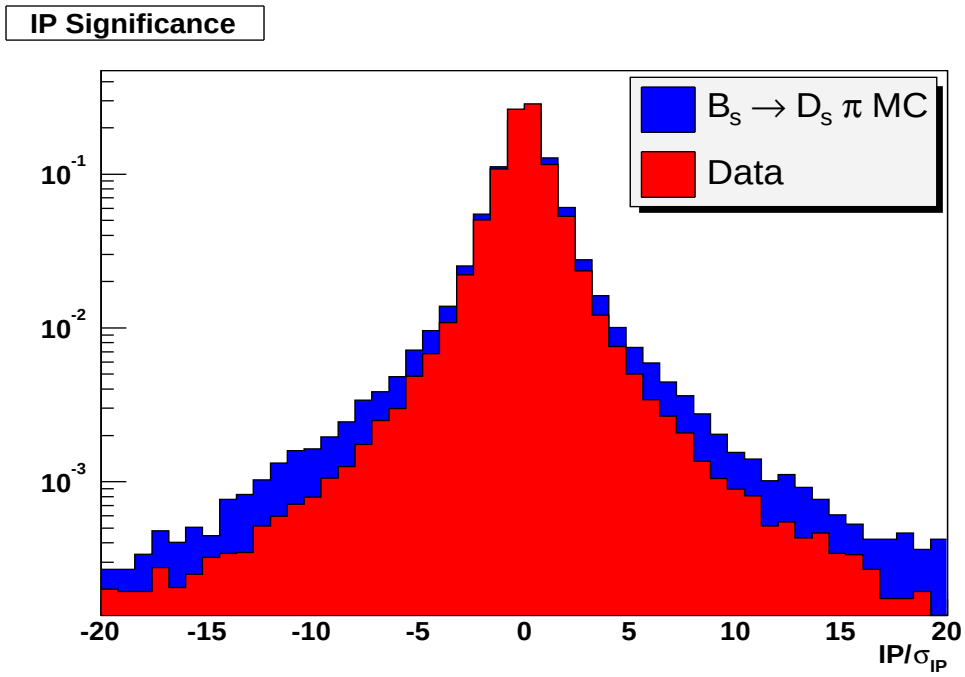

Figure 4.2: Comparison of Level-3 IPS for all tracks in $B_s \to D_s\pi$ MC and data, run 188676.

An important point to note is that if the primary vertex position is incorrect the IPS will in general be increased which means events will pass the triggers rather than get rejected. This will increase the pass rate but is preferred to rejecting good events.

4.6 Muon impact parameter significance

This filter utilises the fact that a muon from a B decay should have a larger IPS than a muon that originates from the primary vertex. Since B physics events are collected at DØ by muon triggers this filter could be applied to all B physics analyses. For hadronic decays the muon would originate from the opposite-side B decay, also

known as the "tagging" muon. For semileptonic decays the muon could originate from the B on both sides.

The filter that performs this task is named `L3FPhysIP` and it is a relational filter. The Level-3 muon tools `L3TMuoCentralMatch` and `L3TMuon` match tracks in the central region with hits in the muon system [45]. They output a list of `L3TMuonPhysicsResults` objects which contain information from the muon system and the central track that has been matched. The muon filter [46] runs and outputs a list of muons passing the specified requirement cuts. `L3FPhysIP` compares this list of muons with the list of tracks passed by the track IPS filter `L3FIP`. By matching the track from the `L3TMuonPhysicsResults` object with the track from the `L3IPTrackPhysicsResults` object the significance of the muon's impact parameter can be indirectly calculated.

The two tracks are matched if the differences in each track parameter are all less than 1×10^{-5} which is just a rounding error. Unlike `L3FIP`, only one muon can be triggered on. Figure 4.3 shows the IPS for all Level-3 muons in $B_s \to D_s\pi$ MC and in data. Since this is a hadronic B_s decay the muon in the event is the opposite-side tagging muon. The muons have a 3 GeV/c p_T cut.

4.7 Two object invariant mass

This is a versatile filter that can calculate the invariant mass of different objects. Its name is `L3FInvMass` and it takes as input a list of tracks, jets or muons. When tracks or muons are used, the mass hypotheses are supplied and the option of just opposite sign tracks given. If jet objects are used the invariant mass is calculated from the 4 vectors.

Figures 4.4 and 4.5 show the ϕ invariant mass in $B_s \to D_s\pi$ MC ($D_s \to \phi\pi$, $\phi \to K^+K^-$) and data respectively. The actual ϕ mass is 1.02 GeV. There is much higher background in data, as expected. Figure 4.6 shows the result of using muon objects in this filter. The J/ψ peak can clearly be seen at a mass of 3.1 GeV/c^2.

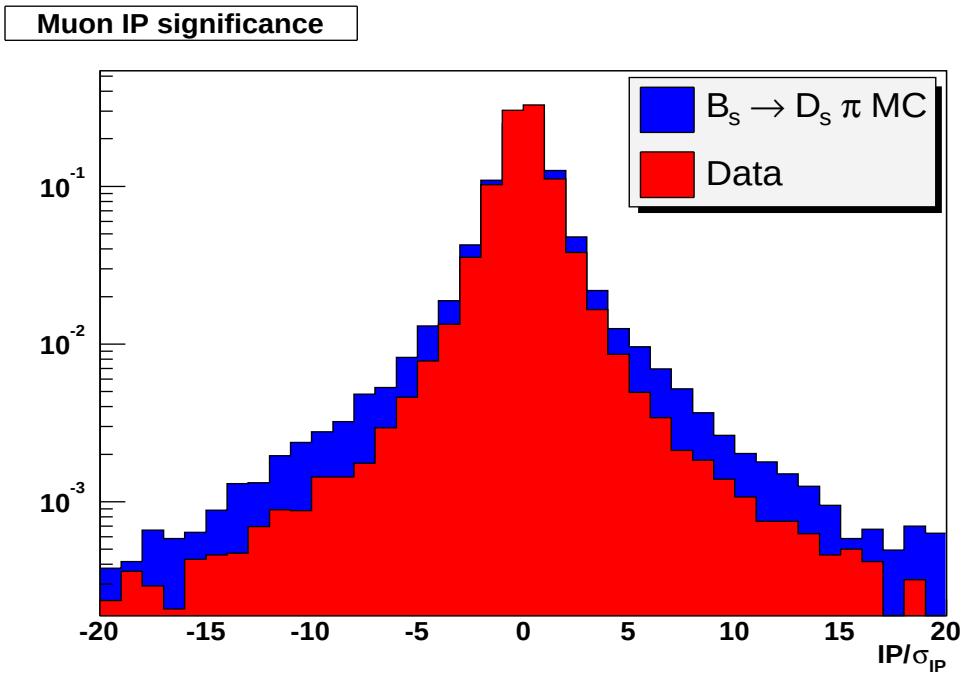

Figure 4.3: Comparison of Level-3 IPS for all muons in $B_s \rightarrow D_s\pi$ MC and data, run 188676.

It is important to note that these plots are for demonstration only. When running this filter online, it is not critical that a peak is seen. Nor is it important what the width or efficiency is. The issue, as with any trigger tool, is whether the filter can reject background events while keeping signal events. This will be demonstrated in the next section.

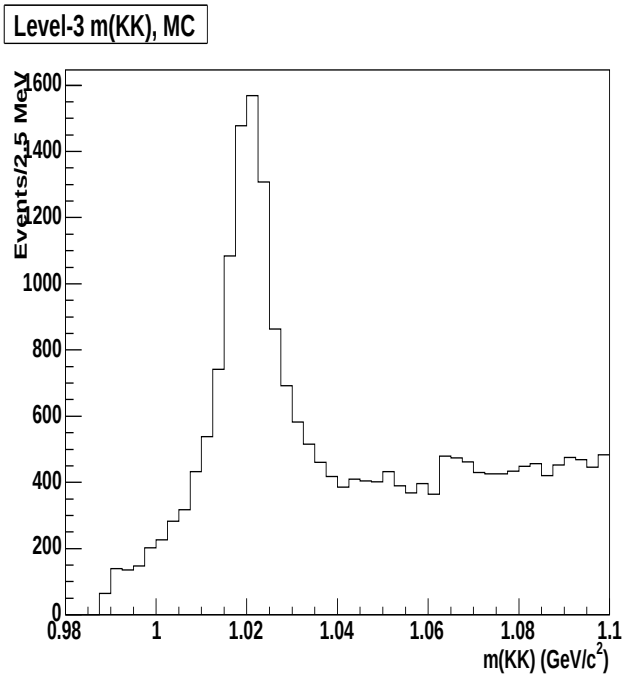

Figure 4.4: Level-3 KK invariant mass in $B_s \to D_s\pi$ MC. The tracks have $p_T > 1.0$ GeV/c and opposite signs. Each track is assigned the K mass (0.494 GeV/c^2).

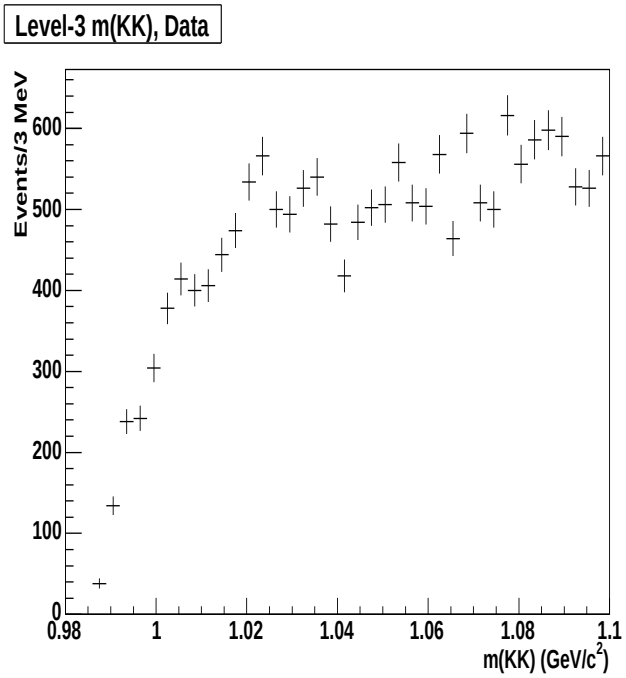

Figure 4.5: Level-3 KK invariant mass in data. The tracks have $p_T > 1.0$ GeV/c and opposite signs. Each track is assigned the K mass (0.494 GeV/c^2).

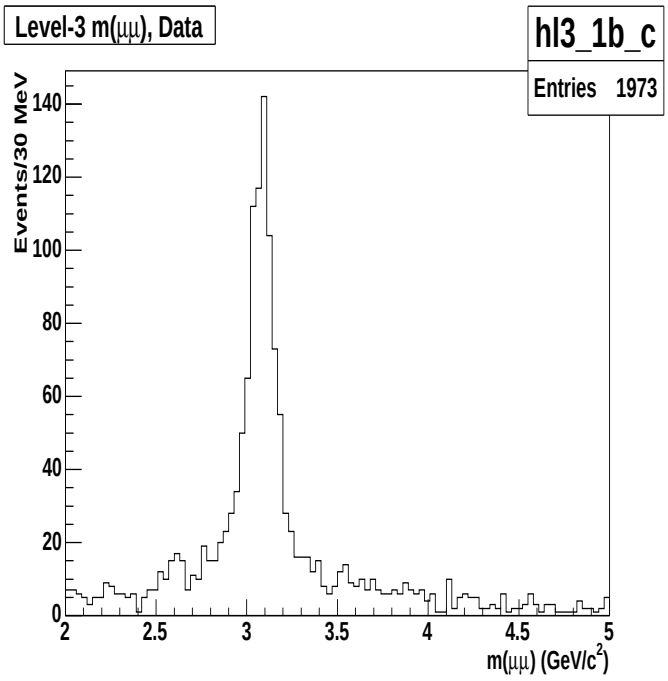

Figure 4.6: Level-3 $\mu\mu$ invariant mass in data.

4.8 Trigger studies

In the following section, the various tools described in this Chapter are studied. As with any trigger tool there is a fine balance between the rejection of background events and the efficiency for passing signal events. Additional factors include the pass rate in Hz, the prescale at a particular instantaneous luminosity and the allowed bandwidth for the trigger in question. Although these factors are related, the prescale and allowed bandwidth are also sociological factors which are time dependent. All these aspects make designing triggers extremely complex. In the following, the efficiencies and rejections of the individual tools are studied. Then they are combined to form certain combinations. These are designed to provide a foundation for creating new triggers. Only by looking at the data they collect can their performance be really evaluated.

4.8.1 Description of method

All the following trigger studies were performed with two samples.

MC $\sim$ 13,000 $B_s \to D_s\pi$ + 0.8 min bias with a $\mu^{\pm}$ $p_T > 3.0$ GeV, $|\eta| < 2.2$

DATA $\sim$ 20,000 events, run 188676, instantaneous luminosity $\sim$15x10^{30}cm^{-2}s^{-1}

The studies were performed in December 2003 so the instantaneous luminosity of the data sample corresponded to the mean luminosity at the time. In addition, the number of minimum bias events in the MC was chosen by the collaboration to approximately equal the number of interactions per bunch crossing in the Tevatron. The MC was generated with the muon p_T and η cuts because these are the minimum requirements for a muon to pass the single muon trigger.

Both samples were run through `d0trigsim`[1] with a triggerlist containing the single muon trigger containing the loose terms at Level-1 and Level-2 and a Level-3 loose muon matched to a 3 GeV central track (see Table 4.2). The efficiency for the MC sample was 44% and the efficiency for data was 25%. The studies used only the events that passed the basic preselection.

The nature of filters is to pass or fail an event and they do not produce their own set of results. Therefore in order to perform the studies, a simulation framework was developed using the `ROOT` analysis package. The code in each filter was transported into `ROOT` and additional code developed to perform the trigger studies. Consistency between the `ROOT` simulation and `d0trigsim` was checked on an event by event basis.

Efficiency and rejection were defined as follows

$$\text{efficiency} = \frac{\text{number of events passing filter}}{\text{total number of events}} \tag{4.3}$$

$$\text{rejection} = \frac{1}{\text{efficiency}} \tag{4.4}$$

[1] `d0trigsim` is the DØ trigger simulator. Version p16.01.00 was used

The efficiency in signal MC is a measure of how well the filter passes signal events. The rejection in data is a measure of how well the filter rejects background events. In all these studies, it is assumed that data represents the background. In fact, there will be some B content as an event containing a muon is more likely to contain a B, but this effect is small enough to ignore for these purposes. This is currently the practice in the B physics group at DØ since data, at present, better represents the background than MC.

4.8.2 Individual filter performance

Figures 4.7 to 4.14 show a selection of plots displaying efficiency and rejection versus IPS for the individual filters. For each filter, the efficiencies and rejections were studied for a range of parameters. Two plots, which correspond to the maximum efficiency and maximum rejection configurations, are shown for each filter. If a filter's rejection in data is equal to 1/efficiency for signal then it rejects signal and background in equal amounts. Therefore, for a filter to be effective, the rejection on real data must be greater than 1/efficiency for signal so that it rejects more backround than signal.

IP_TRK_2SMT_MMX_PTX

This is the test filter for `L3FIP`, the track IPS filter, and has the following components:

MMX - Level-3 track matched muon p_T requirement

IP `L3FIP` - IPS filter

TRK - One track with IPS, satisfying:

2SMT - 2 axial SMT hits

PTX - $p_T >$ X

Figure 4.7 shows the efficiency and rejection versus IPS with MM3 (Level-3 track matched muon $p_T > 3.0$ GeV) and PT0.5 (track $p_T > 0.5$ GeV). The IPS of the track is along the x axis. On the left y axis is the efficiency, with the efficiency represented by the solid curve. The right y axis is the rejection and the rejection is represented by the curve with triangles. For any value of track IPS the efficiency and rejection are read off the relevant curve. For example, by requiring the track IPS to be > 2, the rejection is around 1.5 with an efficiency of 90%. (Note, all efficiencies are with respect to the total passing MM3).

Figure 4.8 shows the efficiency and rejection versus IPS with MM5 (Level-3 track matched muon $p_T > 5.0$ GeV) and PT2 (track $p_T > 2.0$ GeV). This figure shows that by requiring MM5 the efficiency drops and the rejection increases significantly. For example, by requiring track IPS > 3, the efficiency is 16% and the rejection is 9.

IP_2TRK_2SMT_MMX_PTX

This test filter is analogous to the previous one, IP_TRK_2SMT_MMX_PTX, but now 2 tracks are required to satisfy the conditions. Figures 4.9 and 4.10 show the efficiency and rejection versus IPS with MM3 and PT0.5 (both tracks $p_T > 0.5$ GeV) and MM5 and PT2 (both tracks $p_T > 2.0$ GeV) respectively. Requiring multiple tracks with IPS improves both efficiency and rejection. Compare Figure 4.8, which is the single track case, to Figure 4.10 the two track case. For the same efficiency (16%), the rejection in the one track case is around 9 and in the two track case it is around 11.5.

MIP_2SMT_MMX_PT0

This is the test filter for `L3FPhysIP`, the muon IPS filter. It is comprised of:

MMX - Level-3 track matched muon p_T requirement

2SMT - 2 axial SMT hits on the muon track

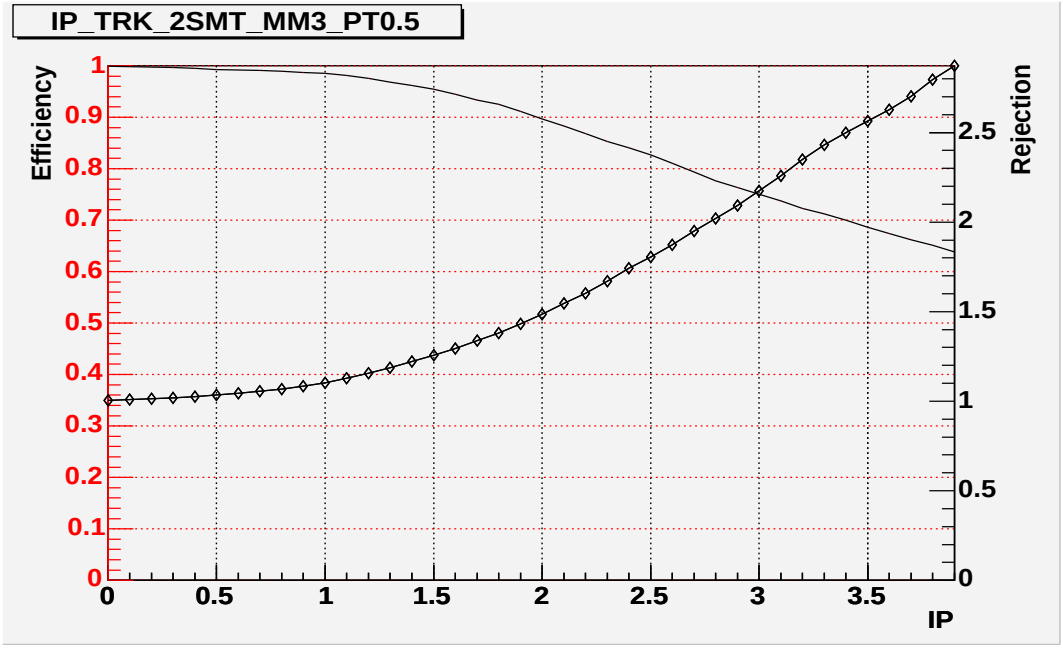

Figure 4.7: Efficiency and rejection versus IPS for IP_TRK_2SMT_MM3_PT0.5 (3 GeV/c track matched muon plus one track with $p_T > 0.5$ GeV/c, 2 axial SMT hits and IPS > X). The left y axis is the efficiency with efficiency represented by the solid curve. The right y axis is the rejection with rejection represented by the curve with triangles.

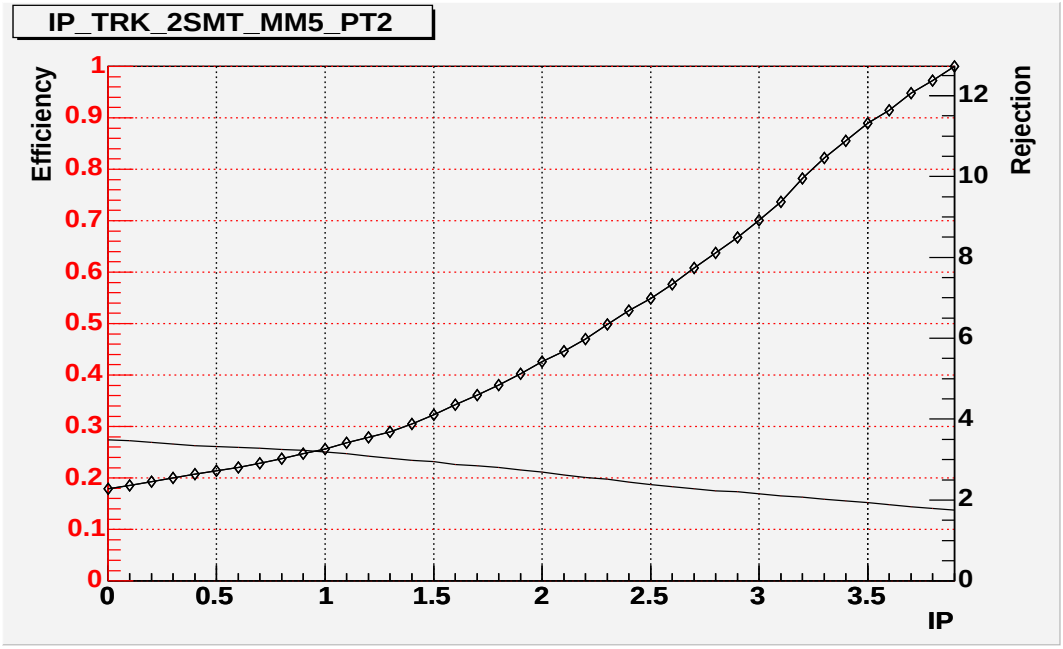

Figure 4.8: Efficiency and rejection versus IPS for IP_TRK_2SMT_MM5_PT2 (5 GeV/c track matched muon plus one track with $p_T > 2$ GeV/c, 2 axial SMT hits and IPS > X). The left y axis is the efficiency with efficiency represented by the solid curve. The right y axis is the rejection with rejection represented by the curve with triangles.

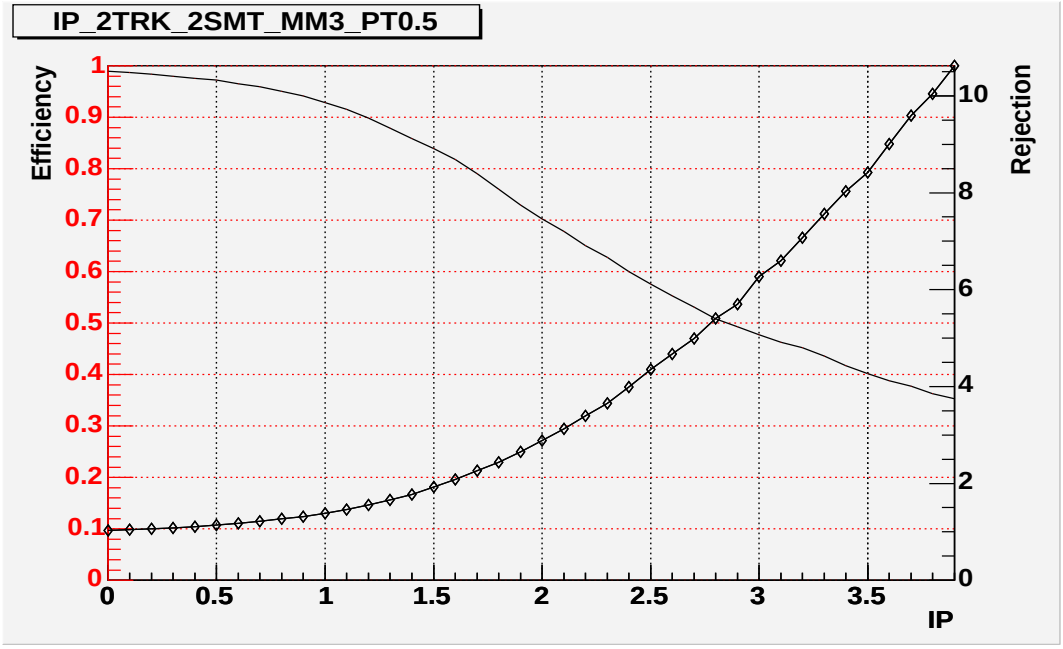

Figure 4.9: Efficiency and rejection versus IPS for IP_2TRK_2SMT_MM3_PT0.5 (3 GeV/c track matched muon plus two tracks, both with $p_T > 0.5$ GeV/c, 2 axial SMT hits and IPS > X). The left y axis is the efficiency with efficiency represented by the solid curve. The right y axis is the rejection with rejection represented by the the curve with triangles .

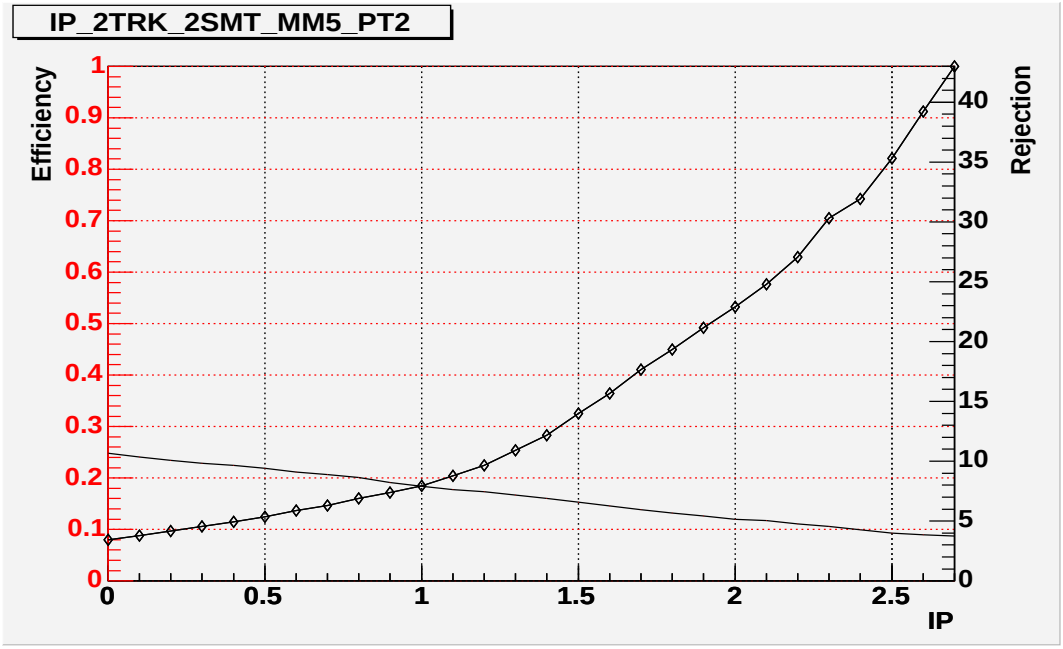

Figure 4.10: Efficiency and rejection versus IPS for IP_2TRK_2SMT_MM5_PT2 (5 GeV/c track matched muon plus two tracks, both with $p_T > 2.0$ GeV/c, 2 axial SMT hits and IPS > X). The left y axis is the efficiency with efficiency represented by the solid curve. The right y axis is the rejection with rejection represented by the the curve with triangles .

MIP L3FPhysIP - Muon IPS filter

PT0 - No additional p_T cuts

Figures 4.11 and 4.12 show the efficiency and rejection versus muon IPS with a muon p_T cut of > 3.0 and 5.0 GeV/c respectively. The x axis displays the muon IPS. In the former case, with an IPS > 1.75, the efficiency is 50% with a rejection of around 3.5. In the latter case, an efficiency of 10% and a rejection of 12 is achieved with an IPS > 2.5. These values show that the trigger is effective.

INVMASS_MMX_PTX

This is the test filter for `L3FInvMass`, the two track invariant mass filter. It is comprised of:

MMX - Level-3 track matched muon p_T requirement

INVMASS `L3FInvMass` - Two track invariant mass in the ϕ mass range

PTX - Both tracks with a total of ≥ 10 axial hits and $p_T >$ X

Figure 4.13 shows the efficiency and rejection curves for MM3 (Level-3 track matched muon $p_T > 3.0$ GeV) and PT0.5 (both tracks forming the invariant mass have $p_T >$ 0.5 GeV). The x axis displays the size of the ϕ mass window which is centred on 1.02 GeV/c^2. Figure 4.14 shows the efficiency versus rejection curve for MM5 (Level-3 track matched muon $p_T > 5.0$ GeV) and PT2 (both tracks forming the invariant mass have $p_T > 2.0$ GeV). The efficiency is low ($\sim 5\%$) but the rejections are very large which will be critical in the case of high instantaneous luminosities.

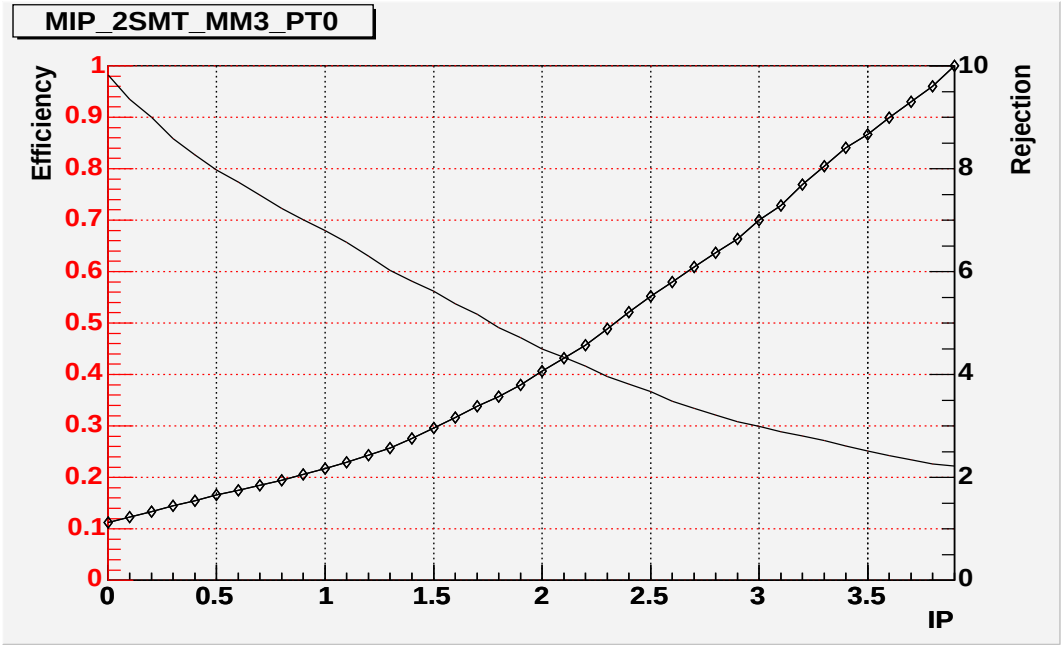

Figure 4.11: Efficiency and rejection versus muon IPS for MIP_2SMT_MM3_PT0 (3 GeV/c track matched muon with 2 axial SMT hits and IPS > X). The left y axis is the efficiency with efficiency represented by the solid curve. The right y axis is the rejection with rejection represented by the the curve with triangles .

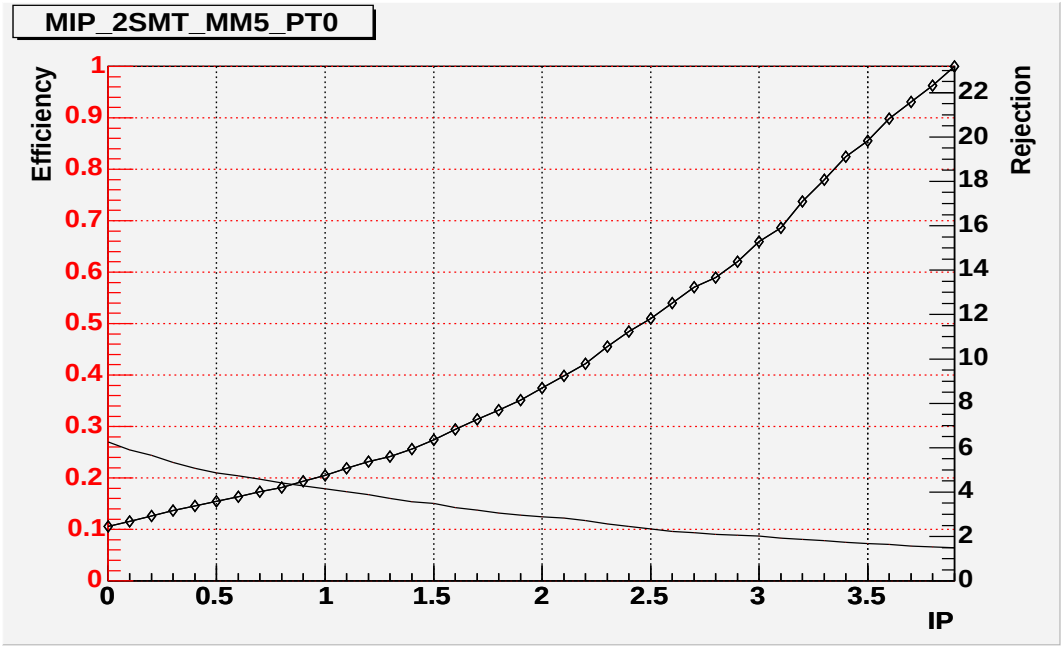

Figure 4.12: Efficiency and rejection versus muon IPS for MIP_2SMT_MM5_PT0 (5 GeV/c track matched muon with 2 axial SMT hits and IPS > X). The left y axis is the efficiency with efficiency represented by the solid curve. The right y axis is the rejection with rejection represented by the the curve with triangles .

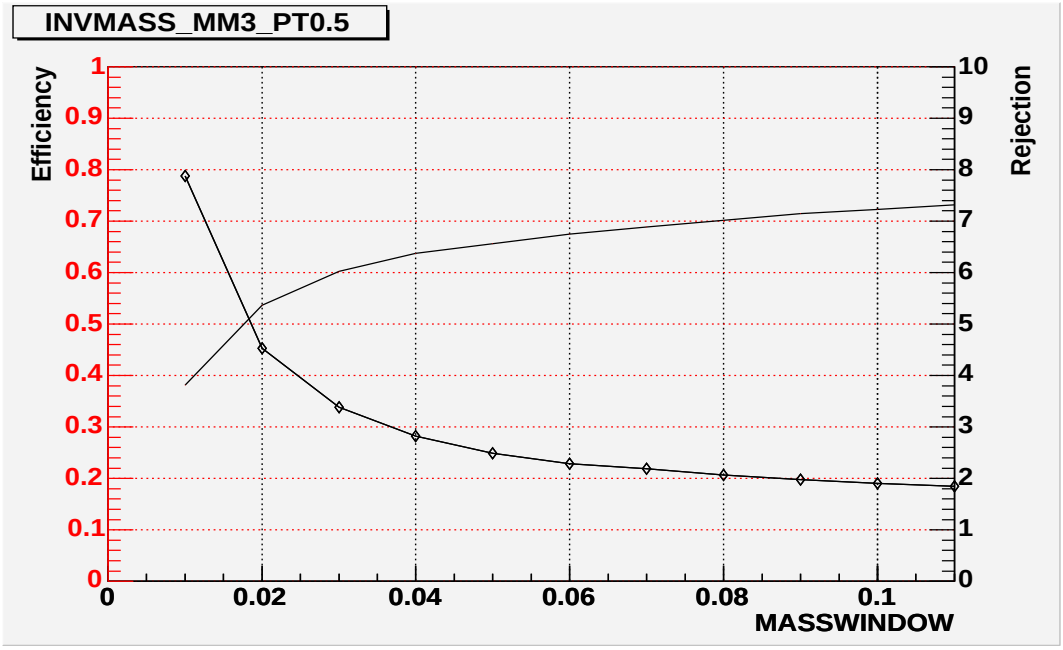

Figure 4.13: Efficiency and rejection curves for INVMASS_MM3_PT0.5 (3 GeV/c track matched muon plus two tracks with $\geq$ 10 axial total hits and $p_T > 0.5$ GeV in the ϕ mass range). The x axis is the mass window in GeV/c^2 centred on 1.02 GeV/c^2. The left y axis is the efficiency with efficiency represented by the solid curve. The right y axis is the rejection with rejection represented by the the curve with triangles .

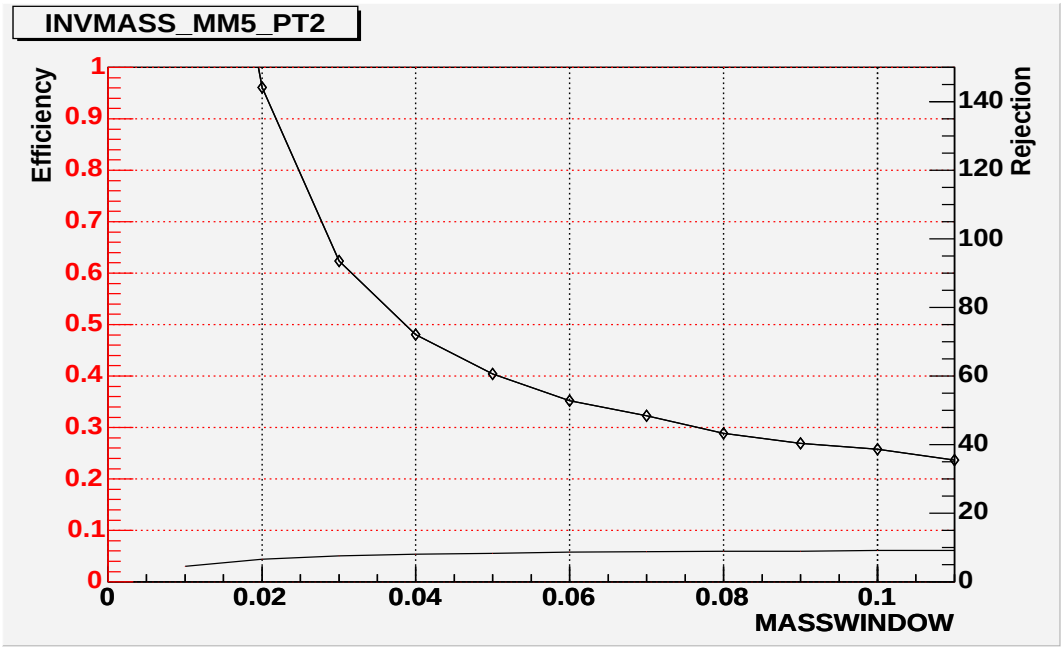

Figure 4.14: Efficiency and rejection curves for INVMASS_MM5_PT2 (5 GeV/c track matched muon plus two tracks with $\geq$ 10 axial total hits and $p_T > 2.0$ GeV in the ϕ mass range). The x axis is the mass window in GeV/c^2 centred on 1.02 GeV/c^2. The left y axis and the solid curve represent efficiency. The right y axis and the the curve with triangles represent rejection.

4.8.3 Combined filters

In this section an example of one of the possible combinations of these filters is studied. The filter is essentially the muon IPS plus the invariant mass filter. This filter is designed for B_s decays in which there is a ϕ in the final state. The muon is either from the opposite side B (as in the case of hadronic decays) or from the semileptonic B_s decay.

MIP_2SMT_INVMASS_MMX_PTX

This test filter is comprised of:

MMX - Level-3 track matched muon p_T requirement

2SMT - 2 axial SMT hits on muon track

MIP L3FPhysIP - Muon IPS filter

INVMASS L3FInvMass - Two track invariant mass in the ϕ mass range

PTX - Both tracks with $\geq$ 10 total axial hits and $p_T >$ X

Figure 4.15 shows the efficiency and rejection curves for MM3 (Level-3 track matched muon $p_T > 3.0$ GeV) and PT0.5 (both tracks forming the invariant mass have $p_T >$ 0.5 GeV). The x axis is the muon IPS. The ϕ mass range is fixed at 0.98-1.06 GeV/c^2. An efficiency of 50% gives a rejection of above 4 when the muon IPS is > 0.85. This is a significant improvement on the performance of the muon impact parameter filter, as seen in Figure 4.11.

Figure 4.16 shows the efficiency and rejection curves for MM5 and PT2. The rejection rates for this filter are very large, critical at the highest instantaneous luminosities. Even though the efficiency is low ($\sim$ 5%) this is still a very effective trigger.

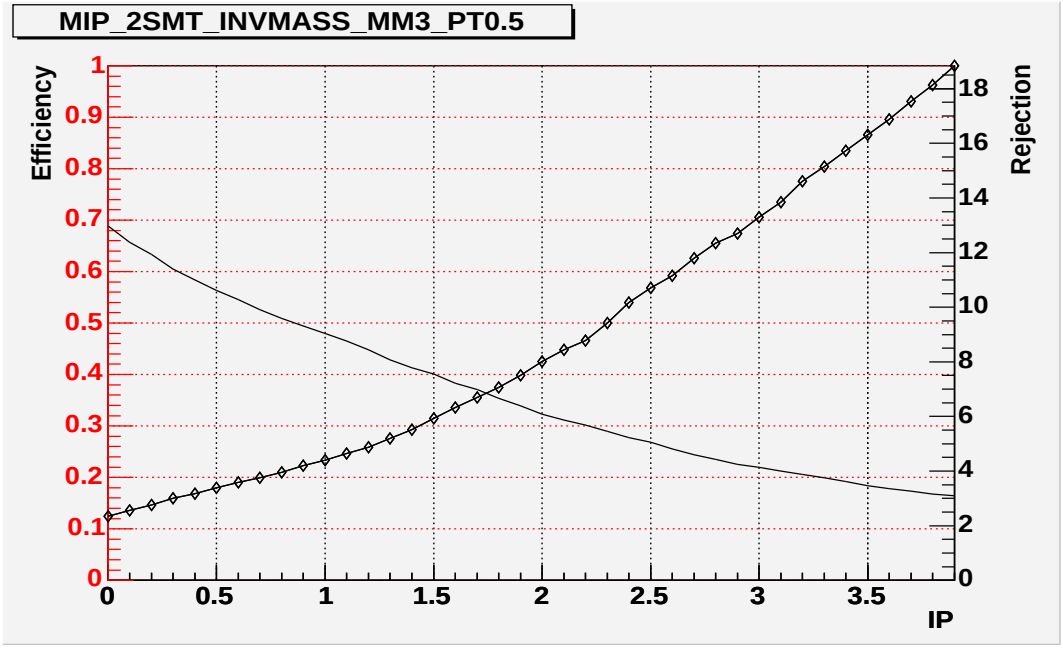

Figure 4.15: Efficiency and rejection curves for MIP_2SMT_INVMASS_MM3_PT0.5 (3 GeV/c track matched muon with 2 axial SMT hits and IPS > X plus two tracks with $\geq$ 10 axial total hits and $p_T > 0.5$ GeV/c in the ϕ mass range 0.98-1.06 GeV/c^2). The left y axis and the solid curve represent efficiency. The right y axis and the the curve with triangles represent rejection.

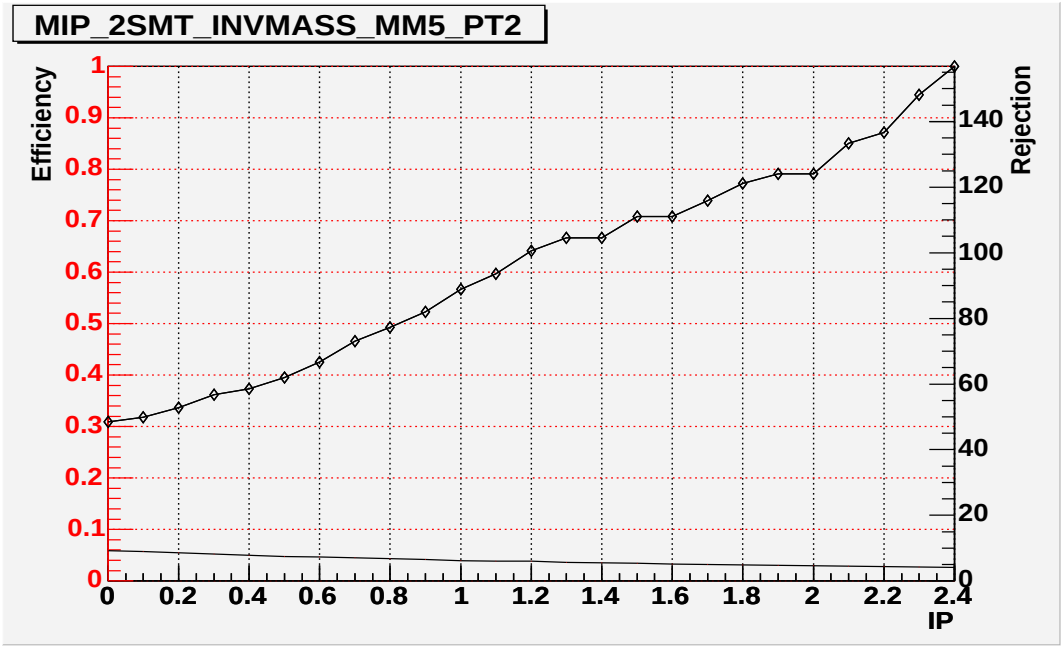

Figure 4.16: Efficiency and rejection curves for MIP_2SMT_INVMASS_MM5_PT2 (5 GeV/c track matched muon with 2 axial SMT hits and IPS > X plus two tracks with $\geq$ 10 axial total hits and $p_T > 2.0$ GeV/c in the ϕ mass range 0.98-1.06 GeV/c^2). The left y axis and the solid curve represent efficiency. The right y axis and the the curve with triangles represent rejection.

4.8.4 Trigger studies summary

The studies performed have shown these new filters to be effective in that they reject significantly more background events than signal events. It has also been demonstrated that very large rejections can be obtained with respect to the single muon trigger at Level-3. Although the efficiencies appear to be low, they have to be considered in comparison to prescales. As already stated, an efficiency of 10% is preferred to a prescale of 10. In addition, the efficiency with respect to the final B_s analysis cuts will be much higher, since signal events that fail these filters may never be reconstructed.

Combinations of these filters will allow the single muon trigger to run unprescaled at the highest instantaneous luminosities, where without these new filters, it would be completely turned off.

4.9 The v13 triggerlist

The v13 triggerlist first ran online at the end of June 2004. Many new trigger tools were available, especially the tools and filters described in this chapter. Here is an outline of the new triggers, including different combinations of the new Level-3 filters, used in v13. The terms LOOSE/TIGHT at Level-1 or Level-2 refer to Table 4.2.

The first family requires a 3.0 GeV muon at Level-1 and a 4.0 GeV muon at Level-3. The Level-3 requirements are muon IPS or multiple track IPS with 2 tracks in the ϕ mass range. These triggers run unprescaled up to approximately $60\text{x}10^{30}\text{cm}^{-2}\text{s}^{-1}$ where they start to receive prescales. This is already a major improvement on the old single muon triggers.

ML1_IPTLM_IMP_V Level-1: LOOSE. Level-2: TIGHT.

Level-3: 1 track matched muon with $p_T > 4$ GeV/c and IP significance > 3.0.

2 tracks with $p_T > 0.5$ GeV/c, opposite sign, in ϕ mass range.

Primary Vtx $|z| < 35$ cm.

ML1_TLM_2IP_IMP_V Level-1: LOOSE. Level-2: TIGHT.

Level-3: 1 track matched muon with $p_T > 4$ GeV/c.

2 tracks with $p_T > 1.5$ GeV/c and IP significance > 3.0.

2 tracks with $p_T > 0.5$ GeV/c, opposite sign, in ϕ mass range.

Primary Vtx $|z| < 35$ cm.

ML1_TLM_3IP_IMP_V Level-1: LOOSE. Level-2: TIGHT.

Level-3: 1 track matched muon with $p_T > 4$ GeV/c.

3 tracks with $p_T > 0.75$ GeV/c and IP significance > 3.0.

2 tracks with $p_T > 0.5$ GeV/c, opposite sign, in ϕ mass range.

Primary Vtx $|z| < 35$ cm.

ML1_TLM_4IP_IMP_V Level-1: LOOSE. Level-2: TIGHT.

Level-3: 1 track matched muon with $p_T > 4$ GeV/c.

4 tracks with $p_T > 0.5$ GeV/c and IP significance > 3.0.

2 tracks with $p_T > 0.5$ GeV/c, opposite sign, in ϕ mass range.

Primary Vtx $|z| < 35$ cm.

The second family of triggers requires a 5.0 GeV/c muon both at Level-1 and Level-3. The Level-2 requirement is loosened. The other Level-3 requirements are exactly the same. This family of triggers runs unprescaled.

ML1_IPTLM5_IMPV Level-1: TIGHT. Level-2: LOOSE.

Level-3: 1 track matched muon with $p_T > 5$ GeV/c and IP significance > 3.0.

2 tracks with $p_T > 0.5$ GeV/c, opposite sign, in ϕ mass range.

Primary Vtx $|z| < 35$ cm.

MM1_TLM_IMP_2IPV Level-1: TIGHT. Level-2: LOOSE.

Level-3: 1 track matched muon with $p_T > 5$ GeV/c.

2 tracks with $p_T > 1.5$ GeV/c and IP significance > 3.0.

2 tracks with $p_T > 0.5$ GeV/c, opposite sign, in ϕ mass range.

Primary Vtx $|z| < 35$ cm.

MM1_TLM_IMP_3IPV Level-1: TIGHT. Level-2: LOOSE.

Level-3: 1 track matched muon with $p_T > 5$ GeV/c.

3 tracks with $p_T > 0.75$ GeV/c and IP significance > 3.0.

2 tracks with $p_T > 0.5$ GeV/c, opposite sign, in ϕ mass range.

Primary Vtx $|z| < 35$ cm.

MM1_TLM_IMP_4IPV Level-1: TIGHT. Level-2: LOOSE.

Level-3: 1 track matched muon with $p_T > 5$ GeV/c.

4 tracks with $p_T > 0.5$ GeV/c and IP significance > 3.0.

2 tracks with $p_T > 0.5$ GeV/c, opposite sign, in ϕ mass range.

Primary Vtx $|z| < 35$ cm.

In addition to these families of triggers there is also a muon + electron trigger family that require track IPS and invariant mass in the ϕ mass range.

Figures 4.17 to 4.19 show the Level-1, Level-2 and Level-3 trigger cross sections as a function of luminosity for the MM1_TLM_IMP_2IPV trigger. The trigger cross section is defined as the ratio of the rate and instantaneous luminosity and takes account of any dead time and pauses. This particular trigger was chosen because it never received a prescale.

The ideal behaviour would be a linear relation with no gradient as this implies that the rate increases linearly with the luminosity. This is clearly not the case for Level-1 and Level-2 as the trigger cross sections increase non-linearly with luminosity. With higher luminosities there is higher occupancy in all detector subsystems. In the muon systems there is a higher fake rate which causes more events to be triggered.

The Level-3 case is different. It does display approximately linear behaviour but the cross section decreases with luminosity. This implies at higher luminosities the trigger passes a lower fraction of events. The CFT and SMT have higher occupancies like the muon system but in the case of the fast tracking algorithms employed at

Level-3, the density of hits in the detectors causes fakes but also reduces the quality of the real tracks. The tracks fail quality cuts and the event may fail. At the present time, there is considerable effort being made in addressing these problems.

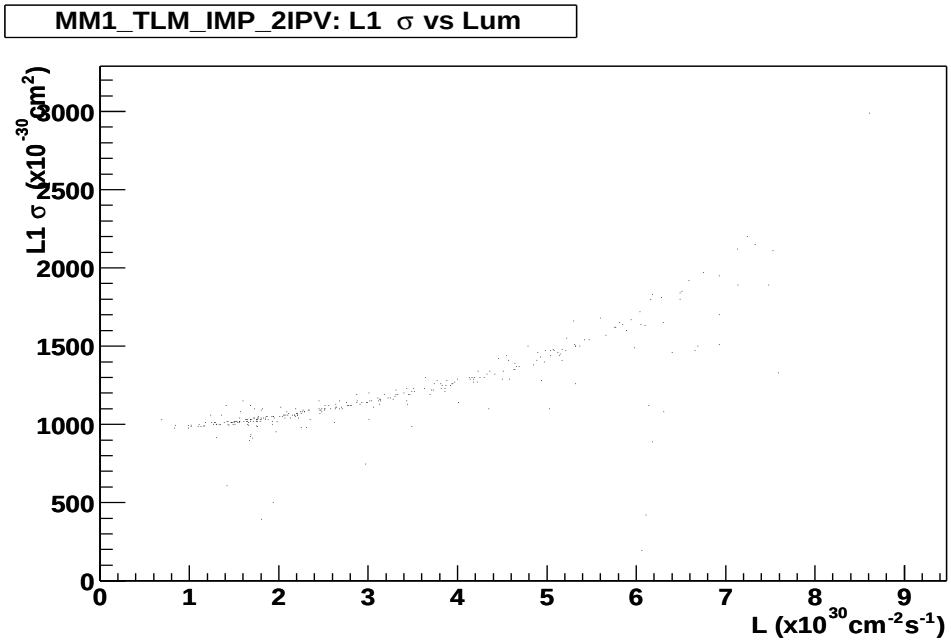

Figure 4.17: Level-1 trigger cross-section as a function of luminosity for MM1_TLM_IMP_2IPV.

4.10 Summary

The addition of these new triggers using impact parameter significance and invariant mass is critical to the B physics programme at DØ. In comparison, the triggers in the list with the old Level-3 requirements (muon + tracks for example) are prescaled away at anywhere from 10-50x10^{30}cm^{-2}s^{-1}. Essentially, the single muon trigger never ran without a prescale. Prescales severely reduce the sensitivity to B_s oscillations [47]. This was a major concern, especially as the instantaneous luminosity is increasing. Prior to the v13 triggerlist and the filters described in the chapter the prospects of finding B_s mixing in the hadronic mode were poor. The work performed here, allows the experiment to not only run a single muon trigger at all luminosities,

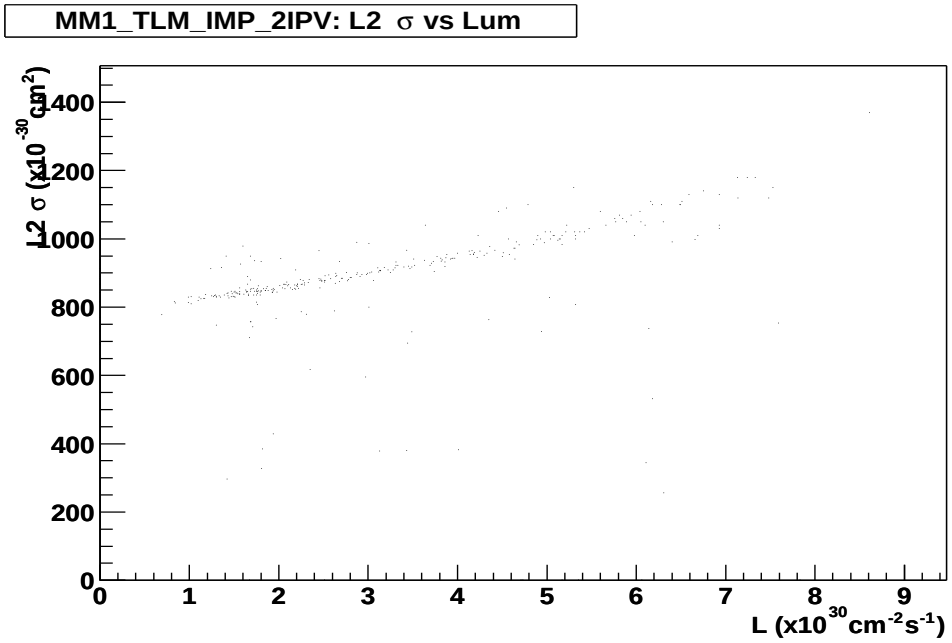

Figure 4.18: Level-2 trigger cross-section as a function of luminosity for MM1_TLM_IMP_2IPV.

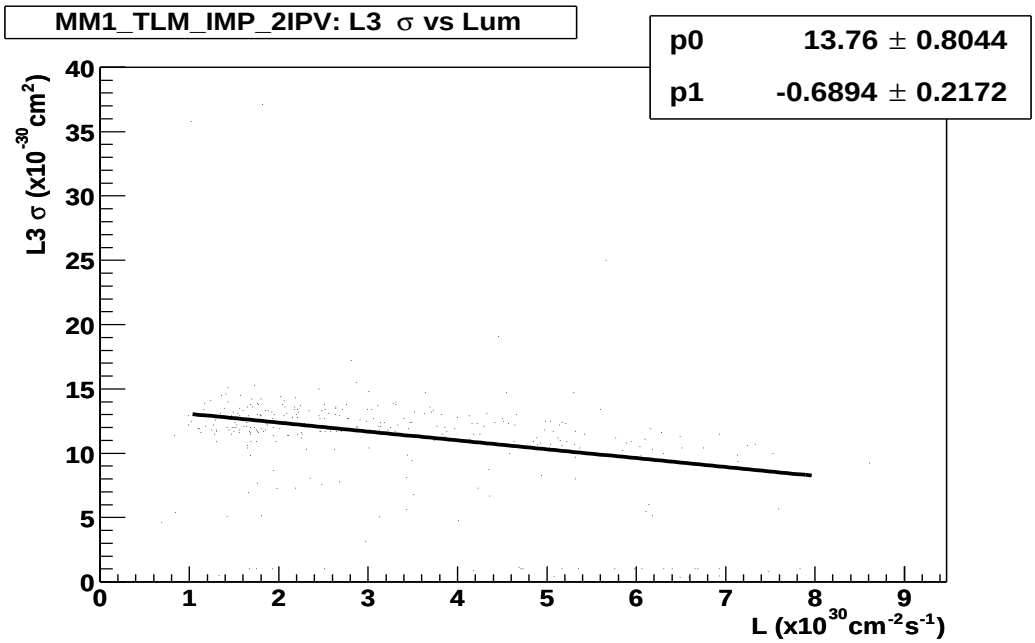

Figure 4.19: Level-3 trigger cross-section as a function of luminosity for MM1_TLM_IMP_2IPV.

but to run it without prescales. This has made the discovery of B_s mixing in both the semileptonic and hadronic modes a real prospect.

Chapter 5

Analysis

The $B_s^0 \to D_s^- \pi^+$ mode is known as the "Golden mode" for B_s mixing.[1] This is because the fully reconstructed B_s provides the optimum momentum and proper time resolution which is critical for resolving the rapid oscillations. Conversely the semileptonic mode, $B_s \to D_s^- \mu^+ X$, has missing momentum due to an unreconstructed neutrino.

The branching ratio for the semileptonic channel is (7.9±2.4)%) [5]. The branching ratio for the hadronic channel has now been measured at CDF and found to be around 4.2×10^{-3} [48]. At DØ the hadronic events must be collected using a single muon trigger where the opposite side B has decayed semileptonically. For this reason, the expected number of hadronic events is much less than the expected number of semileptonic events. However, hadronic events collected in this way already have an opposite side muon that can be used to tag the initial state flavour of the B_s. These hadronic decays are, therefore, extremely important to the DØ experiment.

This Chapter initially describes the reconstruction of the $B_d^0 \to D^{*-} \pi^+$ and $B_s^0 \to D_s^- \mu^+ X$ decay channels which provide excellent cross checks of the analysis. Then the reconstruction of $B_s^0 \to D_s^- \pi^+$ is described and the first observation at DØ presented. Finally, DØ's predicted sensitivity for B_s mixing is calculated, using the information gained from the reconstruction of this important mode.

[1] Charge conjugate modes also are implied throughout.

5.1 Reconstruction software

5.1.1 d0reco tracking algorithms

d0reco is the official DØ event reconstruction software. Currently (as of version p14) the tracking utilises three different algorithms to reconstruct charged particle trajectories within the DØ detector. Pattern recognition is performed by the AA [49], [50] and HTF [51] algorithms.

The AA algorithm constructs initial track hypotheses from three hit combinations in the SMT. Each track hypothesis is extrapolated to the next layer and a hit associated if one exists within a $\Delta\phi$ window. If there is no hit present in that layer then a miss is associated. All possible hypotheses are constructed and tracks can share hits. The HTF algorithm utilises a Hough transformation to convert hits into lines in $(q/p_T, \phi)$ space. The intersections of the lines represent the track parameters. By histogramming the parameter space and finding the maximum bins track hypotheses are constructed.

All the track hypotheses formed from the AA and HTF algorithms are ordered and then filtered according to criteria dependent on the number of individual hits, shared hits and misses. The filtering occurs on the most likely hypotheses first and if a hypothesis passes, all hypotheses sharing those hits are removed. The final stage of track finding uses the GTR algorithm [52] which uses a Kalman Track Fit together with the DØ interacting propagator [53]. The latter propagates the tracks accounting for the magnetic field, multiple scattering and energy loss.

The tracking efficiency as a function of p_T and η for all tracks is shown in Figure 5.1. The MC sample used was $Z \to \mu\mu$ plus an average of two minimum bias events. Note the excellent coverage down to ~300 MeV in p_T and out to ~4 in $|\eta|$.

5.1.2 BANA

The basic reconstruction package used throughout this analysis is called BANA [54] and it is the default for the B physics group. It performs primary vertexing with a

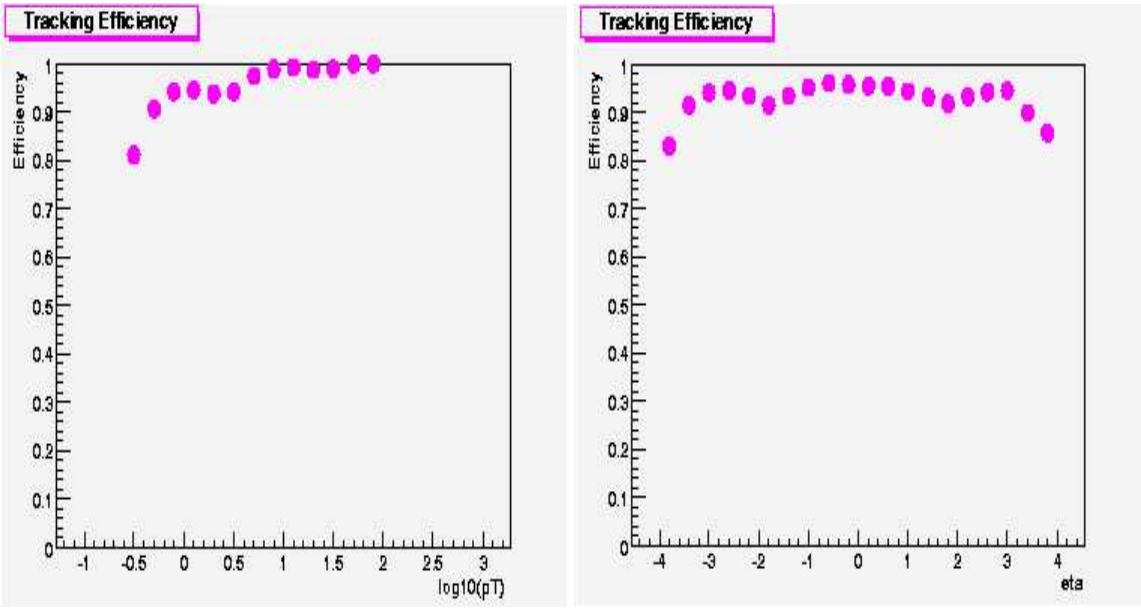

Figure 5.1: `d0reco` tracking efficiency as a function of $\log_{10}(p_T)$ (p_T in GeV/c) and η. The MC sample used was $Z \to \mu\mu$ plus an average of two minimum bias events.

beamspot constraint using the methods described in [55]. In addition it performs track jet clustering using the Durham algorithm [56] and V_0 and secondary vertex finding. Recent additions have been flavour tagging and silicon dE/dx information. The package also provides an interface to the Monte Carlo truth information.

5.1.3 Muon reconstruction

The muons used in both the semileptonic and hadronic analyses were required to meet the following criteria:

- hits in both the A and BC layers of the muon system
- at least two wire hits in both the A and BC layers
- at least one scintillator hit in both the A and BC layers
- χ^2 of the muon system fit > 0
- a match to a track in the inner tracking system
- $p_T(\mu) > 2.0$ GeV/c, $p(\mu) > 3.0$ GeV/c and $|\eta| < 2$.

These cuts represent the official DØ certified muon criteria [57].

5.2 Preliminary studies: $B_d^0 \to D^{*-}\pi^+$

In order to ascertain whether the reconstruction of hadronic B_s decays was feasible at DØ, some preliminary studies were made using the mode $B_d^0 \to D^{*-}\pi^+$, where $D^{*-} \to \overline{D}^0\pi^-$ and $D^0 \to K^-\pi^+$. The kinematics of the $D^* \to D^0\pi$ decay allow a tight cut on the invariant mass, namely $M(D^*) - M(K\pi) \geq M(\pi^+)$ (within detector resolution), which gives a large reduction in the background. This mode acts as an important cross-check since it shows that the collection of hadronic decays by triggering on muons from the opposite side B decay is possible.

The data used for this study correspond to approximately 250 pb^{-1} collected between April 2002 and January 2004. The triggerlists used were previous to version 13 and therefore did not contain any impact parameter significance or invariant mass triggers.

The cuts used were developed over a period of time and they were first tested on MC to check their suitability and reconstruction efficiency. The MC does not adequately describe the data where there is a higher number of fake and real tracks. Therefore the reconstruction was then applied to the data and the cuts tuned to maximise the number of signal events. All the mass window sizes are set from data. This is the standard method for the development of analyses in the B physics group at DØ.

5.2.1 Reconstruction cuts

Each track was required to have at least 2 SMT and 6 CFT hits to cut fake and poorly reconstructed tracks.

The D^0 was reconstructed via a two track vertex with each track satisfying $p_T >$ 0.7 GeV/c and impact parameter significance > 2 which helps to reduce combinatoric background. Both tracks had to come from the same jet and to remove semileptonic

decays, events were discarded if the jet contained a muon. The χ^2 of the vertex was required to be < 9 to ensure a good vertex and the invariant mass of the D^0 candidate had to satisfy $1.75 < M(K\pi) < 1.95$ GeV/c^2. Note that since there was no particle identification, both $K\pi$ and πK hypotheses were attempted.

The D^0 candidate was then vertexed with another track to form the D^* candidate. This "soft" pion has a much lower p_T spectrum than the other tracks so it had no p_T cut and was not required to come from the same jet as the D^0 tracks. The difference in the D^* and D^0 invariant masses was required to satisfy $0.142 < M(D^*) - M(D^0) < 0.149$ GeV/c^2 which selects the real D^* candidates.

The D^* candidate was then vertexed with a track from the same jet as the tracks that formed the D^0. It had to satisfy $p_T > 2.0$ GeV/c and impact parameter significance > 2. The cuts on the final pion are very tight since this is where the majority of the combinatoric background originates. The χ^2 of the vertex had to be < 9 to ensure a good vertex. The decay length significance of the B_d was required to be > 3 which ensures that it is incompatible with the primary vertex. The momentum, $p(B_d)$, had to be > 6 GeV/c. Finally, the cosine of the angle between the muon and the B_d candidate had to be $<$ -0.5 which selects the B_d candidates with an opposite side muon.

5.2.2 Results

Figure 5.2 shows the invariant mass of the B_d candidates. A Gaussian signal function plus a second order polynomial to describe the background were fitted to the data. The number of signal events is 72 ± 17. This is the first observation of a fully hadronic B decay at DØ. Since the branching fractions for the decays $B_d^0 \to D^{*-}\pi^+\pi^0$ and $B_d^0 \to D^{*-}\pi^+$ are (1.5±0.5)% and (2.76±0.21)$\times 10^{-3}$ respectively [5] the peak is expected to be due to both modes.

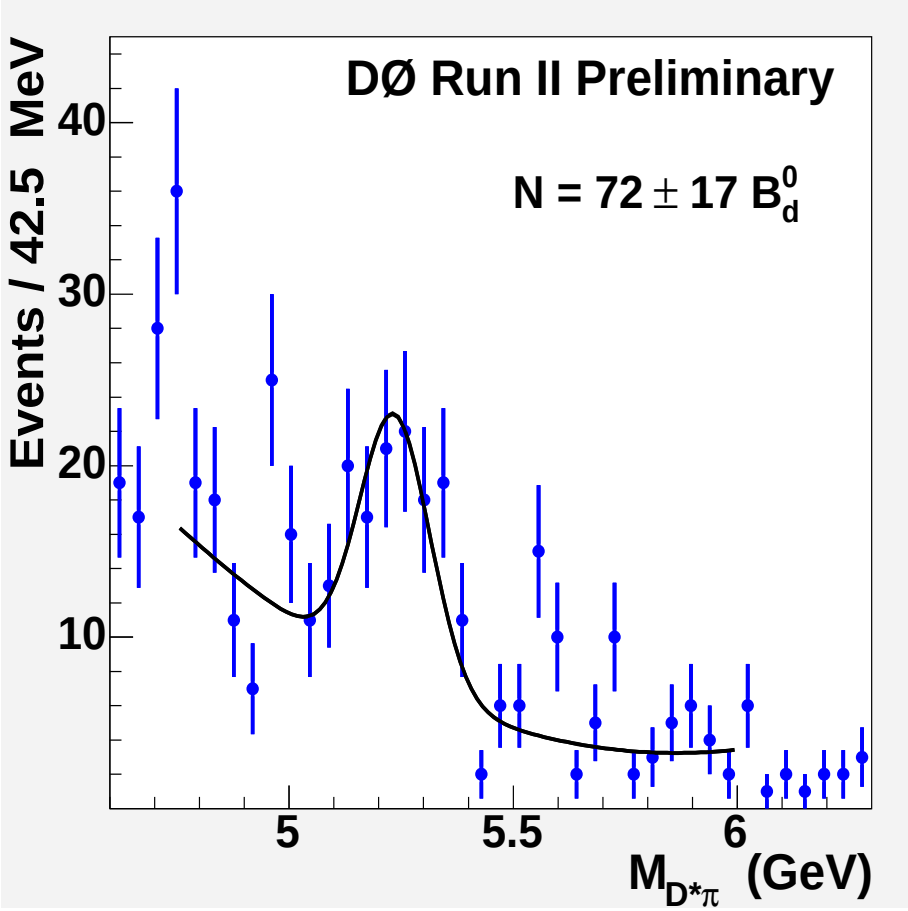

Figure 5.2: Invariant mass of B_d candidates in data. The fit function consists of a Gaussian signal plus a second order polynomial background.

5.3 Triggerlist v13 data sample

This consisted of ∼70 pb^{-1} [58] of data collected with the v13 trigger list described in Chapter 4. These were collected between the end of June 2004 and the end of August 2004 when the Tevatron shutdown commenced. The data were reconstructed using the p14 version of `d0reco`.

Even though the full DØ data set at this time was much larger, ∼ 450 pb^{-1}, only the data collected with the v13 triggerlist were expected to yield an observable number of $B_s^0 \to D_s^- \pi^+$ decays since the v13 triggerlist contained multiple triggers specifically designed to collect these events. These are the track and muon impact parameter significance and ϕ invariant mass cuts as described in Chapter 4.

5.4 $B_s \to D_s^- \mu^+ X$

Successful reconstruction of the semileptonic mode, $B_s \to D_s^- \mu^+ X$, provides an excellent foundation for the reconstruction of hadronic decays. This is because in terms of the reconstruction method, the D_s meson in the semileptonic and hadronic decay modes are almost identical. The cuts for reconstructing this mode, described in Section 5.4.1, were developed in the same way as those in Section 5.2. The MC does not adequately describe the data because of the larger number of fake and real tracks. The code is tested on MC and then applied to data. The mass windows were set from data and the cut values varied to give the maximum number of signal events in data. The values used here were motivated by the official cuts for DØ B hadron reconstruction [59] and the B_s semileptonic mixing analysis [60].

5.4.1 Reconstruction cuts

The D_s was reconstructed via a three track vertex. Each track was required to have at least 2 SMT and 2 CFT hits, to have a $p_T > 0.7$ GeV/c and be in the same Durham jet. Two of the tracks were required to have opposite signs and an invariant mass in the ϕ range $1.008 < M(KK) < 1.028$ GeV/c^2 assuming a kaon hypothesis. In addition, the impact parameter significances of one of the kaon tracks and the pion track were required to be > 2 which additionally reduces combinatorics. The χ^2 of the D_s vertex was required to be < 16 to ensure a good vertex. The decay length significance of the D_s was required to be > 5 which ensures it is incompatible with the primary vertex. The angle between the D_s momentum and the direction from the primary vertex to the D_s vertex (from here on denoted by $\cos(\alpha)$) was required to be > 0.9. This ensures that the D_s candidate's momentum "points back" to the primary vertex.

The D_s candidate was vertexed with a muon to form the B_s candidate and the χ^2 of the vertex was required to be < 16. The muon must be in the same jet as the

other tracks. In addition the mass of the B_s candidate was required to be in the range $2.6 < M(\mu D_s) < 5.4$ GeV/c^2. The charge of the muon must be correlated with the pion from the D_s ie $q_\mu \times q_\pi < 0$. If the decay length of the B_s candidate was greater than the decay length of the D_s candidate then the distance between the vertices divided by the error was required to be < 2, excluding D_s candidates reconstructed "behind" the B_s. The p_T of the D_s had to be > 2.5 GeV/c and the B_s candidate was required to satisfy $p(\mu D_s) > 7$ GeV/c.

In reconstructing this decay mode, there are no decay length significance or angular cuts on the B_s candidate. This is because the sample will be used for B_s mixing and these cuts can harm the measurement. The lifetime of the sample collected with these cuts will be biased due to the loss of events with low proper times. These events are where the oscillation amplitude is the greatest (Equation 1.50). Therefore this approach was adopted for the hadronic reconstruction.

5.4.2 Results

Figure 5.3 shows the invariant mass of the D_s candidates with a right sign muon in the v13 data set. Two Gaussians and a polynomial of order two to describe the background were fitted to the data. The two peaks on the left and right correspond to the decays $B_d^0 \to \mu^+ D^- X$ with $D^- \to \phi\pi^-$ and $B_s^0 \to \mu^+ D_s^- X$ with $D_s^- \to \phi\pi^-$ respectively. There are approximately 1600 $B_s^0 \to D_s^- \mu X$ candidates. The width of the D_s is 10% larger in data than in MC and is typical of the mass resolutions at DØ.

5.5 $B_s \to D_s^- \pi^+$

In this section, the methods for reconstructing the $B_s \to D_s \pi$ decay are described. The philosophy is to base the reconstruction around the D_s as in the semileptonic case but to replace the "added" muon with a pion. The main problem in doing this

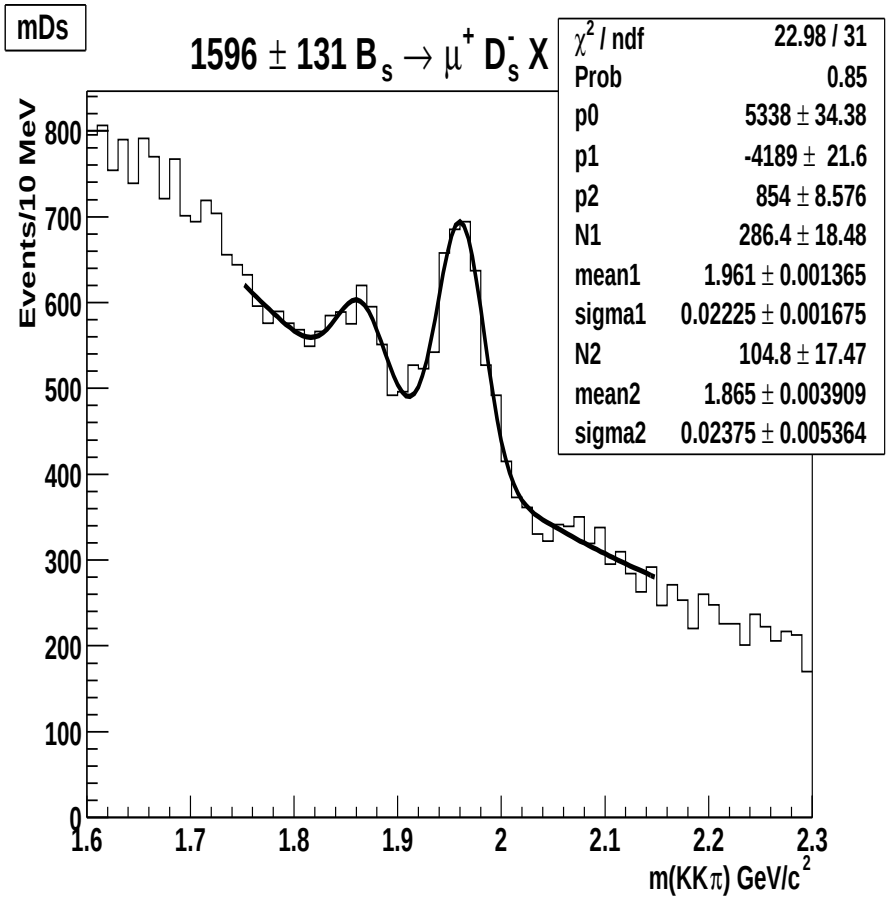

Figure 5.3: Invariant mass of the D_s candidates with right sign muon in the v13 data set. The main peak is due to $B_s^0 \to \mu^+ D_s^- X$ with $D_s^- \to \phi\pi^-$. The smaller peak is due to the decay $B_d^0 \to \mu^+ D^- X$ with $D^- \to \phi\pi^-$. There are in total ~ 1600 $B_s \to D_s \mu X$ candidates.

is that in any given event there are 2 orders of magnitude more tracks than muons. This creates extremely high combinatoric backgrounds.

The cuts were developed over a period of time with input from the $B_d \to D^{*-}\pi^+$ analysis. They were first tested on MC and the efficiencies checked. The reconstruction was then applied to the data. As already mentioned, the data contain more real and fake tracks than the MC and the procedure is to tune the cuts on data. To reduce combinatoric background, a good D_s candidate was enforced by tightening the semileptonic cuts. The remaining cuts on the B_s candidates were then tuned to maximise the number of signal events.

5.5.1 Monte Carlo

A sample of 102500 $B_s \to D_s^{(*)-}\pi^+$ events was generated using Pythia [61] and EvtGen [62] which are the official packages used by the B physics group for production and decay respectively. A B_s^0 meson and a $\mu^\pm$ with $p_T > 3.0$ GeV and $|\eta| < 2.2$ were required at the generator level. The sample was then passed through detector simulation, digitisation, `d0reco` and `BANA`. Table 5.1 shows the branching fractions used to generate the sample. The probability of a $B_s \to D_s$ decay in the event is 1. Note that the branching fractions of the $D_s \to \phi\pi$ and $\phi \to KK$ decays are 100% to increase statistics.

$B_s^0 \to D_s^{*-}\pi^+$	50.94%
$B_s^0 \to D_s^-\pi^+$	49.06%
$D_s^{*-} \to D_s^-\gamma$	94.2%
$D_s^{*-} \to D_s^-\pi^0$	5.8%
$D_s^- \to \phi\pi^-$	100%
$\phi \to KK$	100%

Table 5.1: Branching fractions used in the $B_s \to D_s^{(*)-}\pi^+$ Monte Carlo sample.

The MC was not passed through the trigger simulator explicitly.[2] However, the projections are still valid since no efficiencies are calculated from the MC.

5.5.2 Reconstruction cuts

The reconstruction cuts for the D_s were based on the semileptonic reconstruction, except that the p_T cut on all three tracks was increased to 1.0 GeV/c and the impact parameter significance cuts on one of the kaon tracks and the pion track was increased to > 3. These cuts were tighter than in the semileptonic reconstruction to reduce the large background under the D_s peak which, when vertexed with another track, could introduce large combinatorics. There were also the loose requirements that each track was required to have an axial impact parameter < 0.25 cm and a

[2] The Level-1 and Level-2 simulators were not functional in the p14 release. p17 will be the first release where they are officially certified.

stereo impact parameter < 0.4 cm in order to reduce combinatorics. This cut was first used in the B_s semileptonic reconstruction with $D_s^- \to K^{*0} K^-$ [63].

The mass of the D_s was required to be in the range $1.895 < M(KK\pi) < 2.027$ GeV/c^2 which was $\pm 3\sigma$ taken from the semileptonic D_s mass peak. The D_s candidate was vertexed with a track that was required to have $p_T > 2.0$ GeV/c and impact parameter significance > 2. These cuts on the final pion were the same as in the $B_d^0 \to D^{*-} \pi^+$ analysis.

A cone cut around the D_s direction was introduced. Figure 5.4 shows the $\Delta R = \sqrt{(\Delta\phi)^2 + (\Delta\eta)^2}$ between the D_s direction and the π from the B_s decay. The shaded

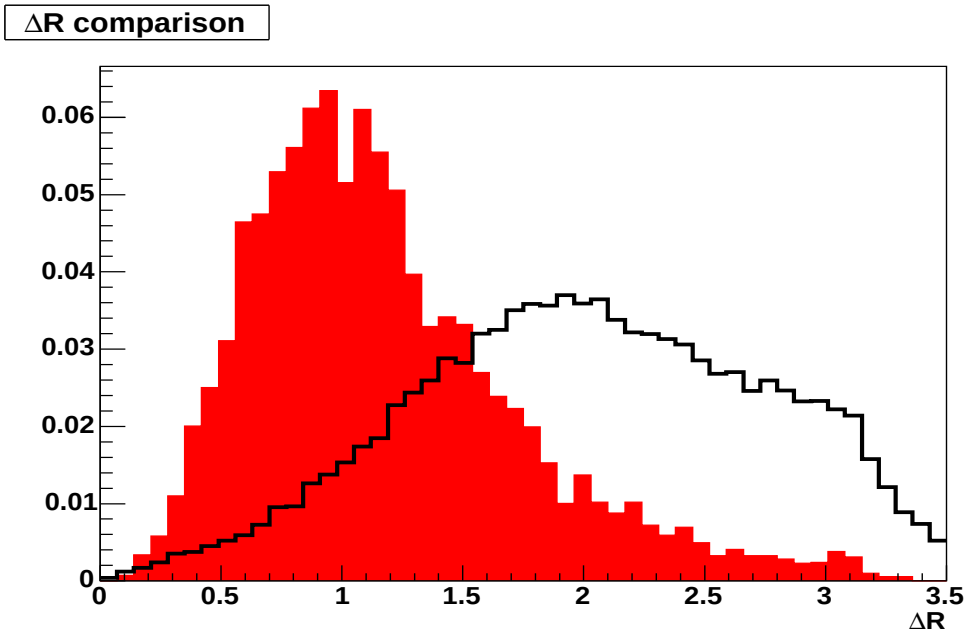

Figure 5.4: ΔR between the D_s direction and the π from the B_s. The shaded histogram is the ΔR in MC when the track is known to originate from a real B_s. The unshaded histogram is the value in the data. The histograms are scaled to have the same area.

histogram is the ΔR in MC when the track is known to originate from a real B_s. The unshaded histogram is the value in the data. The histograms are scaled to have the same area. A cut value of < 1.5 was chosen.

This track also had to have the opposite charge of the D_s and was hypothesised to be a pion. The vertex was required to have a $\chi^2 < 16$ and the B_s candidate

had to have a momentum > 7 GeV/c. If the decay length of the B_s candidate was greater than the decay length of the D_s candidate then the distance between the vertices divided by the error was required to be < 2.

5.5.3 Results

Monte Carlo

Figure 5.5 shows the invariant mass of the ϕ and D_s for the B_s decays in the MC. Figure 5.6 shows the invariant mass of the B_s decays for the $B_s^0 \to D_s^- \pi^+$ and $B_s^0 \to D_s^{*-} \pi^+$ decays respectively. Both peaks were fitted with single Gaussians and Table 5.2 summarises the fit parameters.

	mass (GeV/c^2)	σ (GeV/c^2)	constant
$B_s \to D_s$	5.362	0.068	137
$B_s \to D_s^*$	5.159	0.100	103

Table 5.2: Parameters from the $B_s \to D_s$ and $B_s \to D_s^*$ invariant mass Gaussian fits.

Table 5.3 shows the vertex resolutions for the primary (PV) and D_s and B_s secondary vertices.

	σ_x (μm)	σ_y (μm)	σ_z (μm)
PV	18	17	35
D_s	57	49	80
B_s	27	28	54

Table 5.3: Primary and secondary vertex resolutions for the $B_s \to D_s^{(*)-} \pi^+$ sample. Errors are at the 10% level.

The primary vertex resolutions are fitted with single Gaussian distributions. The secondary vertices are fitted with double Gaussian distributions and the weighted average σ quoted. The secondary vertices are sensitive to mis-reconstructed tracks or tracks with large errors and the residual distributions contain tails. This effect is larger for the D_s vertex reconstruction as it contains fewer tracks. The pull

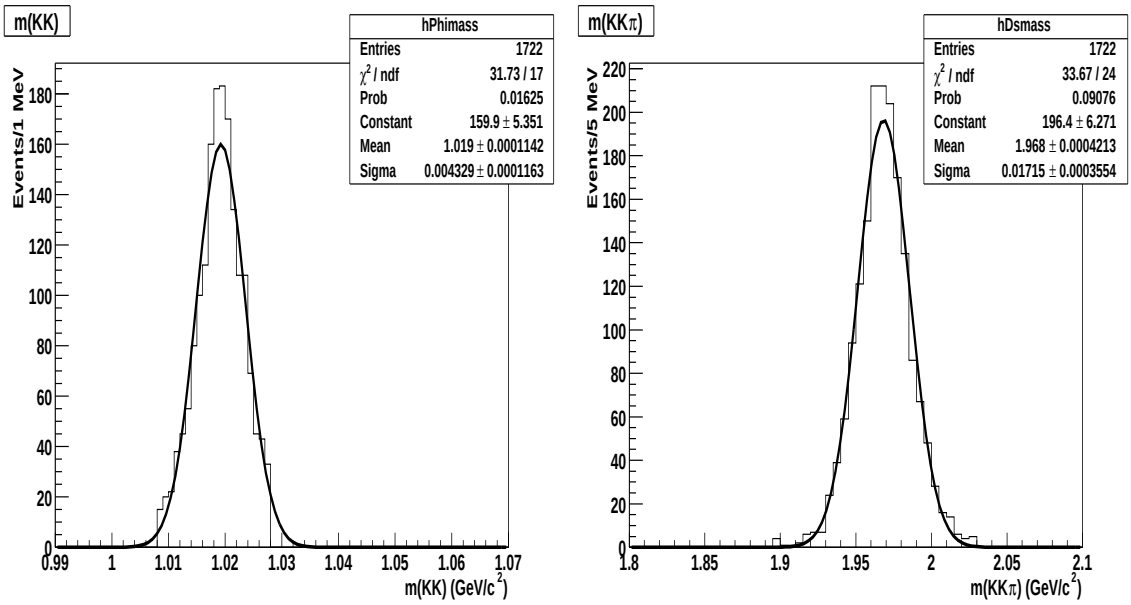

Figure 5.5: Invariant mass of the ϕ and D_s candidates in MC.

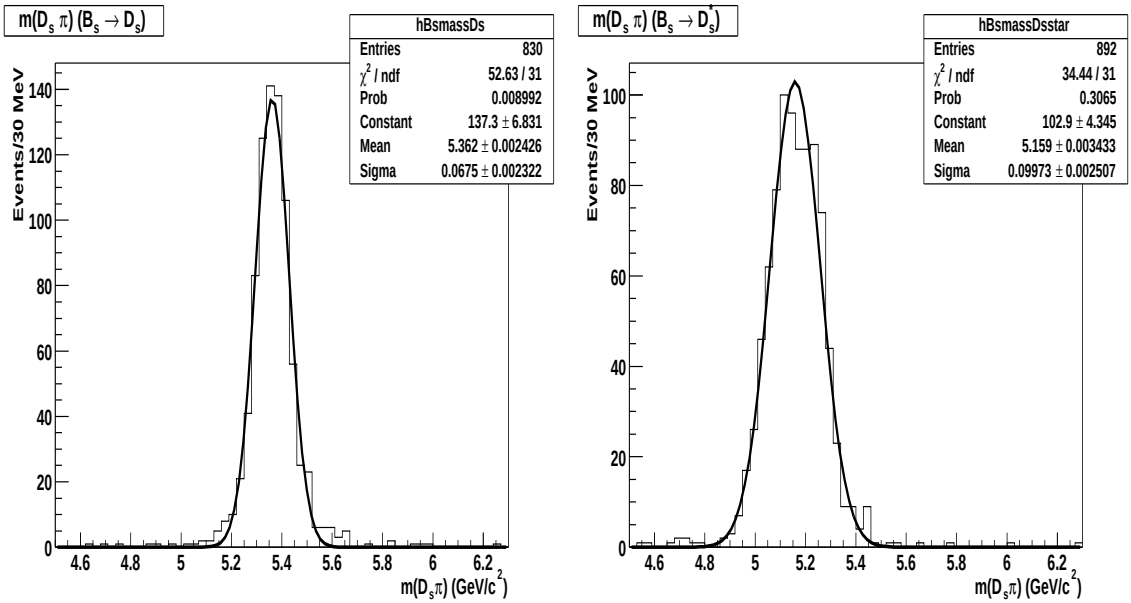

Figure 5.6: Invariant mass of B_s candidates in MC for $B_s \to D_s \pi$ and $B_s \to D_s^* \pi$.

distributions all have a width consistent with unity which implies the errors are correctly described.

The B_s proper time is defined by

$$t = \frac{L_{xy} \times M}{c \times p_T} \tag{5.1}$$

where L_{xy} is the transverse decay length, M is the B_s mass and p_T is the transverse momentum. In the $B_s^0 \to D_s^{*-} \pi^+$ decays, the photon or π^0 is not reconstructed and the p_T of the B_s is underestimated. This causes an overestimation of the proper time. It is possible that in the future these decays will be used for B_s mixing. Any such analysis will require a detailed determination of the correction factor for the p_T estimate. This is completely analogous to the correction factor in the semileptonic B_s mixing analysis where a correction factor is needed due to the missing neutrino. The first hadronic B_s mixing analyses will not use these events and increasing statistics by considering other hadronic decay modes, such as $D_s^- \to K^{*0} K^-$, will be preferred to using the $B_s^0 \to D_s^{*-} \pi^+$ decays. The introduction of the correction factor causes a loss in proper time resolution. Therefore, only the $B_s \to D_s^- \pi^+$ decays will be considered here.

The transverse decay length resolution, L_{xy}, and the p_T resolution are shown in Figure 5.7. The distributions are fitted with double Gaussians. The L_{xy} resolution has widths of 30 and 90 μm and the p_T resolution has widths of 115 and 405 MeV/c. Despite the double Gaussian structure of the resolution distributions, the pull distributions are Gaussian with a mean and width close to zero and unity respectively.

The proper time resolution is shown in Figure 5.8. The value from the Gaussian fit is 83 fs which is almost a factor of 2 better than in the semileptonic mode (150 fs [64]). The fact that the mean is consistent with zero shows that there is no bias in the estimation of the proper time.

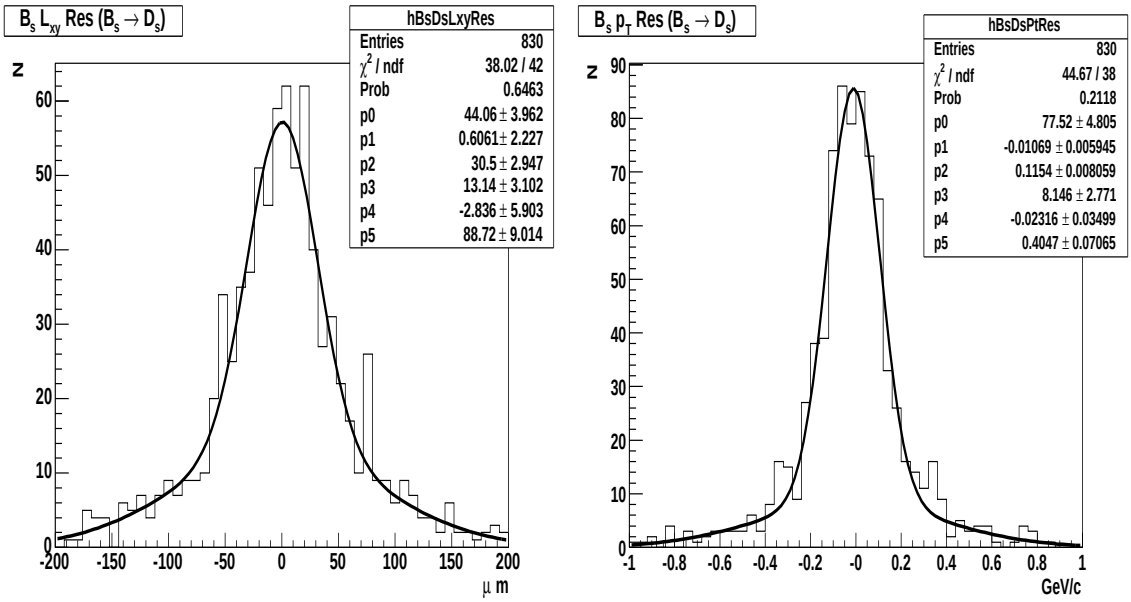

Figure 5.7: L_{xy} and p_T resolutions for the $B_s^0 \to D_s^- \pi^+$ candidates.

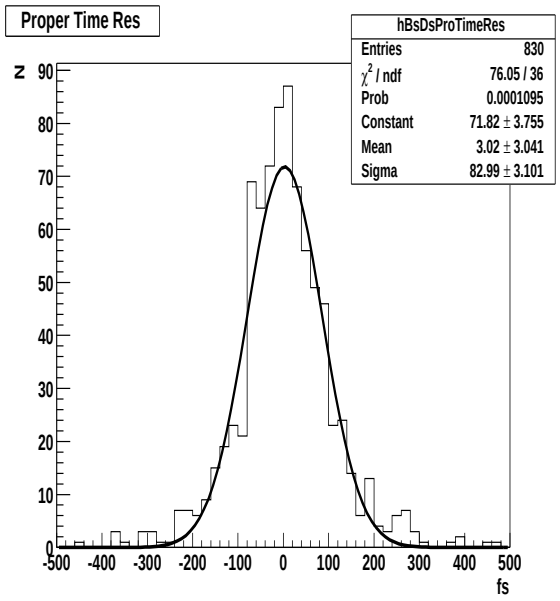

Figure 5.8: Proper time resolution for the $B_s^0 \to D_s^- \pi^+$ candidates.

Data

The B_s mass peak for the v13 data sample is shown in Figure 5.9. The peak on the left corresponds to $B_s^0 \to D_s^{*-} \pi^+$ where the D_s^{*-} has decayed to $D_s^- X$ where the X is a photon or π^0 and is unreconstructed. The peak on the right corresponds to

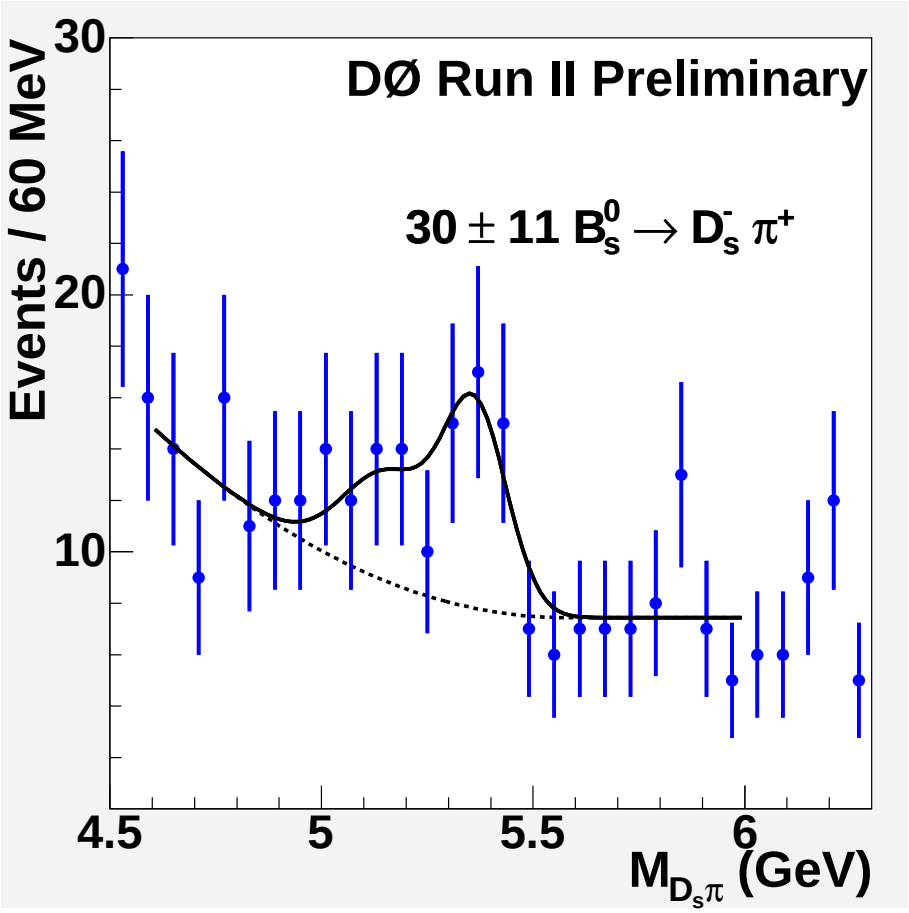

Figure 5.9: Mass of B_s candidates in the v13 data set. The peak on the left corresponds to $B_s^0 \to D_s^{*-}\pi^+$ where the D_s^{*-} has decayed to $D_s^- X$ where the X is a photon or π^0 and is unreconstructed. The peak on the right corresponds to $B_s^0 \to D_s^-\pi^+$. The signal fit is composed of two Gaussians with their relative widths fixed at 1.471 GeV/c^2 and their mean difference fixed at 0.203 GeV/c^2. Both values are obtained from MC. The background fit consists of a first order polynomial to model the non B background plus a second order polynomial which is required to be zero at 5.6 and above to model the B background.

$B_s^0 \to D_s^-\pi^+$. The signal fit is composed of two Gaussians with their relative widths fixed at 1.471 GeV/c^2 and their mean difference fixed at 0.203 GeV/c^2. Both values are obtained from MC. The mass resolution in data is known to be larger than in MC. For example, the D_s mass resolution (Figure 5.3) is 10% larger in data than in MC. In addition, the percentage increase is expected to be proportional to mass. This is confirmed in the $\Upsilon(1S)$ cross section analysis where the increase in mass resolution is 17% [65]. Therefore the percentage increase in width of the B_s mass peak is constrained to lie in between these two extreme values.

In an attempt to model the B background, the reconstruction code was applied to the entire DØ semileptonic B_s MC sample (300k events). However, due to the lack of statistics after applying the hadronic selection cuts, this proved unsuccessful. The background fit consists of a first order polynomial to model the non B background plus a second order polynomial which is required to be zero at 5.6 and above to model the B background. The number of signal events is 30 ± 11 and the number of background events is $\sim$76 assuming a window of $\pm 3\sigma$ from the B_s mean (5.14 to 5.59 GeV/c^2).

5.6 Full dataset

The reconstruction described in the previous section was applied to the full data set. This consists of $\sim$450 pb^{-1} collected between April 2002 and August 2004. Exactly the same cuts and fit were applied to the data. There is evidence of a B_s peak but there is around a factor of nine more background than signal. The value of $S/\sqrt{S+B}$ for the v13 data set is 2.7. The equivalent number for the same luminosity in the full dataset is 1.1. This emphasises the enhanced performance of the trigger using the impact parameter significance and invariant mass triggers introduced in v13.

5.7 Mass constraints

The momentum resolution of the B_s can be improved by constraining the tracks from the D_s to form a common vertex and to have an invariant mass equal to that of the D_s. This will improve the proper time resolution (Equation 5.1) and will increase the sensitivity to B_s oscillations. The `vfitter` package [66] provides many methods to apply kinematic constraints to vertices. Figure 5.10 shows the proper time resolution when the tracks from the D_s are vertexed and mass constrained to 1.968 GeV/c^2 [5]. The proper time resolution for the Gaussian fit is 78 fs which is a

5 fs improvement on the unconstrained vertex. An attempt to apply this method to data was unsuccessful since the errors in the data are not sufficiently well understood [67]. Understanding these errors is a primary concern for the DØ experiment and applies to all such analyses, but is outside the scope of this work.

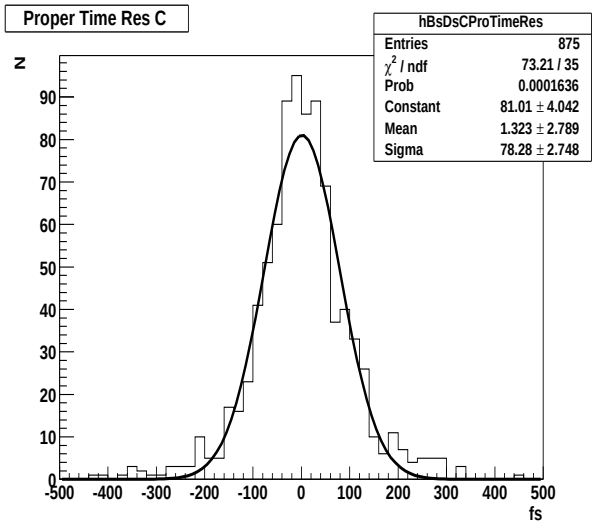

Figure 5.10: Proper time resolution for the $B_s^0 \to D_s^- \pi^+$ when the tracks from the D_s are vertexed and mass constrained to 1.968 GeV/c^2.

5.8 B_s mixing sensitivity

ΔM_s is related to the time dependent asymmetry, $A_0(t)$, defined by

$$A_0(t) = \frac{N^{non-osc}(t) - N^{osc}(t)}{N^{non-osc}(t) + N^{osc}(t)} \tag{5.2}$$

where t is the proper time and N^{osc} and $N^{non-osc}$ refer to the number of events tagged as oscillated and non-oscillated respectively (Section 1.4). Therefore the B_s flavour at production must be determined via a tagging mechanism. In practise a maximum likelihood fit to $A_0(t)$ is used to extract ΔM_s. For an observation of oscillations or a limit placed on the value of ΔM_s, the average significance of the likelihood fit is approximated by

$$Sig(\Delta M_s) = \frac{S}{\sqrt{S+B}} \sqrt{\frac{\epsilon D^2}{2}} e^{-(\Delta M_s \sigma_t)^2/2}. \tag{5.3}$$

where S and B are the number of signal and background events respectively and σ_t is the proper time resolution. ϵ and D are the efficiency and dilution of the applied flavour tag defined in terms of the number of correctly tagged, N_{tag}, and incorrectly tagged, N_{mistag}, events, ie

$$\epsilon = \frac{N_{tag} + N_{mistag}}{\text{Total}} \quad D = \frac{N_{tag} - N_{mistag}}{N_{tag} + N_{mistag}}. \tag{5.4}$$

Note that $D = 2P_{tag} - 1$ where P_{tag} is the probability for a correct tag.

In this case, each reconstructed B_s has an opposite side muon that can be used to tag the production flavour. A $\mu^-(\mu^+)$ implies the flavour at production was $B_s^0(\overline{B}_s^0)$. Therefore the tagging efficiency, ϵ, is effectively 100%. From studies performed for the semileptonic B_s mixing analysis on B_d and B_u data, the average dilution is found to be 0.727 [60]. Therefore $\epsilon D^2 = 0.53$.

The sensitivity is predicted for 4 fb^{-1} of data which is a conservative estimate for the amount of data collected by 2009. Using the yield in the v13 data, which is equivalent to 70 pb^{-1}, the number of signal and background events in 4 fb^{-1} is estimated to be 1720 and 4400 respectively.

The proper time resolution in data is known to be worse than in the MC. Estimates from the B_s mixing analysis [60], the B_s lifetime using semileptonic decays [68] and B_s and B_d lifetimes in the modes $B_s^0 \to J/\psi\phi$ and $B_d^0 \to J/\psi K^*$ [69] have shown the degradation in data to be anywhere from a factor of 1.2 to 1.6. To account for this in the sensitivity projections the best (MC value) and worse (1.6 $\times$ MC value) estimates of the proper time resolution form a band of possible values. The fractional gain in resolution due to the mass constraint in MC (0.94) is assumed to apply in data.

Figure 5.11 shows the sensitivity projection using these estimates. The average significance for a given ΔM_s is calculated using Equation 5.3. Figure 5.12 shows the sensitivity projection assuming the D_s vertex is mass constrained. The shaded region is excluded at the 95% confidence limit, $\Delta M_s \leq 14.4$ ps^{-1}. The projected

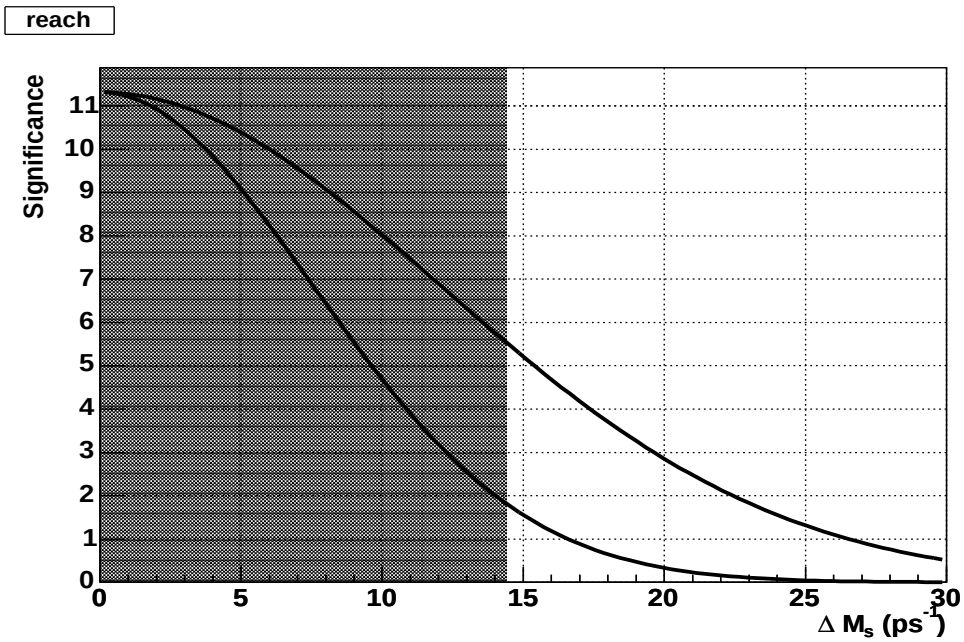

Figure 5.11: ΔM_s reach assuming 4 fb^{-1}, $\epsilon D^2 = 0.53$, and σ_t in the range 83-133 fs. The average significance for a given ΔM_s is calculated using Equation 5.3. The shaded region is excluded at the 95% confidence limit, ie $\Delta M_s \leq 14.4$ ps^{-1}. The projected reach for 3σ evidence of B_s oscillations is $\Delta M_s = 12.3$ - 19.6 ps^{-1}.

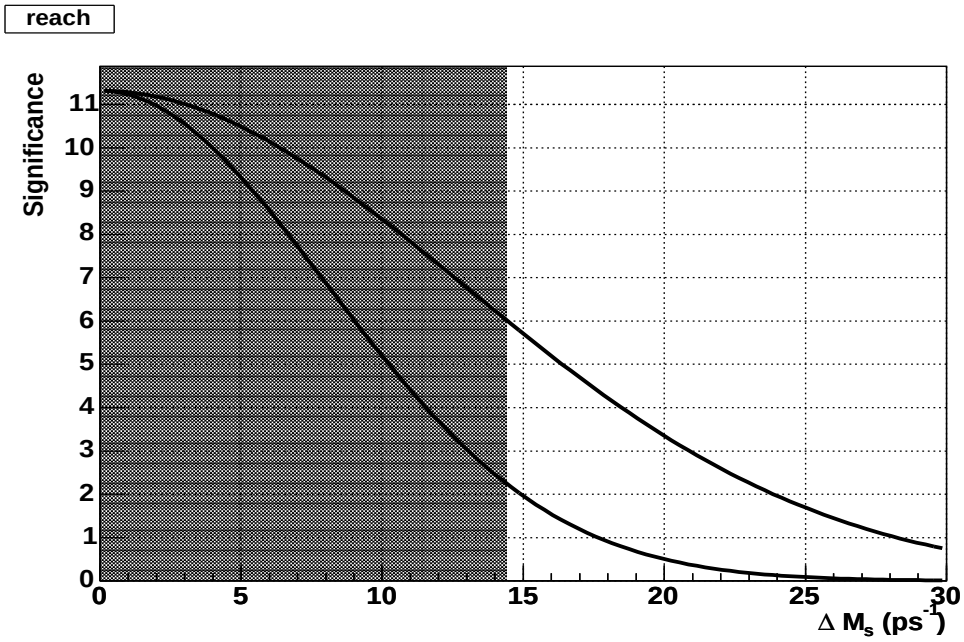

Figure 5.12: ΔM_s reach assuming 4 fb^{-1}, $\epsilon D^2 = 0.53$, and σ_t in the range 78-125 fs. The shaded region is excluded at the 95% confidence limit, ie $\Delta M_s \leq 14.4$ ps^{-1}. The projected reach for 3σ evidence of B_s oscillations is $\Delta M_s = 13.1$ - 21.0 ps^{-1}.

reach for 3σ evidence of B_s oscillations is ΔM_s = 12.3 - 19.6 ps^{-1} and 13.1 - 21.0 ps^{-1} for the unconstrained and constrained vertexing methods respectively.

There are two upgrades for the DØ detector that directly affect the B_s mixing sensitivity. The first one is the addition of the silicon Layer-0 [28]. This is an extra layer of silicon detectors situated between the inner radius of the SMT and the beam pipe. This will be installed in the summer of 2005. At between 2 and 4 fb^{-1} the first layer of the SMT will start to fail. An estimate of the fractional gain in proper time resolution with Layer-0 and no SMT Layer-1 is 0.72. The other upgrade proposed is increased Level-3 bandwidth for B physics. This would be possible due to new reconstruction farms based off the Fermilab site. The increased bandwidth would allow lower muon p_T thresholds. A conservative estimate of the effect of the increased bandwidth is a factor of three gain in statistics [64].

Figures 5.13 and 5.14 show the sensitivity projections including the Layer-0 and Level-3 bandwidth upgrades. The projected reach for 3σ evidence of B_s oscillations is now ΔM_s = 20.3 - 32.4 ps^{-1} and 21.6 - 34.5 ps^{-1} for the unconstrained and constrained vertexing methods respectively.

The range of ΔM_s predicted by the SM is 15.6 - 22.2 ps^{-1} at the 95% CL from global fits to the unitarity triangle. This includes the current limits from experiment. If these are not included the range moves to 14.2 - 28.1 ps^{-1} [20]. Even without the silicon Layer-0 and trigger bandwidth upgrades, DØ would still be able to make a 3σ discovery or set a new world limit on B_s mixing. However, when the upgrades are implemented the full SM range can be covered.

Therefore, these projections show that using the hadronic decay $B_s \to D_s^- \pi^+$, DØ could make a discovery of B_s oscillations or exclude the SM predictions indicating new physics. Either of these scenarios would be an extremely important result.

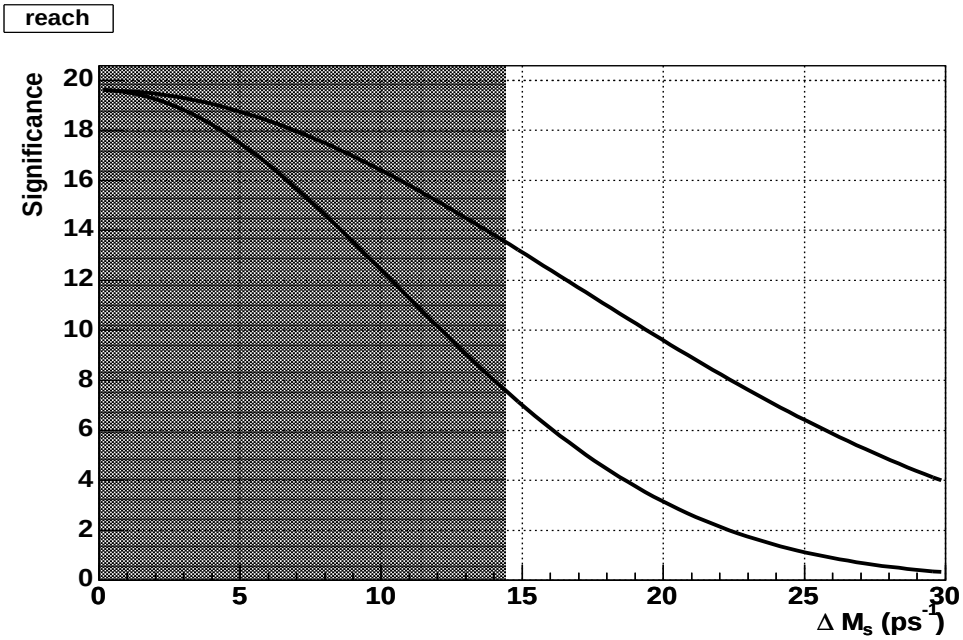

Figure 5.13: ΔM_s reach including silicon Layer-0 and the trigger bandwidth upgrade assuming 4 fb^{-1}, $\epsilon D^2 = 0.53$, and σ_t in the range 60-96 fs. The shaded region is excluded at the 95% confidence limit, ie $\Delta M_s \leq 14.4$ ps^{-1}. The projected reach for 3σ evidence of B_s oscillations is $\Delta M_s = 20.3$ - 32.4 ps^{-1}.

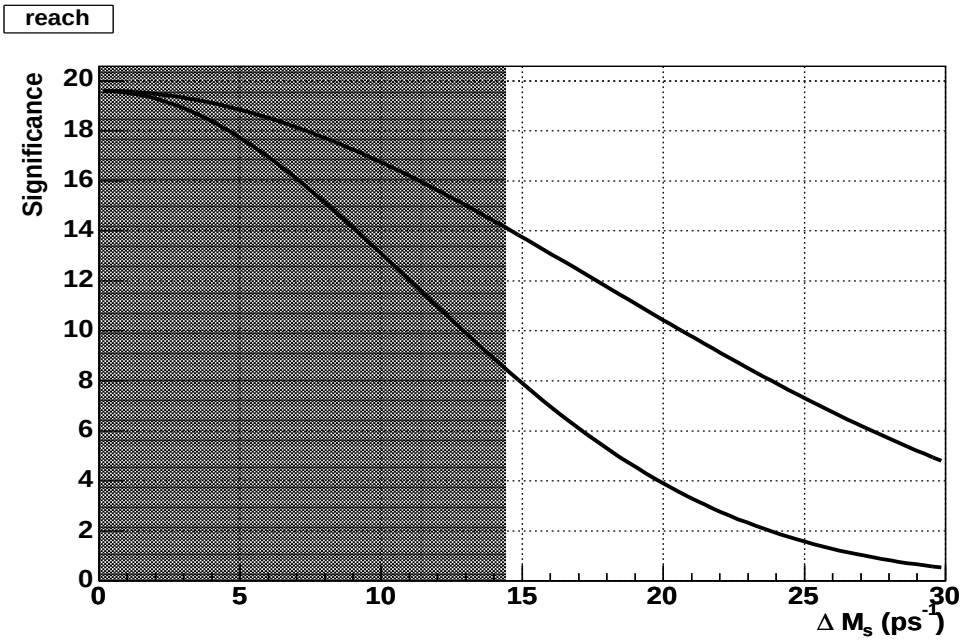

Figure 5.14: ΔM_s reach including silicon Layer-0 and the trigger bandwidth upgrade assuming 4 fb^{-1}, $\epsilon D^2 = 0.53$, and σ_t in the range 56-90 fs. The shaded region is excluded at the 95% confidence limit, ie $\Delta M_s \leq 14.4$ ps^{-1}. The projected reach for 3σ evidence of B_s oscillations is $\Delta M_s = 21.6$ - 34.5 ps^{-1}.

Chapter 6

Conclusions

6.1 Summary

One of the main goals at the Tevatron is the observation of B_s oscillations. Until the LHC turns on in 2007 the Tevatron is the only facility in the world that can perform this measurement. The value of ΔM_s will severely constrain the apex of the unitarity triangle and so is a very important test of the Standard Model. From fits to the unitarity triangle, the SM predicts upper limits on ΔM_s of 22.2 ps^{-1} and 28.1 ps^{-1} if limits from experiment are included or excluded respectively [20]. Another motivation is that historically the discovery of mixing in other systems has led to new insights. Mixing in the kaon system led to the discovery of CP violation and mixing in the B_d system indicated a large top mass.

Both the Tevatron and DØ are performing well. The Tevatron is now exceeding the design instantaneous luminosity regularly and DØ is recording data with an efficiency of over 90%. The B physics programme has been very successful and the B physics group is the most prolific at DØ with 4 papers already published or submitted and with many more expected in the near future. These include the world's best limit on $B_s \to \mu\mu$, a measurement of $\Delta\Gamma_s$ and a limit on B_s oscillations using $B_s^0 \to D_s^- \mu^+ X$ decays.

The work described in this thesis has contributed very significantly to the physics output of the DØ experiment. The Level-3 vertexing algorithms developed are now

an integral part of the experiment's trigger strategy. The z vertexing tool has an efficiency and purity above 95% for all types of MC events and is used by almost every physics group at DØ, encompassing B physics, Higgs, Top, Electroweak and New Phenomena. The x-y vertex resolution in data is $\sim$15 μm which is competitive with the offline vertexing algorithms despite running three orders of magnitude faster and having half the tracks available for vertexing. It forms the basis of all Level-3 lifetime and B-tagging triggers which are relied on by the B physics and Higgs groups. The New Phenomena and Top groups will also adopt the triggers in the future. The primary vertexing has recently become a basis for a new Level-3 secondary vertexing tool.

The development of the triggers designed for low p_T B physics has also made a significant contribution to the experiment. These triggers, which include track and muon impact parameter significance and invariant mass tools, have allowed the single muon triggers to run unprescaled at all luminosities. Previous to this work, the single muon triggers were effectively turned off at all but the lowest luminosities, severely damaging the prospects for B_s mixing, especially in the statistically limited hadronic mode $B_s^- \to D_s^- \pi^+$. These triggers also underlie many other analyses, and as the luminosity increases, they will become increasingly important to many other decay channels. In addition, the tools were developed with extendability in mind and the addition of impact parameter significance tools for electrons, taus or indeed any object containing tracks, is straightforward.

The first observation of hadronic B decays, and in particular the decay $B_s^0 \to D_s^- \pi^+$, is a very important step for the B physics group at DØ. The yield is 30 events in 70 pb^{-1}, each with their production flavour tagged by the opposite side muon. These numbers show that the triggers developed are working very well, and place DØ in an excellent position to discover B_s oscillations in the hadronic mode.

This information on the yield, which cannot be estimated from MC, is an essential input for the sensitivity projections. The projections made here show that, with the

silicon Layer-0 and the trigger bandwidth upgrade, DØ can cover the full predicted SM range for ΔM_s using the hadronic mode $B_s \to D_s^- \pi^+$.

6.2 Further work

Due to increases in luminosity there will always be further development and refinement of the Level-3 trigger. Extensions to the work described here include modifying the z finding algorithm to find multiple vertices. This would be used to reject events with a large number of minimum bias events and could be critical as the luminosity increases. If three dimensional b-tagging is required at Level-3, then either an improved z finding algorithm or a new x-y-z finding algorithm would be required; either of which is easily achieved by building on the existing code.

As already mentioned, the impact parameter significance tools could be extended to electrons matched to tracks. An obvious extension of the invariant mass tool would be to allow a three track invariant mass. Armed with this tool, the D_s could be directly triggered on. A more ambitious extension would be to make a B_s invariant mass tool. An object oriented framework could be developed that uses different invariant mass objects. For example, different D_s invariant mass objects could exist which reconstruct D_s candidates in different channels. The B_s tool could use the D_s tool as an input, independent of the mode the D_s was reconstructed in. The Level-3 trigger at DØ makes the development of sophisticated trigger tools like this possible.

Now that the $B_s^0 \to D_s^- \pi^+$ decay has been reconstructed at DØ the B physics group will continue the work started here. The hadronic analysis will be developed in parallel to the semileptonic analysis. With an increase in statistics and a need for improved proper time resolution to probe higher values of ΔM_s, the hadronic mode will become increasingly important, until eventually it dominates. Improvements in the signal to noise ratio and understanding the proper time resolution will be strong areas of activity. Other B_s decay modes such as $B_s \to D_s \pi\pi\pi$ and D_s decay modes

such as $D_s \to K^*K$ will be included to increase statistics. Important new work will also lie in the use of artificial neural networks to find optimal cut values for each decay mode.

The DØ experiment is already progressing towards either a ΔM_s measurement or an exclusion of its SM predicted values. Just as Run I of the Tevatron is remembered for the discovery of the top quark, Run II will be remembered for B_s mixing.

Appendix A

Level-3 track parameters

S_1/R R is the radius of the circle in the x-y plane.

S_1 is the track rotation: -1 or +1 for tracks clockwise and anticlockwise respectively.

$S_2 \times d_0$ d_0 is the distance of closest approach of the track to the origin in the x-y plane.

S_2 is the sign of the angular momentum of the track about the origin at the d_0 point.

ϕ_0 is the azimuthal angle of the track direction at the d_0 point.

$\tan\lambda = dZ/dS_{xy}$ specifies the pitch of the helix. S_{xy} refers to the distance traversed around the arc in the x-y plane measured from the d_0 point.

Z_0 is the Z position of the track helix at the d_0 point.

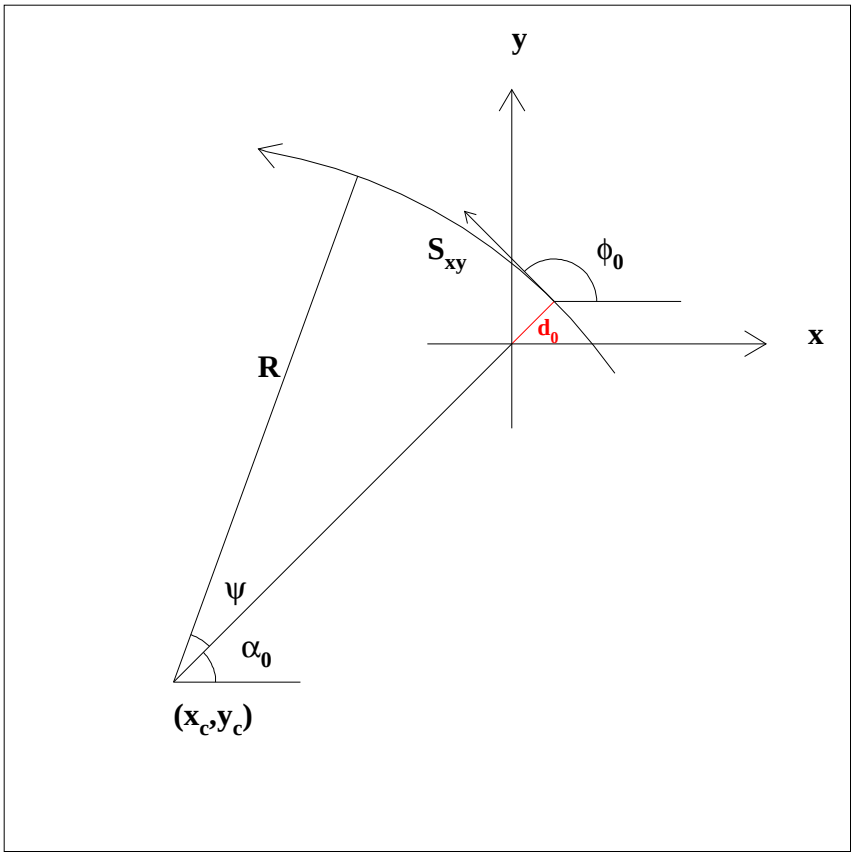

Figure A.1: Relation between Level-3 track parameters

References

[1] F. Halzen, A. Martin, "Quarks & Leptons", John Wiley & Sons, 1984, ISBN 0-471-81187-4

[2] "B Physics at the Tevatron Run II and Beyond" FERMILAB-Pub-01/197, hep-ph/0201071

[3] SNO collaboration, "Direct Evidence for Neutrino Flavor Transformation from Neutral-Current Interactions in the Sudbury Neutrino Observatory", Phys. Rev. Lett. 89, 011301 (2002)

[4] J. Christenson *et al.* "Evidence for the decay of the K_2^0 meson", Phys. Rev. Lett. 13, 138 (1964)

[5] S. Eidelman *et al.* "The Review of Particle Physics", Phys. Lett. B592, 1 (2004)

[6] S. Weinberg, "A model of leptons", Phys. Rev. Lett. 19, 1264 (1967)

[7] P. Higgs, "Broken Symmetries, massless particles and gauge fields", Phys. Lett. 12, 132 (1964)

[8] P. Higgs, "Broken Symmetries and the masses of the gauge bosons", Phys. Lett. 13, 508 (1964)

[9] P. Higgs, "Spontaneous Symmetry Breakdown without Massless Bosons", Phys. Rev. 145, 1156 (1966)

[10] M. Kobayashi, T Maskawa, "CP-violation in the Renormalizable Theory of Weak Interaction", Prog. Theor. Phys 49, 652 (1973)

[11] L. Wolfenstein, "Parameterization of the Kobayashi-Maskawa Matrix", Phys. Rev. Lett. 51, 1945 (1984)

[12] H. Wittig, "Status of lattice calculations of B-meson decays and mixing", hep-ph/0310329

[13] KTEV Collaboration, "Observation of Direct CP violation in $K_{S,L} \to \pi\pi$ Decays", Phys. Rev. Lett. 83 22 (1999)

[14] NA48 Collaboration, "A new measurement of direct CP violation in two pion decays of the neutral kaon" Phys. Lett. B 465 (1999) 335

[15] Belle collaboration, "Observation of Large CP Violation and Evidence for Direct CP Violation in $B^0 \to \pi^+\pi^-$ Decays", Phys. rev. Lett. 93 021601 (2004)

[16] Belle collaboration, "Evidence for Direct CP Violation in $B^0 \to K^+\pi^-$ Decays", Phys. Rev. Lett 93 131801 (2004)

[17] Babar collaboration, "Observation of Direct CP Violation in $B^0 \to K^+\pi^-$ Decays", Phys. Rev. Lett 93 191802 (2004)

[18] Belle collaboration, "Measurement of the CP Violation Parameter $sin2\phi_1$ in B_d^0 Meson Decays, Phys. Rev. Lett 86 2509-2514 (2001)

[19] Babar collaboration, "Measurement of CP-Violating Asymmetries in B^0 Decays to CP Eigenstates", Phys. Rev. Lett 86 2515-2522 (2001)

[20] M. Battaglia *et al.* "The CKM matrix and the unitarity triangle", hep-ph/0304132

[21] R. D. Field, "Sources of b quarks at the Fermilab Tevatron and their correlations", Phys. Rev. D 65 094006 (2002)

[22] CDF and DØ Collaborations, "b-production at the Tevatron", hep-ex/030933

[23] M. Mangano, "B production at Tevatron", Talk given at HCP 2004

[24] M. Mangano, "The saga of bottom production in $p\bar{p}$ collisions" hep-ph/0411020

[25] DØ Collaboration, "Observation of the Top Quark", Phys. Rev. Lett. 74 2632 (1995)

[26] "Run II Handbook", Fermilab beams division Run II web-page, http://www-bd,fnal.gov/runII/index.html

[27] DØ Collaboration, "The DØ Upgrade: The Detector and its Physics", Fermilab-Pub-96/357-E

[28] H. Evans, "The Run IIb Upgrade Prospects and Challenges", Talk given at DØ Collaboration Meeting 10 Dec 2004

[29] "Tevatron Collider and Operations Plans", Beams-doc-1183-v1

[30] "Run II Luminosity Upgrade at the Fermilab Tevatron, v2.0", http://www-bdnew.fnal.gov/doereview04/RunII_Upgrade_Plan_v2.0.pdf

[31] A. Meyer, "Shutdown and Status Report", Talk given at DØ Collaboration Meeting 8 Dec 2004

[32] DØ Collaboration, "The DØ Detector", Nucl Instr. and Methods A 338 185 (1994)

[33] D. Edmunds *et al.* "Technical Design Report for the Level 2 Global Processor", DØ Note 3402

[34] R. Illingworth, "Raw Data Format and Unpacking for the SMT", DØ Note 3829

[35] D. Bauer, R. Illingworth, "L3 Trigger. Clustering in the SMT", DØ Note 3822

[36] D. Whiteson, "Global Track Finding at Level 3", DØ Note 3808

[37] M. Narain, F. Stichelbaut, "Vertex Reconstruction using the Impact Parameters Technique", DØ Note 3560

[38] G. Borissov, "Lifetime Tag of events $Z^0 \to b\bar{b}$ with the DELPHI detector. AABTAG program." DELPHI Note

[39] D. Bloch *et al.* "Performance of the JLIP b-tagger in p14", DØ Note 4348

[40] M. Sanders "Beam Position Monitoring in Real Time", DØNote 4755

[41] http://www-clued0.fnal.gov/ avdhesh/Beam_main.html

[42] A Garcia-Bellido *et al.* "Primary Vertex certification in p14", DØ Note 4320

[43] http://www-d0.fnal.gov/computing/algorithms/status/p14.html

[44] C. Leonidopoulos, "The Muon Trigger at DØ", DØ Note 4099

[45] P. Balm, "Central Track Matching of Muon Tracks at Level 3", DØ Note 3934

[46] P. Balm *et al.* "The DØ Level-3 muon filter" DØ Note 3999

[47] R. Gelhaus, J. Ellison, "B_s Mixing using $B_s \to D_s^{(*)}\pi$ at DØ", DØ Note 4108

[48] CDF Collaboration, "Masses and branching fractions at CDF", Eur. Phys. J C 33, s01, s189-s191 (2004)

[49] G. Borissov, "Status of DØ Track Reconstruction", Talk given at All DØ Meeting, 14 Feb 2003

[50] G. Borissov, "Ordering a Chaos or... Technical Details of AA Tracking", Talk given at All DØ Meeting, 28 Feb 2003

[51] A. Khanov, "HTF: histogramming method for finding tracks. The algorithm description.", DØ Note 3778

[52] H. Greenlee, "The DØ Kalman Track Fit", DØ Note 4303

[53] H. Greenlee, "The DØ Interacting Propagator", DØ Note 4293

[54] http://d0server1.fnal.gov/users/nomerot/Run2A/B_ANA.html

[55] The Delphi Collaboration, "b-tagging in DELPHI at LEP", Eur. Phys. J. C32 185-208 (2004)

[56] S. Catani *et al.* "New clustering algorithm for multijet cross section in e^+e^- annihilation", Phys. Lett. B269 432 (1991)

[57] C. Clement *et al.* "MuonID Certification for p14", DØ Note 4350

[58] http://d0online2.fnal.gov:8511/www/RunII.html

[59] DØ Collaboration, "Reconstruction of B hadron signals at DØ", DØ Note 4481

[60] The B_s Mixing Group, "Limits on B_s mixing at DØ using $B_s \to \mu\nu X$ with opposite side tagging", DØ Note 4701

[61] T. Sjöstrand *et al.* "Pythia 6.2 Physics and Manual", Comp. Phys. Comm. 135, 238 (2001)

[62] D. J. Lange, "The EvtGen particle decay simulation package", Nucl. Inst. Meth. A462, 152 (2002)

[63] DØ Collaboration, "Reconstruction of the $B_s \to D_s^- \mu^+ X (D_s^- \to K^{*0} K^-)$ decay at DØ.", DØ Note 4581

[64] B. Abbot *et al.* "Estimated Gains in B Physics with Increased L3 Trigger Bandwidth", DØ Note 4318

[65] D. Bauer *et al.* "Studies of $\Upsilon(1S)$ state production with the DØ Detector at Fermilab", DØ Note 4523

[66] S. Towers, "`vfitter`: A Vertexing Package with Kinematic and Topological Constraints", DØ Note 3994

[67] S. Towers, "Optimizing the Efficiency of Mass Constrained Vertex Fitting via a Track p_T Uncertainty Scale Factor", DØ Note 4407

[68] A. Sanchez-Hernandez, "Measurement of the B_s^0 lifetime using the semileptonic decay channel $B_s^0 \to D_s^- \mu^+ \nu X$", DØ Note 4690

[69] C. Luo, "A study of $B_s^0 \to J/\psi\phi$ and $B_d^0 \to J/\psi K^*$ Decays with the DØ Detector at Fermilab", DØ Note 4221